AVO IN AZIMUTHALLY ANISOTROPIC MEDIA FRACTURE DETECTION USING P-WAVE DATA AND A SEISMIC STUDY OF NATURALLY FRACTURED TIGHT GAS RESERVOIRS

A DISSERTATION

SUBMITTED TO THE DEPARTMENT OF GEOPHYSICS

AND THE COMMITTEE ON GRADUATE STUDIES

OF STANFORD UNIVERSITY

IN PARTIAL FULFILLMENT OF THE REQUIREMENTS

FOR THE DEGREE OF

DOCTOR OF PHILOSOPHY

Wei Chen

August 1995

Abstract

An enormous amount of natural gas exists in naturally fractured, low-permeability reservoirs. In such reservoirs natural fractures often control the storage and mobility of gas in tight formations. Present technology allows us to exploit the increased drainage provided by natural fractures. For reservoir engineers to make better decisions on drilling, it is very important to be able to locate the fracture zones and determine the position, orientation, spatial density, and connectivity of fractures. Detecting and characterizing natural fractures are critical practical problems for tight gas reservoir characterization.

During the last ten years, considerable emphasis has been placed on seismic velocity anisotropy as the key indicator of fractures. Multi-component VSP and surface reflection seismic studies have shown striking evidence of anisotropy, primarily from shear-wave splitting. It has become the industry standard to use shear-wave splitting, which measures velocity anisotropy of shear-waves, to study fractures.

While the industry focuses on the relatively expensive multi-component shear-wave methods, rich information of velocity, amplitude, and frequency in the better-established and more cost effective single component (P-wave) data has not been fully exploited. With the increasing popularity of 3-D seismology, it is now possible to detect velocity anisotropy from P-wave data through azimuthal variations of traveltime and amplitude-versus-offset (AVO) trends, and then map fractures from anisotropy just as we do using shear-wave methods.

The *objective* of this research is to develop a methodology to detect and characterize natural fractures using conventional one-component P-wave data. This thesis includes three key parts.

The first part is dedicated to the study of AVO trends in azimuthally anisotropic environments. AVO analysis is widely used as a hydrocarbon indicator in the oil industry. Conventional AVO techniques, however, ignore the possibility that the media may be azimuthally anisotropic. This practice may introduce serious errors since azimuthal anisotropy has been widely observed from well logging, vertical seismic profiling (VSP) and multi-component surface seismic surveys. In this part I present simple formulas to estimate AVO responses in orthorhombic media and show that azimuthal anisotropy can indeed significantly change AVO trends. The effect of azimuthal anisotropy is quadratic in the sine of angle of incidence, and linear in the difference of anisotropy between the layers. When the media are only transversely isotropic, but with a horizontal symmetry axis, the

AVO trends depend not only on the contrast in Thomsen's parameter δ, but also on those in ε and γ.

The second part studies possible P-wave seismic signatures of natural fractures. The focus is on azimuthal variations of traveltime and AVO responses, and attributes representing the frequency content of seismic traces. To simplify the discussion I use the model of a single set of parallel vertical fractures. The seismic observables are linked to the anisotropy parameters through the theoretical work done by Thomsen (1986), Sena (1991) and myself, and then to fracture parameters using Hudson's crack theory (Hudson, 1981). P-wave azimuthal anisotropy can be detected only when the offset is at least comparable to the target depth. The maximum amount of P-wave traveltime variations is approximately one half of the traveltime difference between the fast and the slow shear-waves, which can be tens of milliseconds. Azimthal traveltime analysis is useful for detecting both fluid-filled and gas-saturated fractures, whereas azimuthal AVO analysis is effective only for fluid-filled fractures. Therefore, the best fracture indicator in tight gas reservoirs is P-wave traveltime anisotropy.

The last part of the thesis is a report on a 9-component seismic study of a tight gas reservoir in the Powder River Basin, east-central Wyoming. It includes the geological description of the survey area, the information about data collection and processing, the interpretation of the shear-wave data, and the results of our search for P-wave signatures of natural fractures. It is part of our final report submitted to the U.S. Department of Energy.

We collected about 50 kilometers of 9-component surface reflection seismic data at the southern boundary of the Powder River Basin. Throughout the field site, the fracture *directions*, inferred from the shear-wave rotation analysis on all four lines, trend consistently SW-NE — all generally within about 20° of each other. These trends were taken to be equal to the polarization direction of the fast shear wave after rotation. The fracture *intensity* was taken to be proportional to relative time difference between the fast and slow shear waves at each location. This travel time difference (inferred fracture intensity) is highly variable throughout the site – the corresponding shear-wave anisotropy in the Frontier-Niobrara zones ranges from near zero to as much as 7 percent. The regions of largest anisotropy can be interpreted with two localized zones of relatively intense fracturing.

Perhaps most intriguing are the several indications of P-wave anisotropy that I observed. Azimuthal variations of AVO response and P-wave stacking velocity were observed at two locations where lines intersect. The azimuthal velocity variation is consistent with the directions of the fracture model.

Acknowledgments

I am deeply appreciative of being part of Stanford Rock Physics Group. I thank all the faculty, staff members, and students who have made my study at Stanford a wonderful and rewarding experience.

My sincerest gratitude goes to my advisor, Professor Gary Mavko, and co-advisor, Professor Amos Nur, for their advice, encouragement, patience, and continuous support. Many thanks to Gary Mavko who has been giving stimulating ideas and useful feedback on my research. I have benefited greatly from the discussions with him. Amos Nur's broad interest in all aspects of geophysics has always been an inspiring source.

I would also like to thank other members of my academic committee, James Ingle (Chairman), Mark Zoback, Greg Beroza, Jerry Harris, Francis Muir, and Jack Dvorkin, for their stimulating questions and insightful suggestions.

Special thanks go to Margaret Muir for her great deal of help over the course of my stay at Stanford.

As a foreign student, I deeply appreciate the friendly and enjoyable environment made possible by everyone in the department. Thanks to the many students who have been very helpful, including my officemate Dawn Burgess, Tapan Mukerji, Christina Chan, Qiang Chen, Hezhu Yin, J. P. Blangy, Xinzhou Liu, Ralf Schulz, James Packwood, Duron Galmudi, Li Teng, and Yuguang Liu.

My research was partly funded by the Department of Energy, Amoco, Arco, and the Gas Research Institute. I wish to thank for their financial support. I thank Rob Walters for allowing me to include some of his work on the geological background of the test site in this thesis. I am also grateful for the sponsorship of the SRB affiliates.

I also wish to express my special thanks to my parents, my grandmother, my sister and brother, who has always been an inspiration for me, for their strong moral support.

Finally, I would like to thank Hong Chen for her help both in my work and in my life. I will always be indebted to her invaluable contributions.

Contents

List of Tables

List of Figures

Chapter 1

Introduction

1.1 Fracture detection

Natural gas is an important source of energy. Depending on the prices of crude oil and the U.S. energy policy, natural gas may emerge as an alternative fossil fuel to oil. The current gas reserve is approximately 500 Tcf by some estimation, enough to last only 30 years at today's consumption rate (Blangy, 1992).

1.1.1 The problem — fracture detection and characterization

An enormous amount of natural gas exists in naturally fractured, low-permeability reservoirs. In such tight gas reservoirs the permeability of the matrix rock can be as low as one microdarcy, seriously inhibiting gas flow essential for commercial production. On the other hand, regional, systematic fracture sets can easily increase the permeability by one or two orders of magnitude, sometimes more (Lorenz et al., 1991). It is fair to say that fractures control the storage and mobility of gas in tight formations.

Present technology allows us to exploit the increased drainage provided by natural fractures. For example, horizontal wells have been drilled to intersect a maximum number of fractures to enhance gas flow (Mueller, 1992). For reservoir engineers to make better decisions on drilling, it is very important to be able to locate the fracture zones and determine the position, orientation, spatial density, and connectivity of fractures. Detecting and characterizing natural fractures are critical practical problems for tight gas reservoir characterization.

1.1.2 Motivation for *new* research

Theoretical and laboratory studies (Nur, 1971; Hudson, 1980, 1981; Yin, 1993) have shown that fractures have many effects on the seismic properties of rocks, such as lower velocity, increased velocity anisotropy, and higher attenuation. When seismic waves pass through a fractured rock, the fractures may influence or change the characteristics of the waves. For example, the traveltime may increase, the amplitude-versus-offset (AVO) responses may change, the recorded seismic traces may have less high frequency content, and the traveltime and AVO trends may display azimuthal variations. Searching for these signatures using reflection seismic methods allows us to detect and characterize fractures.

During the last ten years, considerable emphasis has been placed on seismic velocity anisotropy as the key indicator of fractures. Multi-component VSP and surface reflection seismic studies have shown striking evidence of anisotropy, primarily from shear-wave splitting (Alford, 1986; Willis et al., 1986; Mueller, 1992). It has become the industry standard to use shear-wave splitting, which measures velocity anisotropy of shear-waves, to study fractures.

While the industry focuses on the relatively expensive multi-component shear-wave methods, rich information of velocity, amplitude, and frequency in the better-established and more cost effective single component (P-wave) data has not been fully exploited. With the increasing popularity of 3-D seismology, it is now possible to detect velocity anisotropy from P-wave data through azimuthal variations of traveltime and amplitude-versus-offset (AVO) trends, and then map fractures from anisotropy just as we do using shear-wave methods.

There are many advantages for using P-wave methods instead of shear-wave methods to study fractures. P-wave data is cheaper to collect and easier to process. It suffers less from ground roll and other noise. Its higher data quality allows detailed study of traveltime and reflection amplitude. Furthermore, most of the existing land data and all marine data are P-wave.

1.1.3 Major research goals

The *objective* of this research is to develop a methodology to detect and characterize natural fractures using conventional one-component P-wave data. My approach is to identify theoretically possible seismic signatures of natural fractures, and to explore a processing and interpretation strategy for linking these signatures to the rock parameters through a real 2-D field survey.

The project includes three key elements:

- Theoretical studies of AVO signatures in azimuthally anisotropic media in general.
- Theoretical studies of possible P-wave signatures of fractures, such as azimuthal variations of traveltime and AVO trends.
- A 9-component reflection seismic survey in a tight gas reservoir to test the P-wave signatures of natural fractures and compare the results with those from the standard shear-wave analysis.

With my work, I wish to provide a sound framework, both in theory and in practice, for future large-scale 3-D reflection seismic surveys to further test the idea of detecting fractures using P-wave data.

1.2 Plan

This dissertation is organized as follows:

Chapter 2 is dedicated to the study of AVO trends in azimuthally anisotropic environments. AVO analysis is widely used as a hydrocarbon indicator in the oil industry. Conventional AVO techniques, however, ignore the possibility that the media may be azimuthally anisotropic. This practice may introduce serious errors since azimuthal anisotropy has been widely observed from well logging, vertical seismic profiling (VSP) and multi-component surface seismic surveys. In this chapter I will present simple formulas to estimate AVO responses in orthorhombic media and show that azimuthal anisotropy can indeed significantly change AVO trends. This study is theoretically based on Thomsen's formulation of weak elastic anisotropy (Thomsen, 1986). It is very important not only for fracture detection, but also for gas exploration as well.

Chapter 3 studies possible P-wave seismic signatures of natural fractures. The focus is on azimuthal variations of traveltime and AVO responses, and attributes representing the frequency content of seismic traces. To simplify the discussion I use the model of a single set of parallel vertical fractures. The seismic observables are linked to the anisotropy parameters through the theoretical work done by Thomsen (1986), Sena (1991) and myself, and then to fracture parameters using Hudson's crack theory (Hudson, 1981).

The last chapter is a report on our 9-component seismic study of a tight gas reservoir in the Powder River Basin, east-central Wyoming. It includes the geological description of the survey area, the information about data collection and processing, the interpretation of the shear-wave data, and the results of our search for P-wave signatures of natural fractures. It is part of our final report submitted to the U.S. Department of Energy.

References

Blangy, J. P., 1992, Integrated seismic lithologic interpretation: the petrophysical basis: Ph.D. dissertation, Stanford University, Stanford, California.

Crampin, S., Bush, I., Naville, C., and Tylor, D. B., 1986, Estimating the internal structure of reservoirs with shear-wave VSPs: The Leading Edge, **5**, 35-39.

Hudson, J. A., 1980, Overall properties of a cracked solid, Math. Proc. Cambr. Phil. Soc., **88**, 371-384.

Hudson, J. A. , 1981, Wave speeds and attenuation of elastic waves in material containing cracks, Geophys. J. Roy. Astr. Soc., **64**, 133-150.

Lorenz, J. C., Teufel, L. W., and Warpinski, N. R., 1991, Regional fractures I: a mechanism for the formation of regional fractures at depth in flat-lying reservoirs: The American Association of Petroleum Geologists Bulletin, **75**, No. 11, 1714-1737.

Nur, A., 1971, Effects of stress on velocity anisotropy in rocks with cracks, J. Geophys. Res., **76**, 2022-2034.

Mueller, M., 1992, Using shear waves to predict lateral variability in vertical fracture intensity: The leading Edge, **11**, No. 2, 29-35.

Sena, A. G., 1991, Seismic traveltime equations for azimuthally anisotropic and isotropic media: Estimation of interval elastic properties, Geophys., **56**, 2090-2101.

Thomsen, L., 1986, Weak Elastic Anisotropy: Geophys., **51**, 1954-1966.

Willis, H. A., Rethford, G. L. and Bielavski, E., 1986, Azimuthal anisotropy: occurrence and effect of shear wave data quality, paper presented at 56th Annual Meeting, Soc. of Explor. Geophys., Houston.

Yin, H., 1992, Acoustic Velocity and Attenuation of rocks: Isotropy, Intrinsic Anisotropy, and Stress Induced Anisotropy, Ph.D. dissertation, Stanford University, Stanford, California.

Chapter 2

AVO in azimuthally anisotropic media

Abstract

This chapter studies the amplitude-versus-offset (AVO) responses in azimuthally anisotropic environments. I will present simple formulas, similar to those of Banik's (1987), to estimate AVO trends. In the most general form, the result can be applied to a system of two orthorhombic layers sharing the same three orthogonal principle axes. One of the principal axes is perpendicular to the interface between the media. This model of two orthorhombic layers is a generalization of the often-used model of transverse isotropy with a vertical symmetry axis. For most practical purposes, the formulas allow us to study and interpret the azimuthal variations of AVO trends.

The effect of azimuthal anisotropy is quadratic in the sine of angle of incidence, and linear in the difference of anisotropy between the layers. When the media are only transversely isotropic, but with a horizontal symmetry axis, the AVO trends depend not only on the contrast in Thomsen's parameter δ, but also on those in ε and γ. In other words, both compressional and shear-wave anisotropy can affect AVO trends. This scenario is different from transverse isotropy that Banik (1987) and Thomsen (1993) discussed where the symmetry axis is vertical and only the contrast in δ is significant for small to medium angles of incidence.

Most AVO studies ignore the possibility that the media may be azimuthally anisotropic. However, this practice may introduce serious errors since azimuthal anisotropy has been widely observed from well logging, vertical seismic profiling (VSP) and multi-component surface seismic surveys. The contrast in Poisson's ratio is commonly recognized as the controlling factor of AVO trends. Between gas and water saturated rocks the difference in Poisson's ratio can amount to about 0.2. The contrast in parameters of anisotropy between

an isotropic rock and an azimuthally anisotropic rock, on the other hand, can easily achieve similar magnitude even when the anisotropy is weak (Thomsen, 1986). Therefore the contribution of anisotropy to AVO trends may be comparable to the contribution of different saturations of gas and water. As a consequence, when using AVO as a hydrocarbon indicator, we must make adjustments to conventional AVO analysis to eliminate the effect of azimuthal anisotropy.

2.1 Introduction

Since Ostrander (1982, 1984) demonstrated that the variation in P-wave reflection coefficient versus angle of incidence is controlled by the contrast in Poisson's ratio across the reflection plane, the technique of amplitude variation with offset (AVO) analysis has been used extensively in the seismic exploration for hydrocarbon-bearing reservoirs (e.g., Rutherford and Williams, 1989; Allen and Peddy, 1993; Fatti et al., 1994; Castagna and Smith, 1994). This technique is based on the petrophysical observation that gas-saturated sandstones have a lower Poisson's ratio than water-saturated sandstones or clays. Therefore, the amplitude of the reflected wave increases with source-receiver offset at a gas-water interface, as shown in equation (2.1) (Hilterman, 1989):

$$R_{PP} \approx R_P \cos^2\theta + 2.25\,\Delta\sigma \sin^2\theta, \tag{2.1}$$

where $R_{PP}(\theta)$ is the P-P reflection coefficient corresponding to angle of incidence θ, R_P is the reflection coefficient for normal incidence, and $\Delta\sigma$ is the contrast in Poisson's ratio. For relatively large angles, the effect of $\Delta\sigma$ becomes dominant. Castagna (1993) has provided an excellent review and a list of useful references on this subject. For a wide range of AVO-related topics, see the technical program and abstracts of the joint SEG/EAEG 1992 summer research workshop.

Most of the AVO analysis work implicitly assumes that rocks are isotropic. In reality, however, this assumption is often invalid. Many authors (Nur, 1971; Banik, 1984; Crampin et al., 1984; Thomsen, 1986; Yin, 1992; Liu, 1994) have observed that in general the elastic properties of crustal rocks are anisotropic. Elastic anisotropy of the rocks can be intrinsic when individual crystals in a rock are aligned along a preferred orientation, or when grains in a sedimentary rock such as shale are aligned during either deposition or plastic deformation (Banik, 1984; Liu, 1994). Anisotropy can also be induced by the imposition of nonhydrostatic stresses (Nur, 1971) or the inclusion of cracks or fractures (Hudson, 1980, 1981, 1991). Whatever the causes of anisotropy, the behavior of seismic waves traveling through an anisotropic medium and the AVO response at an interface depend on the direction of wave propagation, polarization, and the orientations of the symmetry axes of the anisotropy relative to the reflection interface. To interpret the AVO signature of the seismic data reliably, we must take into account the effect of elastic anisotropy on reflectivities.

Daley and Hron (1977) studied the reflection and transmission coefficients for transversely isotropic media with the symmetry axis perpendicular to the interface (TIV).

Wright (1987) showed that the effects of transverse isotropy on AVO can be significant. Thomsen (1993) gave an approximate equation of P-wave reflectivity as a function of the anisotropic parameters in weak transversely isotropic media. Blangy (1994) presented his modeling results based on realistic parameters of transversely isotropic sandstones and shales. By far most of the work on AVO in anisotropic environments has been based on the TIV model.

Although transversely isotropic rocks such as clay and shale are most commonly observed in sedimentary basins, which justifies the emphasis on TIV models, other forms of anisotropy do occur quite often. For example, shear-wave splitting, which has been reported in many VSP and surface seismic studies, indicates some form of azimuthal anisotropy (Crampin, 1987; Thomsen, 1988; Mueller, 1992). Non-TIV environments, however, have largely been ignored when doing AVO analysis. The few published studies on this topic are either modeling results based on a few special situations (Pelissier et. al. 1991; Levin, 1994), or algorithms for numerical calculation of reflection and transmission coefficients (Schoenberg and Protázio, 1992). Pelissier et al. (1991) showed with numerical modeling azimuthally varying patterns of reflectivity when the anisotropy symmetry axis is not normal to the interface. Levin (1994) presented a ray-tracing result in which large azimuthal variations of moveout velocity can be observed. Schoenberg and Protázio (1992) generalized the Zoeppritz equations to anisotropic media that allow efficient numerical computation. The results so far are not enough to give seismic interpreters the necessary understanding and tools to deal with azimuthal anisotropy.

In this chapter I derive easy-to-use formulas to compute AVO responses at the interface of anisotropic media that can be either transversely isotropic or azimuthally anisotropic. I first consider the easiest cases that are combinations of transversely isotropic media with either a vertical or a horizontal symmetry axis (TIH), and then generalize the results to other cases that include orthorhombic anisotropy. TIH may occur when an originally isotropic medium in horizontal beddings contains a parallel set of vertical fractures. This is the model used in most studies of shear-wave splitting (Thomsen, 1988). Orthorhombic anisotropy is realized when a horizontal layer of transversely isotropic rock such as shale contains parallel vertical fractures. Both TIH and orthorhombic anisotropy are better models than TIV when studying naturally fractured reservoirs.

The derivation of the formula closely matches that for TIV media (Banik, 1987). The anisotropy is assumed to be weak; otherwise the problem can only be solved numerically. The results can be used as a direct link between the azimuthal variation of AVO signatures and elastic anisotropy parameters, which are useful for both azimuthal anisotropy detection and data correction.

The rest of this chapter is organized into five sections. Section 2 reviews the basic results of studies on weak elastic transverse isotropy, which are then used in subsequent sections. Section 3 derives the approximate equations for AVO responses at the interface of several combinations of TIV and TIH media. Section 4 generalizes the result to orthorhombic media. Numerical modeling is used in section 5 to show the effectiveness of the results. Section 6 discusses some pitfalls of the approximation used in the derivation and possible applications of the results, and concludes the chapter.

2.2 Review of weak elastic anisotropy

This section briefly reviews previous work on linear elastic anisotropy that pertains to in later sections. The basic equations of elastic are well known; their approximations when the media are weakly transversely isotropic were given by Thomsen (1986), Banik (1987), and others.

2.2.1 Christoffel equation

In a linear elastic system the stress tensor σ_{ij}, strain tensor ε_{kl} and elastic modulus tensor c_{ijkl} satisfy the generalized Hooke's law (Nye, 1957) as follows:

$$\sigma_{ij} = c_{ijkl}\,\varepsilon_{kl}, \qquad i, j = 1, 2, 3. \tag{2.2}$$

This chapter uses the summation convention for repeated subscripts. Since stress and strain are symmetric and each has only six independent components, equation (2.2) can be written as

$$\sigma_I = C_{IJ}\varepsilon_J, \qquad I = 1, 2, \ldots, 6, \tag{2.3}$$

where ij or kl is mapped into I or J according to the following rule (Auld, 1973):

ij or kl	11	22	33	23 = 32	31 = 13	12 = 21
I or J	1	2	3	4	5	6

In this case C_{IJ} is a 6 by 6 symmetric matrix which can have at most 21 independent elements.

For a plane wave propagating along direction (l_1, l_2, l_3), the wave equation can be reduced to the Christoffel equation (Auld, 1973), as follows:

$$\mathbf{DCD}^{\mathrm{T}}\mathbf{v} = \rho\left(\frac{\omega}{k}\right)^2 \mathbf{v}, \qquad \mathbf{D} = \begin{bmatrix} l_1 & 0 & 0 & 0 & l_3 & l_2 \\ 0 & l_2 & 0 & l_3 & 0 & l_1 \\ 0 & 0 & l_3 & l_2 & l_1 & 0 \end{bmatrix}, \tag{2.4}$$

where $\mathbf{v}$ is the particle-motion direction for the plane-wave solutions. In a sense, the Christoffel equation is just the Fourier transform of the wave equation. $\mathbf{DCD}^{\mathrm{T}}$ is called the *Christoffel matrix*. It is a 3 by 3 matrix determined only by the direction of plane wave propagation and the elastic constants of the medium.

2.2.2 Transverse isotropy

The most often discussed form of anisotropy is transverse isotropy. It is axisymmetric about axis 3 in an appropriate coordinate system. The elastic modulus matrix of a transversely isotropic medium can be written as

$$\mathbf{C} = \begin{bmatrix} c_{11} & c_{12} & c_{13} & & & \\ c_{12} & c_{11} & c_{13} & & & \\ c_{13} & c_{13} & c_{33} & & & \\ & & & c_{44} & & \\ & & & & c_{44} & \\ & & & & & c_{66} \end{bmatrix}, \quad c_{12} = c_{11} - 2c_{66}, \tag{2.5}$$

with all the missing elements being zero.

Since axes 1 and 2 are equivalent, without losing generality we can assume $l_2 = 0$ when computing phase velocities and particle-motion directions. The Christoffel equation in this simple case then becomes

$$\begin{bmatrix} c_{11}l_1^2 + c_{44}l_3^2 & 0 & (c_{13}+c_{44})l_1l_3 \\ 0 & c_{66}l_1^2 + c_{44}l_3^2 & 0 \\ (c_{13}+c_{44})l_1l_3 & 0 & c_{44}l_1^2 + c_{33}l_3^2 \end{bmatrix} \begin{bmatrix} \mathrm{v}_1 \\ \mathrm{v}_2 \\ \mathrm{v}_3 \end{bmatrix} = \lambda \begin{bmatrix} \mathrm{v}_1 \\ \mathrm{v}_2 \\ \mathrm{v}_3 \end{bmatrix}, \quad \lambda = \rho\left(\frac{\omega}{k}\right)^2. \tag{2.6}$$

Written in this form, it is easy to see that λ is the eigenvalue of the Christoffel matrix, and $\mathbf{v} = [\mathrm{v}_1, \mathrm{v}_2, \mathrm{v}_3]^{\mathrm{T}}$ is the corresponding eigenvector. Equation (2.6) has three solutions, representing three different wave modes:

$$\begin{aligned}
\lambda_1 &= \frac{1}{2}\left(K+\sqrt{K^2-4L}\right), && \text{quasilongitudinal}\\
\lambda_2 &= \frac{1}{2}\left(K-\sqrt{K^2-4L}\right), && \text{quasishear}\\
\lambda_3 &= c_{66}l_1^2 + c_{44}l_3^2, && \text{pure shear}
\end{aligned} \tag{2.7}$$

where

$$\begin{aligned}
K &= (c_{11}+c_{44})l_1^2 + (c_{33}+c_{44})l_3^2,\\
L &= \left(c_{11}l_1^2 + c_{44}l_3^2\right)\left(c_{44}l_1^2 + c_{33}l_3^2\right) - (c_{13}+c_{44})^2 l_1^2 l_3^2.
\end{aligned}$$

2.2.3 Weak transverse isotropy

Since equations (2.7) are not intuitive enough for everyday use, further simplification is needed. Using the notations introduced by Thomsen (1986),

$$\begin{aligned}
\alpha &= \sqrt{c_{33}/\rho},\\
\beta &= \sqrt{c_{44}/\rho},\\
\varepsilon &= \frac{c_{11}-c_{33}}{2c_{33}},\\
\gamma &= \frac{c_{66}-c_{44}}{2c_{44}},\\
\delta^* &= \frac{1}{2c_{33}^2}\left[2(c_{13}+c_{44})^2 - (c_{33}-c_{44})(c_{13}+c_{33}-2c_{44})\right],\\
\delta &= \frac{(c_{13}+c_{44})^2-(c_{33}-c_{44})^2}{2c_{33}(c_{33}-c_{44})} = \frac{1}{2}\left(\varepsilon + \frac{\delta^*}{1-\kappa}\right),\\
\kappa &= \frac{\beta^2}{\alpha^2},
\end{aligned} \tag{2.8}$$

equations (2.7) become (Thomsen, 1986)

$$\begin{aligned}
v_P^2(\theta) &= \alpha^2\left(1+\varepsilon\sin^2\theta + D^*\right),\\
v_{SV}^2(\theta) &= \beta^2\left[1+\frac{1}{\kappa}\left(\varepsilon\sin^2\theta - D^*\right)\right],\\
v_{SH}^2(\theta) &= \beta^2\left(1+2\gamma\sin^2\theta\right),
\end{aligned} \tag{2.9}$$

where θ is the phase angle, and

$$D^*(\theta)=\frac{1-\kappa}{2}\left\{\left[1+\frac{4\delta^*}{(1-\kappa)^2}sin^2\theta cos^2\theta+\frac{4(1-\kappa+\varepsilon)\varepsilon}{(1-\kappa)^2}sin^4\theta\right]^{\frac{1}{2}}-1\right\}.$$

Most of the complexity comes from the term D^*. However, under the condition of weak anisotropy, which is often observed both in situ and in lab measurements, equations (2.9) can be greatly simplified as linear functions of ε, δ, and γ (Thomsen, 1986), as follows:

$$\begin{aligned} v_P(\theta) &= \alpha\left(1+\delta sin^2\theta cos^2\theta+\varepsilon sin^4\theta\right), \\ v_{SV}(\theta) &= \beta\left(1+\frac{\varepsilon-\delta}{\kappa}sin^2\theta cos^2\theta\right), \\ v_{SH}(\theta) &= \beta\left(1+\gamma sin^2\theta\right). \end{aligned} \tag{2.10}$$

Equations (2.10) are very good approximations of the exact equations (2.9) with errors proportional to the quadratic terms of ε, δ, and γ. In fact, when anisotropy is weak, we can see that the velocity surfaces of the compressional and the shear wave deviate only slightly from a perfect sphere, as shown in Figure 2.1. Hence a small linear correction to the usual tools we use in isotropic cases should suffice for most applications.

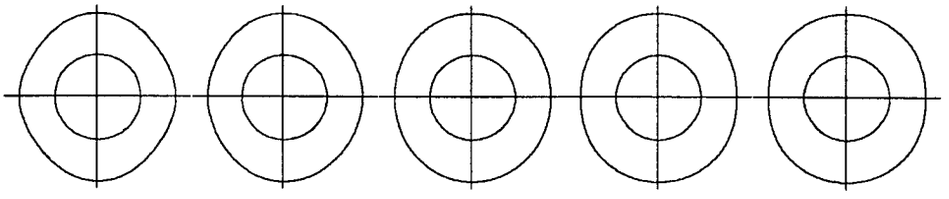

Figure 2.1: Velocity surfaces for weakly TI media. The outer curves indicate the P-wave; the inner curves, the SV wave. The parameters are $\varepsilon=0.1$, $\kappa=0.3$, and from left to right, $\delta=-0.2, -0.1, 0, 0.1, 0.2$.

2.2.4 Ray Angle

The relationship between ray angle and phase angle is illustrated in Figure 2.2. The wave vector points to the direction of maximum rate of increase in phase. At any location the wave vector is perpendicular to the wave front. The ray vector, however, points from the source point to the wave front, which is the direction of energy propagation. In an

anisotropic medium, the wave front is not spherical, and the phase angle θ is usually different from the ray angle ϕ except in the symmetry planes.

The formula for calculating the ray angle ϕ , given by Berryman (1979), is

$$tan\,\phi(\theta)=\left(tan\,\theta+\frac{1}{\mathrm{v}}\frac{d\mathrm{v}}{d\theta}\right)\Big/\left(1-\frac{tan\,\theta}{\mathrm{v}}\frac{d\mathrm{v}}{d\theta}\right). \tag{2.11}$$

Using simple trigonometry, we can write equation (2.11) as (Berryman, 1979)

$$tan(\phi(\theta)-\theta)=\frac{1}{\mathrm{v}}\frac{d\mathrm{v}}{d\theta}. \tag{2.12}$$

For weak transversely anisotropic media, the difference between ray angle ϕ and phase angle θ of the quasi-compressional wave can be obtained by substituting $\mathrm{v_P}$ in equations (2.10) for v in equation (2.12), which results in

$$\phi_{\mathrm{P}}(\theta)-\theta\approx tan(\phi_{\mathrm{P}}(\theta)-\theta)\approx sin2\theta[\varepsilon+(\delta-\varepsilon)cos2\theta]. \tag{2.13}$$

Similarly, for quasi-shear and pure shear waves, we have

$$\phi_{\mathrm{SV}}(\theta)-\theta\approx\frac{\varepsilon-\delta}{2\kappa}sin4\theta,$$
$$\phi_{\mathrm{SH}}(\theta)-\theta\approx\gamma sin2\theta.$$

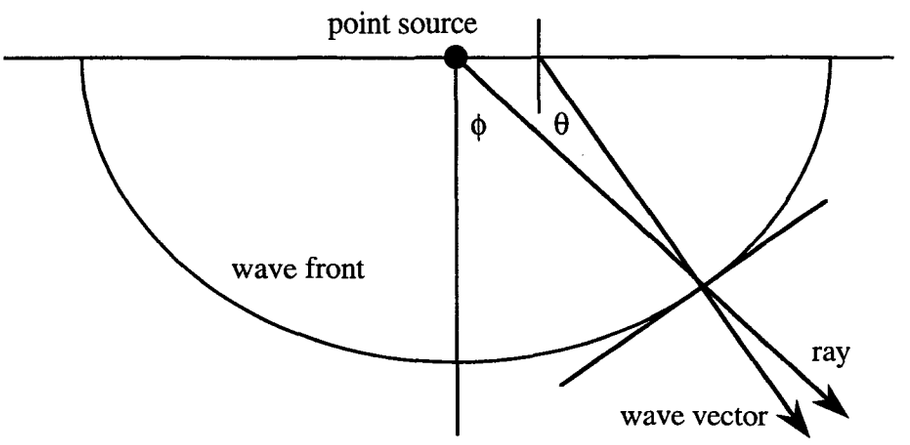

Figure 2.2: The difference between phase angle θ and group angle ϕ.

Equation (2.13) indicates that the difference between the phase angle and the group angle in a TIV environment is of the same order of magnitude as ε, δ, and γ, which amounts to less than a few degrees in most cases.

Figure 2.3 shows the variation of this difference with respect to phase angle. The trends are simple for the shear waves, which are just sinusoidal curves. The difference between the phase angle and the group angle achieves its maximum magnitude at 22.5 and 67.5 degrees angle of incidence for SV waves, and at 45 degrees angle of incidence for SH waves. For P-waves, the trend of equation (2.13) is less clear. However, since the value is controlled by $sin2\theta$, the maximum generally appears between 30 and 60 degrees angle of incidence.

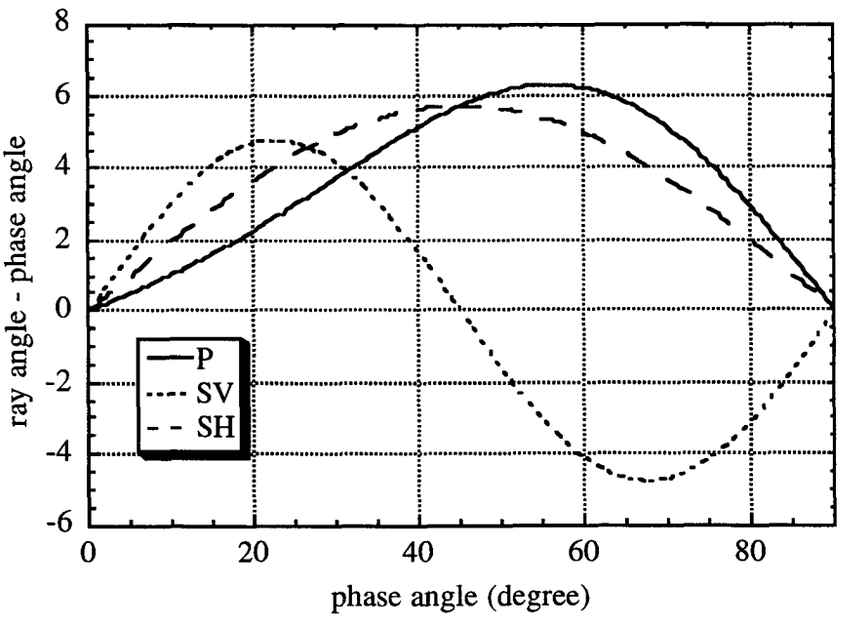

Figure 2.3: Variation of $\phi(\theta) - \theta$ with respect to phase angle θ.
Here $\varepsilon = 0.1$, $\delta = 0.05$, $\gamma = 0.1$, and $\kappa = 0.3$.

In most geophysical applications, it is the ray angle instead of the phase angle that is known. In theory we should calculate the phase angle from the ray angle using equation (2.13), and then compute the phase velocity. However, since the difference between the phase angle and the ray angle is usually very small when anisotropy is weak, equation

(2.10) is still valid to the linear terms of ε, δ, and γ, even if the ray angle is used directly. This claim can be justified for P-waves as follows:

$$\begin{aligned} v_P(\phi(\theta)) &= v_P(\theta + (\phi(\theta) - \theta)) \\ &\approx v_P(\theta) + \frac{dv_P(\theta)}{d\theta}(\phi(\theta) - \theta) \\ &\approx v_P(\theta) + \alpha \sin^2 2\theta \, [\varepsilon + (\delta - \varepsilon)\cos 2\theta]^2 \\ &\approx v_P(\theta). \end{aligned} \tag{2.14}$$

In the last step the quadratic term of ε, δ, and γ is omitted. For shear waves, we can use similar derivations to achieve the same results:

$$\begin{aligned} v_{SV}(\phi(\theta)) &\approx v_{SV}(\theta), \\ v_{SH}(\phi(\theta)) &\approx v_{SH}(\theta). \end{aligned}$$

Equation (2.14) indicates that it is unnecessary to differentiate between the ray angle and the phase angle in the case of weak transverse isotropy.

2.2.5 Group velocity

As Figure 2.2 shows, the ray velocity is different from the phase velocity at the wavefront. The magnitude of the ray velocity $\mathbf{V}$, given by Berryman (1979), is

$$V^2(\phi(\theta)) = v^2(\theta) + \left(\frac{dv}{d\theta}\right)^2. \tag{2.15}$$

$\mathbf{V}$ is also called the *group velocity* because of the similarity between equation (2.15) and the expression for group velocity in a dispersive medium.

Under the condition of weak anisotropy, equation (2.15) can be simplified as

$$\begin{aligned} V(\phi(\theta)) &= v(\theta)\left[1 + \frac{1}{v^2(\theta)}\left(\frac{dv}{d\theta}\right)^2\right]^{\frac{1}{2}} \\ &\approx v(\theta)\left[1 + \frac{1}{2v^2(\theta)}\left(\frac{dv}{d\theta}\right)^2\right] \\ &\approx v(\theta) \\ &\approx v(\phi(\theta)). \end{aligned} \tag{2.16}$$

For the approximation, the quadratic terms in anisotropy are omitted, and equations (2.14) are used in the last step.

Equation (2.16) says that in the linear approximation of weak anisotropy, the group velocity for ray angle ϕ is equal to the phase velocity obtained by using ϕ as the phase angle directly. In other words, velocity anisotropy is the first-order effect of weak anisotropy, while other effects, such as the difference between ray angle and phase angle, or between ray velocity and phase velocity, are of a higher order in anisotropy. This result greatly simplifies data processing and interpretation in a weakly anisotropic environment since velocities can be reliably obtained by stacking, whereas information about ray angles is much less accurate.

Thomsen (1986) discussed the difference between phase angles and ray angles, and concluded that

$$V(\phi(\theta)) = v(\theta).$$

However, he emphasized that given ray angle ϕ, group velocity can be obtained from equations (2.10) with phase angle θ calculated using equations (2.13). As stated by equation (2.16), the step from ray angle to phase angle is quite unnecessary since their difference is only a second-order effect.

2.3 AVO in transversely isotropic Media

This section studies the P-wave reflection coefficients in transversely isotropic media. For several reasons, most published studies of the anisotropic properties of rocks use transversely isotropic systems as the basic model (Thomsen, 1986; Liu, 1994). First, thinly-layered beddings behave as a transversely isotropic medium in the long wave-length limit (Backus, 1962). Second, shale formations in sedimentary basins are often transversely isotropic. Third, theoretical studies (Hudson, 1980) show that an isotropic medium becomes transversely isotropic when uniformly distributed parallel cracks are introduced into the system. Fourth, laboratory measurements and field seismic data often do not warrant more sophisticated models of elastic anisotropy because of limited precision and the existence of noise. Finally, transversely isotropic models have been proven quite useful, and yet they are simple enough to be algebraically manageable.

Up to now geophysicists have been interested mostly in the case where the unique symmetry axis of the transversely system is vertical. Many authors have published papers discussing, among other things, the effects of transverse isotropy with vertical symmetry axis on stacking velocities (Thomsen, 1986), depth determination of horizons (Banik, 1984), AVO trends (Banik, 1987; Thomsen, 1993; Blangy, 1994), and migration (Alkhalifah and Larner, 1994). The study of other transversely isotropic models, however,

has largely been ignored. The main difficulty is that the anisotropic system loses its axisymmetry property when the symmetry axis is not vertical.

Recently, with the increasing interest in multi-component seismology and P-wave azimuthal AVO analysis, the problem of azimuthal anisotropy has gained importance. Surface P-wave data have shown that AVO trends along different azimuth at the same location can differ significantly. The reliability of the AVO analysis on the data depends on the understanding of this phenomenon.

The Zoeppritz equations that govern the reflection and transmission coefficients at an interface are algebraically intimidating to solve analytically. Two approaches are usually taken to deal with the problem. The first is to solve the equations numerically. In this approach, the elastic constants are input to a program, usually as parameters, and the reflection and transmission coefficients are output either to files or to a graphic display. The numerical solutions for a number of isolated cases offer little help to visualize how the variation of a particular physical parameter affects the overall trend of the reflection and transmission coefficients.

The other approach, taken by Bortfeld (1961), Chapman (1976), Aki and Richards (1980), Banik (1987), and others, is to find approximate analytical solutions in terms of changes in density, P-wave velocity, shear-wave velocity, and anisotropy across the interface. Even though these approximations may be valid only for small changes in physical properties, or for a limited range of angles of incidence, they are very helpful in interpreting AVO trends.

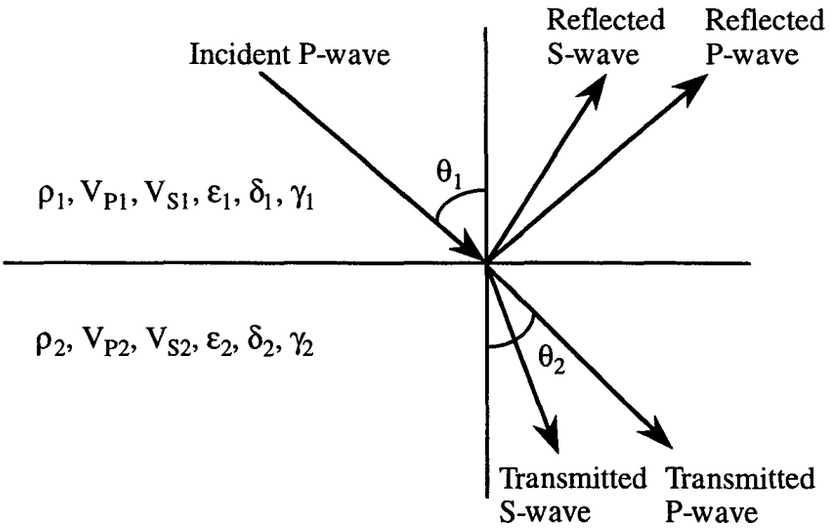

Figure 2.4: Reflected and transmitted waves from an incident P-wave at the interface of two media.

In this section I take the second approach to derive the approximate solutions for various combinations of TIV and TIH media. My main *contribution* is to give simple formulas that estimate AVO responses in azimuthally anisotropic media.

In the discussion that follows, subscripts 1 and 2 indicate the physical properties of media 1 and 2, respectively. The incident wave travels in medium 1 downward to the interface, as shown in Figure 2.4.

Aki and Richards (1980) derived a simple expression for P-P reflectivity at the interface of two isotropic media, as follows:

$$R_{PP}(\theta) \approx \frac{1}{2}\left(1-4p^2V_S^2\right)\frac{\Delta\rho}{\rho}+\frac{1}{2cos^2\theta}\frac{\Delta V_P}{V_P}-4p^2V_S^2\frac{\Delta V_S}{V_S}, \qquad (2.17)$$

where

$$\begin{aligned}
\Delta\rho &= \rho_2-\rho_1,\\
\Delta V_P &= V_{P2}-V_{P1},\\
\Delta V_S &= V_{S2}-V_{S1},\\
\rho &= (\rho_1+\rho_2)/2,\\
V_P &= (V_{P1}+V_{P2})/2,\\
V_S &= (V_{S1}+V_{S2})/2,\\
\theta &= (\theta_1+\theta_2)/2,\\
p &= sin\,\theta_1/V_{P1}.
\end{aligned}$$

In other words, $\Delta\rho$, ΔV_P and ΔV_S are differences in density, P-wave velocity and shear-wave velocity, respectively; ρ, V_P, and V_S are average density, and average P-wave and shear-wave velocities across the interface, respectively; and p is the ray parameter. Equation (2.17) assumes that the angle of incidence θ is not close to 90 degrees; it also requires that the jumps in physical properties of the media be small, that is, the magnitudes of the ratios $\Delta\rho/\rho$, $\Delta V_P/V_P$ and $\Delta V_S/V_S$ be much smaller than one. These conditions are often satisfied in applications of AVO analysis.

Equation (2.17) can be generalized to accommodate cases of weak anisotropy if the velocities in the expression are allowed to vary with the angle of incidence. This generalization is equivalent to linearizing the Zoeppritz equations in terms of $\Delta\rho(\theta)$, $\Delta V_P(\theta)$, and $\Delta V_S(\theta)$ at each angle of incidence, and then solving for reflection coefficient $R_{PP}(\theta)$. As a further step of approximation, angle of incidence θ_1 is used in equation (2.17) instead of angle θ.

2.3.1 AVO in TIH environments

First let us consider the case of a transversely isotropic medium over another transversely isotropic medium. The symmetry axes of both media are horizontal and parallel to one another. In the intrinsic coordinate system of the media, the Thomsen's parameters are ε_1, δ_1, γ_1, and ε_2, δ_2, γ_2, respectively. In such an environment, the P-P reflection coefficient varies not only with the angle of incidence, but also with the azimuth ϕ, which is measured from the symmetry axis. For simplicity I assume that the symmetry axis is parallel to the x-axis, and the z-axis is vertical.

There are two symmetry planes in this system, which are both vertical. The common symmetry axis lies within one symmetry plane (0° azimuth) and is perpendicular to the other (90° azimuth). The quasishear and pure shear waves are coupled at the reflection point unless they are in the symmetry planes. For this reason we need to consider the P-P reflection coefficient in these two planes first.

In the symmetry plane with zero-degree azimuth, the P-wave velocity as a function of angle θ from the vertical axis can be obtained from equations (2.10) as

$$\begin{aligned} V_P(\theta) &= v_P(90°-\theta) \\ &\approx \alpha\left(1+\delta sin^2\theta cos^2\theta+\varepsilon cos^4\theta\right) \\ &= \alpha\left[1+\varepsilon+(\delta-2\varepsilon)sin^2\theta cos^2\theta-\varepsilon sin^4\theta\right], \end{aligned} \tag{2.18-a}$$

and similarly, from equations (2.10) the shear-wave velocity is

$$V_S(\theta) = v_{SV}(90°-\theta) \approx \beta\left(1+\frac{\varepsilon-\delta}{\kappa}sin^2\theta cos^2\theta\right). \tag{2.18-b}$$

Equations (2.18) can be used for both TIH media.

From equations (2.18), the ratios $\Delta V_P(\theta)/V_P(\theta)$ and $\Delta V_S(\theta)/V_S(\theta)$ can be written, to the order of quadratic in $sin\theta$ and linear in $\Delta V_P(0)$, $\Delta V_S(0)$, ε_1, δ_1, γ_1, ε_2, δ_2, and γ_2 as

$$\frac{\Delta V_P(\theta)}{V_P(\theta)} \approx \frac{\Delta V_P(0)}{V_P(0)} + (\Delta\delta-2\Delta\varepsilon)sin^2\theta, \tag{2.19-a}$$

and

$$\frac{\Delta V_S(\theta)}{V_S(\theta)} \approx \frac{\Delta V_S(0)}{V_S(0)} + \frac{\Delta\varepsilon-\Delta\delta}{\kappa}sin^2\theta. \tag{2.19-b}$$

Specifically, for vertically traveling rays,

$$\begin{cases} V_{Pi}(0) = \alpha_i(1+\varepsilon_i), \\ V_{Si}(0) = \beta_i, \end{cases} \qquad i = 1, 2. \tag{2.20}$$

If we combine equations (2.19) and (2.20), at zero-degree azimuth the P-P reflection coefficient as a function of angle of incidence in TIH-TIH environment is

$$\begin{aligned} R_{PP}(0,\theta) \approx & \frac{1}{2}\left(\frac{\Delta\rho}{\rho} + \frac{\Delta V_P(0)}{V_P(0)}\right) \\ & - 2\frac{V_S^2(0)}{V_P^2(0)}\left(\frac{\Delta\rho}{\rho} + 2\frac{\Delta V_S(0)}{V_S(0)}\right)\sin^2\theta + \frac{1}{2}\frac{\Delta V_P(0)}{V_P(0)}\tan^2\theta \\ & + \frac{\Delta\delta - 2\Delta\varepsilon}{2}\sin^2\theta, \end{aligned} \tag{2.21}$$

where $V_P(0)$ and $V_S(0)$ refer to the average of the vertical P and S-wave velocities as in equations (2.21), and Δ refers to the contrast. Notice that the polarization of the shear-wave lies within the symmetry plane containing the symmetry axis.

The first term on the right-hand side of equation (2.21) represents the reflection coefficient at normal incidence; the second and the third terms are the influence of non-normal incidence in an isotropic media; and the last term is the contribution of azimuthal anisotropy.

In the other symmetry plane, with 90-degree azimuth, things are much simpler. The P-wave and shear-wave velocities stay constant within the plane. The velocity for P-wave is

$$V_{Pi}(\theta) = v_{Pi}(0°) \approx \alpha_i(1+\varepsilon_i), \qquad i = 1, 2. \tag{2.22-a}$$

However, for shear-wave velocity there is a catch. Since the plane is perpendicular to the symmetry axis, the velocity of the pure-shear wave should be used, that is,

$$V_{Si}'(\theta) = v_{SHi}(90°) = \beta_i(1+\gamma_i), \qquad i = 1, 2. \tag{2.22-b}$$

The reflection coefficient at 90-degree azimuth is

$$\begin{aligned} R_{PP}(90,\theta) \approx & \frac{1}{2}\left(\frac{\Delta\rho}{\rho} + \frac{\Delta V_P(0)}{V_P(0)}\right) \\ & - 2\frac{V_S^2(0)}{V_P^2(0)}\left(\frac{\Delta\rho}{\rho} + 2\frac{\Delta V_S(0)}{V_S(0)}\right)\sin^2\theta + \frac{1}{2}\frac{\Delta V_P(0)}{V_P(0)}\tan^2\theta \\ & - 4\frac{V_S^2(0)}{V_P^2(0)}\Delta\gamma\sin^2\theta. \end{aligned} \tag{2.23}$$

The first three terms on the right-hand side of equation (2.23) are the same as those of equation (2.21). The last term is the effect of different shear-wave modes participating in the reflection process.

Equations (2.21) and (2.23) are obtained under the conditions of weak anisotropy, small contrast in velocity and density, and small angle of incidence. They can be applied reliably only when these conditions are satisfied. Fortunately, these conditions are not hard to satisfy: the earth is often weakly anisotropic; the physical properties of beddings do not change abruptly very often; and the useful range of angle of incidence in seismic exploration is usually not very large.

It is often useful to be able to estimate AVO trends along azimuth other than 0 or 90 degrees, since the seismic survey lines may not lie exactly in these directions. In non-symmetry planes, the equations of reflection and transmission coefficients are far more complicated because all three wave modes are coupled together. To my knowledge no serious effort has been made to derive analytical solutions for non-trivial cases in a non-TIV environment. However, useful results can be obtained with little extra effort. We know that in TIH-TIH media with a unique symmetry axis, reflectivity $R_{PP}(\phi, \theta)$ is a periodic function of azimuth ϕ with period π. If we expand $R_{PP}(\phi, \theta)$ into a Taylor series and keep the terms up to the order of quadratic in $sin\phi$ and $cos\phi$, we can write the reflection coefficient as

$$\begin{aligned} R_{PP}(\varphi, \theta) \approx & \frac{1}{2}\left(\frac{\Delta\rho}{\rho} + \frac{\Delta V_P(0)}{V_P(0)}\right) \\ & - 2\frac{V_S^2(0)}{V_P^2(0)}\left(\frac{\Delta\rho}{\rho} + 2\frac{\Delta V_S(0)}{V_S(0)}\right) sin^2\theta + \frac{1}{2}\frac{\Delta V_P(0)}{V_P(0)} tan^2\theta \\ & + \left[\frac{\Delta\delta - 2\Delta\varepsilon}{2} cos^2\varphi - 4\frac{V_S^2(0)}{V_P^2(0)}\Delta\gamma sin^2\varphi\right] sin^2\theta. \end{aligned} \tag{2.24}$$

Equation (2.24) is in essence an interpolation that fits the result in the symmetry planes. When anisotropy is weak, the reflectivity functions deviate only slightly from isotropic cases. Hence I believe this approximation should be fine for most applications. In section 5 I shall show that numerically the approximation is reasonably good.

In equations (2.21), (2.23), and (2.24), the reflectivity coefficient is expressed as the total of small changes caused by the contrasts in physical properties. The fact that reflection coefficients depend on these contrasts should not be a surprise. The basic equation in our discussion, equation (2.17), comes from linearizing the solution of the Zoeppritz equations as a weighted summation of the contrasts.

Several observations can be readily made from equations (2.21), (2.23), and (2.24):

- The effect of azimuthal anisotropy is quadratic in $sin\,\theta$. It can be comparable to the effect of the contrasts in density and velocity in isotropic cases. Banik (1987) made the same observation for TIV-TIV environments.
- The effect of anisotropy depends on the contrast in anisotropy parameters. Therefore, the effect is often most visible at the boundary between an isotropic or TIV medium and a TIH medium where the changes in anisotropic parameters are often the greatest. On the other hand, if the media across the interface have the same amount of anisotropy, the effect of anisotropy on reflection coefficients is negligible. As a comparison, the effect of anisotropy in TIV media depends on the contrast in δ (Banik, 1987).
- The reflection coefficient is a function of both azimuth and angle of incidence. This fact may be used to correct the results of conventional AVO analysis. A potentially more important application is to detect azimuthal anisotropy caused by natural fractures in the absence of multi-component shear-wave data, provided that azimuthal variations of AVO trends can be obtained from (3-D) P-wave data.
- All three anisotropy parameters, ε, δ, and γ, contribute to the P-P reflection coefficient. However, with certain combinations of the parameters, their effects may cancel out, resulting in no apparent azimuthal variation at all.
- The contours of reflection coefficients are very close to ellipses at small angles of incidence. Only a small number of parameters determine the shape of the ellipses. This fact can be exploited by statistical methods during data processing when there are a large number of samples with a low signal-to-noise ratio.

The feasibility of detecting azimuthal anisotropy from AVO analysis depends on the difference between the reflectivity curves in both symmetry planes. The difference, referred to as the *amplitude* of azimuthal variation of reflection coefficient in this chapter, is given by:

$$R_{pp}(0°,\theta) - R_{pp}(90°,\theta) \approx \left(\frac{\Delta\delta - 2\Delta\varepsilon}{2} + 4\kappa\Delta\gamma\right) sin^2\,\theta. \qquad (2.25)$$

Azimuthal variation is detectable only when $\left(\frac{\Delta\delta - 2\Delta\varepsilon}{2} + 4\kappa\Delta\gamma\right)$ is large enough to cause measurable differences in AVO trends, otherwise the isotropic terms dominate.

2.3.2 Another point of view

An approximation of the reflection coefficient for TIV media, given by Thomsen (1993), is

$$\begin{aligned} R_{PP}(\theta) \approx & \frac{1}{2}\left(\frac{\Delta\rho}{\rho}+\frac{\Delta V_P(0)}{V_P(0)}\right) \\ & -2\frac{V_S^2(0)}{V_P^2(0)}\left(\frac{\Delta\rho}{\rho}+2\frac{\Delta V_S(0)}{V_S(0)}\right)\sin^2\theta+\frac{1}{2}\frac{\Delta V_P(0)}{V_P(0)}\tan^2\theta \\ & +\frac{\Delta\delta}{2}\sin^2\theta-\frac{1}{2}(\Delta\delta-\Delta\varepsilon)\sin^2\theta\tan^2\theta. \end{aligned} \tag{2.26}$$

This solution is good not only for small angles of incidence, but also for relatively large angles. Similar results can be obtained for TIH media if we follow the derivations outlined by Thomsen (1993). However, given equation (2.12), a simpler method exists.

Let us consider the elastic moduli of a TIH medium as in equation (2.5). In the natural coordinate system where x-axis is the symmetry axis, the matrix of the elastic constants is

$$\mathbf{C}=\begin{bmatrix} \underline{c_{33}} & c_{13} & c_{13} & & & \\ c_{13} & c_{11} & c_{12} & & & \\ c_{13} & c_{12} & \underline{c_{11}} & & & \\ & & & c_{66} & & \\ & & & & \underline{c_{44}} & \\ & & & & & c_{44} \end{bmatrix}, \quad c_{12}=c_{11}-2c_{66}, \tag{2.27}$$

where c_{ij}'s are the elements of the elastic matrix expressed in the intrinsic coordinate system. Since we are interested only in the waves traveling inside the xz-plane, only the underlined stiffness constants appear in the equations governing the reflection and transmission coefficients. We can construct an elastic matrix as

$$\mathbf{C}'=\begin{bmatrix} c_{33} & * & c_{13} & & & \\ * & c_{33} & c_{13} & & & \\ c_{13} & c_{13} & c_{11} & & & \\ & & & c_{44} & & \\ & & & & c_{44} & \\ & & & & & * \end{bmatrix}. \tag{2.28}$$

$\mathbf{C}'$ looks like the elastic matrix of a transversely isotropic medium and gives the same reflection coefficients for waves traveling inside the xz-plane.

The Thomsen's parameters of the hypothetical medium are

$$\varepsilon' = \frac{c_{33}-c_{11}}{2c_{11}} = -\frac{\varepsilon}{1+2\varepsilon} \approx -\varepsilon,$$
$$\delta' = \frac{(c_{13}+c_{44})^2-(c_{11}-c_{44})^2}{2c_{11}(c_{11}-c_{44})} = \frac{\delta-2\varepsilon}{1+\frac{4-2\kappa}{1-\kappa}\varepsilon} \approx \frac{\delta-2\varepsilon}{1+5\varepsilon}, \tag{2.29}$$

where δ and ε are the anisotropy parameters of the original TIH medium. We can use the newly defined ε' and δ', and equation (2.27) to calculate the reflection coefficients.

Notice that δ' is not quite equal to $\delta - 2\varepsilon$, as suggested in equation (2.21). However, under the condition of weak anisotropy, using equation (2.21) is often good enough. When greater accuracy is needed, we should use equation (2.27) together with equations (2.29).

2.3.3 TIV medium over TIH medium

When a TIV medium lies over a TIH medium, the P-wave reflection coefficients can be obtained by combining equations (2.25) and (2.27). The result is

$$\begin{aligned} R_{PP}(\varphi,\theta) \approx & \frac{1}{2}\left(\frac{\Delta\rho}{\rho}+\frac{\Delta V_P(0)}{V_P(0)}\right) \\ & -2\frac{V_S^2(0)}{V_P^2(0)}\left(\frac{\Delta\rho}{\rho}+2\frac{\Delta V_S(0)}{V_S(0)}\right)\sin^2\theta+\frac{1}{2}\frac{\Delta V_P(0)}{V_P(0)}\tan^2\theta \\ & +\left[\frac{\Delta\delta-2\varepsilon_2}{2}\cos^2\varphi-4\frac{V_S^2(0)}{V_P^2(0)}\gamma_2\sin^2\varphi\right]\sin^2\theta. \end{aligned} \tag{2.30}$$

Similar equation exists for the case where a TIH medium lies over a TIV medium.

2.4 AVO in Non-TI Media

The discussion in the previous section assumes that the media are transversely isotropic. For most applications transverse isotropy is the first model to consider. However, there are many other forms of elastic anisotropy. When different anisotropy-inducing factors such as fine layers, fractures, and stress are superposed, anisotropy of more general forms may result. This section studies P-wave reflection coefficients in more general systems of anisotropy.

The behaviors of the waves in arbitrarily anisotropic media are worth studying because not all rocks are transversely isotropic. The knowledge of AVO trends in anisotropic environments in general not only will contribute to our understanding of the AVO problem,

but also can be used to estimate the inaccuracy of conventional AVO techniques and reduce the risk of the decisions based on the AVO analyses.

We can easily imagine many scenarios where more general models of anisotropy are necessary. For example, the stress fields of the earth crust are seldom isotropic (hydrostatic) (Zoback, 1990), and stress anisotropy may cause rocks to behave as anisotropic media by preferentially opening or closing microcracks (Nur, 1972; Yin, 1993). This stress-induced anisotropy is independent of that of finely-layered sediments. When the two effects are combined together, the resulting system will be determined not only by each individual effect, but also by their relative spatial orientation. The most interesting case, in my opinion, is the inclusion of natural fractures in layers of shales and sandstones. Different fracture distributions and orientations may result in different anisotropic systems. By studying the anisotropic properties of the media using surface seismic exploration, VSP, or other techniques, field geophysicists may be able to identify fractured regions. The hope is that in fractured areas the permeability is high enough to enhance oil and gas production. Fracture identification is especially important in tight gas reservoirs where practically the only means to extract gas is by utilizing the enhanced drainage provided by natural fractures.

This section first briefly introduces different kinds of anisotropic systems, and then derives P-wave reflection coefficients for a subset of the systems.

2.4.1 Systems of anisotropy

To generalize the results in section 3 to other anisotropic systems, we have to study the symmetry systems themselves first. The basic description of the symmetry systems can be found in textbooks on crystallography (e.g. Bhagavantam, 1966). Here I briefly outline the ideas using the notation developed previously.

The anisotropic symmetry systems are characterized by the constraints on the stiffness constants. To find these constraints, the following argument is used: if the medium itself is physically symmetric with respect to a certain coordinate transformation, then the stiffness matrix must be invariant under the same transformation. Here only point transformations are considered. A *point transformation* is a linear coordinate transformation such that at least one point is unchanged after the transformation. Rotations, reflections, inversions, and their compositions are all point transformations. When describing rotation symmetries, the smallest possible symmetry rotation is used. An n-fold rotation symmetry means that the medium is symmetric under a rotation of angle

$2\pi/n$. In crystallography only 2-fold, 3-fold, 4-fold, and 6-fold rotation symmetries are possible.

For crystals there are only a small number of different symmetry systems, which are determined by the spatial patterns of the crystal lattice. Even though rocks are anisotropic for different reasons than crystals, the results in crystallography are still valid because the mathematics is similar. Borrowing these results, we can describe the major symmetry systems as:

- *triclinic*: A triclinic system has no symmetry at all. Its stiffness matrix has 21 constants. The only constraints on the elastic constants are inequality relations from basic solid physics and thermodynamics considerations.
- *monoclinic*: A monoclinic system has a single two-fold symmetry axis. Its stiffness matrix has 13 constants.
- *orthorhombic*: An orthorhombic system has three orthogonal two-fold symmetry axes. Its stiffness matrix has nine constants.
- *tetragonal*: An tetragonal system has a single 4-fold symmetry axes. Its stiffness matrix has seven independent constants in general. If a tetragonal system has a 2-fold axis perpendicular to the 4-fold axis, then one elastic constant vanishes, and only six independent constants are needed.
- *trigonal*: A trigonal system has a single 3-fold symmetry axis. Its stiffness matrix has 7 constants. If a trigonal system has a 2-fold axis perpendicular to the 3-fold axis, then one elastic constant vanishes, leaving only six independent constants.
- *hexagonal*: A hexagonal system has a single 6-fold symmetry axis. In addition, every axis perpendicular to the 6-fold axis is a 2-fold axis. Five stiffness constants are required to describe the system. The hexagonal systems are often called transversely isotropic in geophysics publications.
- *cubic*: A cubic system can be characterized by three stiffness constants. Its stiffness matrix has the same form as an isotropic system, except that the three constants do not satisfy the equality relation governing those of an isotropic system.

The stiffness matrices of these anisotropic systems are listed in appendix A.

We can see from appendix A that many symmetry systems have similar stiffness matrices as transversely isotropic systems discussed in section 2. By "similar" we mean that the non-zero elastic constants appear in exactly the same positions in the stiffness matrices of the systems. These systems include orthorhombic, hexagonal and cubic systems, and a subset of tetragonal systems. In the most general cases the stiffness matrix of these systems has the form

$$\mathbf{C}=\begin{bmatrix} c_{11} & c_{12} & c_{13} & & & \\ c_{12} & c_{22} & c_{23} & & & \\ c_{13} & c_{23} & c_{33} & & & \\ & & & c_{44} & & \\ & & & & c_{55} & \\ & & & & & c_{66} \end{bmatrix}, \tag{2.31}$$

where some equality relations may exist between certain elastic constants.

2.4.2 AVO in orthorhombic media

It is relatively easy to generalize the results in the previous section to these anisotropic systems. Basically, the waves of the two shear modes traveling inside the symmetry planes are decoupled, and for all practical purposes the medium behaves as if it were transversely isotropic. Within the symmetry planes, we can find the phase velocities of the P and shear-waves by explicitly solving the Christoffel equation. Then the reflection coefficients are derived as in section 2. Finally, the results are interpolated for waves traveling in an arbitrary azimuth.

The Christoffel equation for a medium with stiffness matrix (2.31) is

$$\begin{bmatrix} c_{11}l_1^2+c_{66}l_2^2+c_{55}l_3^2 & (c_{12}+c_{66})l_1l_2 & (c_{13}+c_{55})l_3l_1 \\ (c_{12}+c_{66})l_1l_2 & c_{66}l_1^2+c_{22}l_2^2+c_{44}l_3^2 & (c_{44}+c_{23})l_2l_3 \\ (c_{13}+c_{55})l_3l_1 & (c_{44}+c_{23})l_2l_3 & c_{55}l_1^2+c_{44}l_2^2+c_{33}l_3^2 \end{bmatrix}\begin{bmatrix} \mathrm{v}_1 \\ \mathrm{v}_2 \\ \mathrm{v}_3 \end{bmatrix}=\rho\left(\frac{\omega}{k}\right)^2\begin{bmatrix} \mathrm{v}_1 \\ \mathrm{v}_2 \\ \mathrm{v}_3 \end{bmatrix}. \tag{2.32}$$

Equation (2.32) can be greatly simplified by letting l_2 vanish, restricting our attention to waves traveling inside the xz-plane. By repeating the process in section 2, the velocities of P and shear waves are

$$\begin{aligned} \mathrm{v}_{Px}(\theta) &= \alpha_0\left(1+\delta_x \sin^2\theta\cos^2\theta+\varepsilon_x \sin^4\theta\right), \\ \mathrm{v}_{SVx}(\theta) &= \beta_0\left(1+\frac{\varepsilon_x-\delta_x}{\kappa}\sin^2\theta\cos^2\theta\right), \end{aligned} \tag{2.33}$$

where the anisotropy parameters are defined as follows:

$$\begin{aligned}
\alpha_0 &= \sqrt{c_{33}/\rho}\,, \\
\beta_0 &= \sqrt{c_{55}/\rho}\,, \\
\varepsilon_x &= \frac{c_{11}-c_{33}}{2c_{33}}, \\
\delta_x &= \frac{(c_{13}+c_{55})^2-(c_{33}-c_{55})^2}{2c_{33}(c_{33}-c_{55})}, \\
\kappa &= \frac{\beta_0^2}{\alpha_0^2}=\frac{c_{55}}{c_{33}}.
\end{aligned} \tag{2.34}$$

Similarly, by letting l_3 be zero, we can find the velocities of waves traveling inside the yz-plane as

$$\begin{aligned}
v_{Py}(\theta) &= \alpha_0\left(1+\delta_y \sin^2\theta\cos^2\theta+\varepsilon_y \sin^4\theta\right), \\
v_{SVy}(\theta) &= \beta_0\left(1+\gamma_{xy}+\frac{\varepsilon_y-\delta_y}{\kappa}\sin^2\theta\cos^2\theta\right),
\end{aligned} \tag{2.35}$$

with parameters ε_y , δ_y and γ_{xy} defined as

$$\begin{aligned}
\varepsilon_y &= \frac{c_{22}-c_{33}}{2c_{33}}, \\
\delta_y &= \frac{(c_{23}+c_{44})^2-(c_{33}-c_{44})^2}{2c_{33}(c_{33}-c_{44})}, \\
\gamma_{xy} &= \frac{c_{44}-c_{55}}{2c_{55}}.
\end{aligned} \tag{2.36}$$

In fact, in each of the symmetry planes, an equivalent transversely isotropic elastic matrix can be constructed similar to equation (2.28). The anisotropic parameters ε_x and δ_x are just the Thomsen's parameters for the equivalent TIV media in the xz-plane, and ε_y and δ_y in the yz-plane. The parameter γ_{xy} represents the velocity anisotropy between two shear-wave modes traveling along z-axis.

Combining wave velocities and equation (2.27), we can get the reflection coefficients for wave traveling inside the symmetry planes. Interpolating the approximate equation over azimuth, the P-wave reflection coefficient in orthorhombic environments as a function of azimuth φ and angle of incidence θ is

$$
\begin{aligned}
R_{PP}(\varphi,\theta) \approx & \frac{1}{2}\left(\frac{\Delta\rho}{\rho}+\frac{\Delta V_P}{V_P}\right) \\
& -2\frac{V_S^2}{V_P^2}\left(\frac{\Delta\rho}{\rho}+2\frac{\Delta V_S}{V_S}\right)\sin^2\theta+\frac{1}{2}\frac{\Delta V_P}{V_P}\tan^2\theta \\
& +\left[\frac{\Delta\delta_x}{2}\cos^2\varphi+\frac{\Delta\delta_y}{2}\sin^2\varphi-4\frac{V_S^2}{V_P^2}\Delta\gamma_{xy}\sin^2\varphi\right]\sin^2\theta \\
& -\left[\frac{\Delta\delta_x-\Delta\varepsilon_x}{2}\cos^2\varphi+\frac{\Delta\delta_y-\Delta\varepsilon_y}{2}\sin^2\varphi\right]\sin^2\theta\tan^2\theta,
\end{aligned}
\tag{2.37}
$$

where V_P and V_S refer to α_0 and β_0, respectively.

2.4.3 Special cases

Equation (2.37) is the general solution for the systems with stiffness matrix in the form of equation (2.31). Solutions for special cases, specifically equations (2.25) and (2.30), can be easily derived from this general solution.

1) Transverse isotropy with a vertical symmetry axis

For the trivial case of transverse isotropy with a vertical symmetry axis, the reduction from equation (2.37) to Banik's equation (Banik, 1987) is straightforward. The shear-wave anisotropy term in equation (2.37) vanishes because any vertical plane is a symmetry plane, and all symmetry planes are identical.

Using equations (2.34) and (2.36), the anisotropy parameters are

$$
\begin{aligned}
\alpha_0 &= \alpha \\
\beta_0 &= \beta \\
\varepsilon_x &= \varepsilon_y = \varepsilon \\
\delta_x &= \delta_y = \delta \\
\gamma_{xy} &= 0,
\end{aligned}
\tag{2.38}
$$

where α, β, ε, and δ are parameters conventionally defined for transverse isotropy as in equations (2.8). By substituting anisotropy parameters in equation (2.37) with those in equations (2.38), we can write the contribution of transverse isotropy to P-wave reflectivity as

$$
\frac{\Delta\delta}{2}\sin^2\theta-\frac{\Delta\delta-\Delta\varepsilon}{2}\sin^2\theta\tan^2\theta,
$$

which is exactly the same as given by Thomsen (1993).

2) Transverse isotropy with a horizontal symmetry axis

This special case is the topic of entire section 3. Here, however, the derivation is very simple. We assume the natural coordinate system where the symmetry axis is parallel to the x-axis. The stiffness matrix, written in this coordinate system, has the form of equation (2.27).

The anisotropy parameters are

$$\begin{aligned}
\varepsilon_x &= \frac{c_{33}-c_{11}}{2c_{11}} = \varepsilon', \\
\delta_x &= \frac{(c_{13}+c_{44})^2-(c_{11}-c_{44})^2}{2c_{11}(c_{11}-c_{44})} = \delta', \\
\varepsilon_y &= 0, \\
\delta_y &= 0, \\
\gamma_{xy} &= \frac{c_{66}-c_{44}}{2c_{44}} = \gamma,
\end{aligned}$$

where ε' and δ' are defined in equations (2.29), and γ is the regular Thomsen's parameter of shear-wave anisotropy.

3) Transversely isotropic layers with orthogonal horizontal symmetry axes

For this special case both the upper and the lower layers are transversely isotropic with a horizontal symmetry axis, and the symmetry axes of the two layers are perpendicular to each other. This model is useful when two orthogonal sets of unidirectional natural fractures exist in the rock matrix, but within each layer a different set of fractures are open for some reason.

For simplicity I assume that the symmetry axis of the upper layer lies in x-direction, and the symmetry axis of the lower layer in y-direction. The stiffness matrix of the upper layer has the same form as equation (2.27), and that of the lower layer is

$$\begin{bmatrix}
c_{11} & c_{13} & c_{12} & & & \\
c_{13} & c_{33} & c_{13} & & & \\
c_{12} & c_{13} & c_{11} & & & \\
 & & & c_{44} & & \\
 & & & & c_{66} & \\
 & & & & & c_{44}
\end{bmatrix}, \quad c_{12} = c_{11} - 2c_{66}.$$

The anisotropy parameters of the lower layer are

$$\begin{aligned}
\varepsilon_x &= 0, \\
\delta_x &= 0, \\
\varepsilon_y &= \frac{c_{33}-c_{11}}{2c_{11}} = \varepsilon_2', \\
\delta_y &= \frac{(c_{13}+c_{44})^2-(c_{11}-c_{44})^2}{2c_{11}(c_{11}-c_{44})} = \delta_2', \\
\gamma_{xy} &= \frac{c_{44}-c_{66}}{2c_{66}} = -\frac{\gamma_2}{1+2\gamma_2} \approx -\gamma_2,
\end{aligned}$$

where the subscript 2 refers to the lower layer.

By substituting the generalized anisotropy parameters in equation (2.37) with the above results, we obtain the anisotropic term in the reflection coefficient as

$$\left[-\frac{\delta_1'}{2}cos^2\phi + \frac{\delta_2'}{2}sin^2\phi + 4\frac{V_S^2}{V_P^2}(\gamma_2+\gamma_1)sin^2\phi\right]sin^2\theta.$$

2.5 Numerical modeling

It is always a concern how good are the approximate equations derived in the previous sections compared to the exact solutions of the Zoeppritz equations. In this section I use numerical modeling to demonstrate that the approximation is reasonably good.

Since the first three terms of equation (2.37) are the contribution from isotropy and the last two terms from anisotropy, the accuracy of equation (2.37) depends on the accuracy of these two parts. To show that my estimation on azimuthal anisotropy is good, I treat the contribution from isotropy as the background and plot the difference between reflectivity curves along different azimuth.

The numerical solutions of the Zoeppritz equations are computed using a program written by Schulz (1994). The program takes as input the density and the stiffness matrix of two layers, and the desired azimuth and the mode of the incident and reflected waves. It outputs the reflectivity as a function of angle of incidence.

For comparison I use the same models as Banik (1987) did. For all the tests the vertical P-wave velocity remains unchanged. The shear-wave has two different modes. In TIH environments I keep the velocity of the vertical pure-shear wave equal to the original shear-wave velocity of the model.

In all the plots in this section, solid curves represent the reflection coefficient or its azimuthal variation obtained from numerically solving the Zoeppritz equations, and the dotted curves the estimation using equation (2.37).

2.5.1 Model 1

Model 1 is the sand-shale model used in Wright (1987) and later in Banik (1987). The density and the velocity of the upper and lower layers are

$$\rho_1 = 2.25 g/cm^3 \;\; \alpha_1 = 2896 m/s \;\; \beta_1 = 1402 m/s,$$
$$\rho_2 = 2.25 g/cm^3 \;\; \alpha_2 = 3322 m/s \;\; \beta_2 = 1402 m/s.$$

The Poisson's ratio of the two layers is 0.3469 and 0.3916, respectively. Since the lower layer has a higher Poisson's ratio, we expect the reflection coefficient to increase with angle of incidence.

Figure 2.5 shows the P-wave reflection coefficient for the isotropic background. I only plot the curves to 45 degrees angle of incidence because that is often more than enough for surface seismic exploration. As we can see in Figure 2.5, even in isotropic environment the estimated reflection coefficient is by no means perfect for medium range angles. In general this kind of match is about what we can get without solving the Zoeppritz equations.

Next I slightly change the stiffness matrix of the lower layer to make it transversely isotropic with its symmetry axis in the x-direction. The change is made in such a way that in the vertical direction the velocities of the P-wave and the shear-wave with polarization perpendicular to the symmetry axis remain unchanged.

For the first case the Thomsen's parameters of the lower layer, defined in its intrinsic coordinate system, are

$$\varepsilon_2 = \delta_2 = \gamma_2 = 0.1.$$

In the 90-degree azimuth symmetry plane the reflection coefficient curve is the same as that in Figure 2.5.

Figures 2.6 shows the difference between the reflectivity curve along 0-degree azimuth and that along 90-degree azimuth. For this example, the contribution of azimuthal anisotropy to reflection coefficient is negligible because $\delta - 2\varepsilon + \gamma$ vanishes. This observation is true in general. The azimuthal variation of reflection coefficient increases with the absolute value of $\delta - 2\varepsilon + \gamma$.

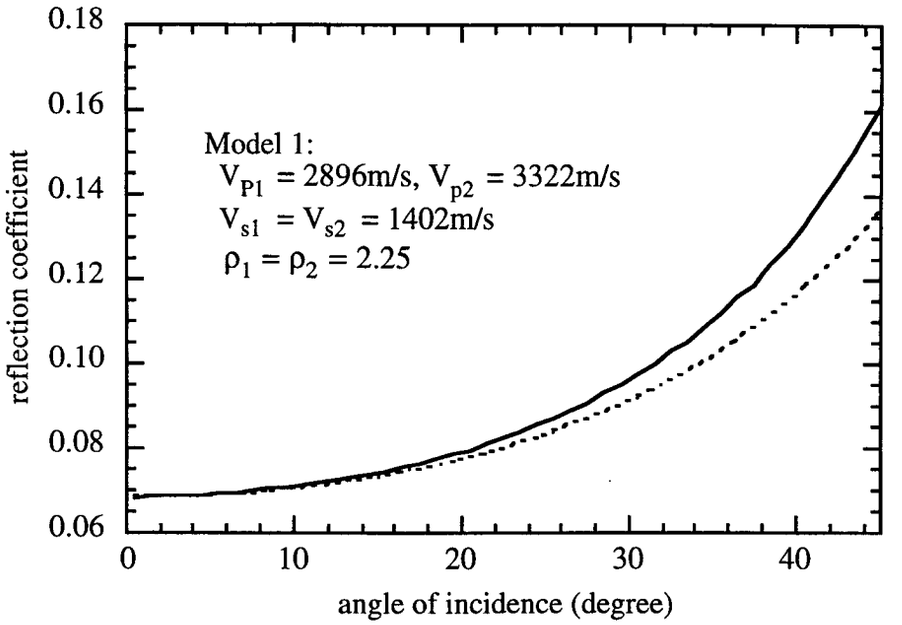

Figure 2.5: P-wave reflection coefficient for model 1. Both upper and lower layers are isotropic. The solid curve represents the numerical solution of the Zoeppritz equations, and the dotted curve the approximate solution using equation (2.37).

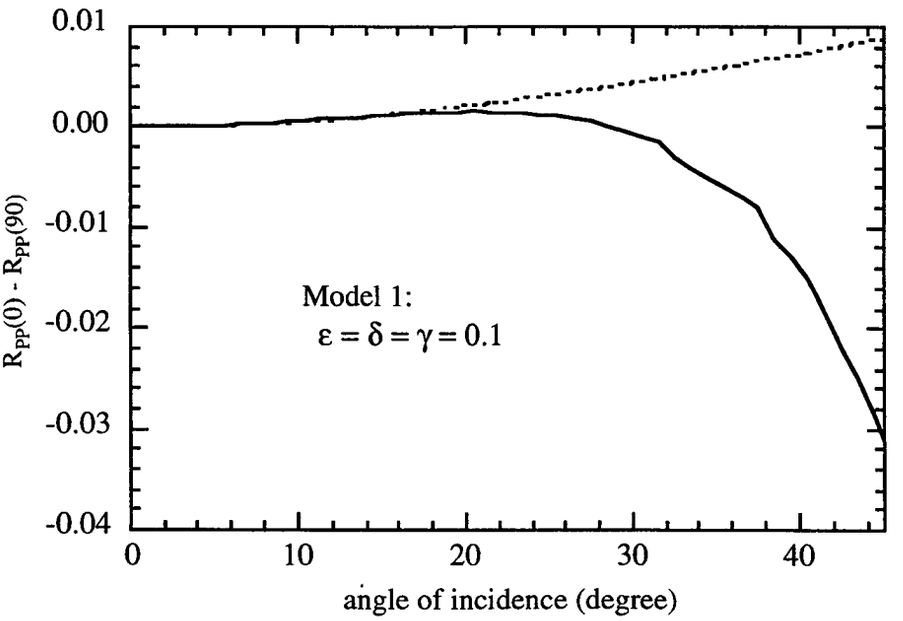

Figure 2.6: Difference between the reflection coefficient along 0-degree azimuth and that along 90-degree azimuth for model 1. The parameters used in equation (2.37) are $\varepsilon_{x2} = -0.0833$, $\delta_{x2} = -0.0833$.

Figures 2.7 show the azimuthal variations of the anisotropy terms for another case of model 1 where

$$\varepsilon_2 = 0.1,\ \delta_2 = 0.2,\ \gamma_2 = 0.1.$$

Each figure shows the difference between the reflection coefficient along certain azimuth and that along 90-degree azimuth. The azimuth angles are 0, 15, 30, 45, 60, and 75 degrees, respectively. These figures demonstrate that the interpolation over azimuth in equation (2.37) is an excellent approximation.

Figures 2.8 shows yet another case of model 1. The Thomsen's parameters for this case are

$$\varepsilon_2 = 0.2,\ \delta_2 = \gamma_2 = 0.$$

This case illustrates the possibility of having completely different AVO trends in different directions. In the direction of 90-degree azimuth, the reflection coefficient increases as expected with offset. In the direction of 0-degree azimuth, however, the reflection coefficient actually decreases with offset. If care is not taken, AVO analysis may come to totally different results depending on the direction of seismic survey lines.

2.5.2 Model 2

Model 2 is also a shale-gas sand model used in Shuey (1985) and again in Banik (1987). The physical properties of the model are

$$\rho_1 = 2.15 g/cm^3\ \ \alpha_1 = 2307 m/s\ \ \beta_1 = 942 m/s,$$
$$\rho_2 = 1.95 g/cm^3\ \ \alpha_2 = 1951 m/s\ \ \beta_2 = 1301 m/s.$$

The Poisson's ratio of the layers are 0.4 and 0.1, respectively.

The large contrast in Poisson's ration indicates that the absolute value of reflection coefficient increases sharply with offset, which is shown in Figure 2.9. Again the dotted curve in Figure 2.9 is the estimation using the first three terms in equation (2.37). The estimation, though predicts the trend of the reflection coefficient curve reasonably well, still has room for improvement. The error at large angles of incidence is probably because of the large contrast in shear-wave velocity between the layers.

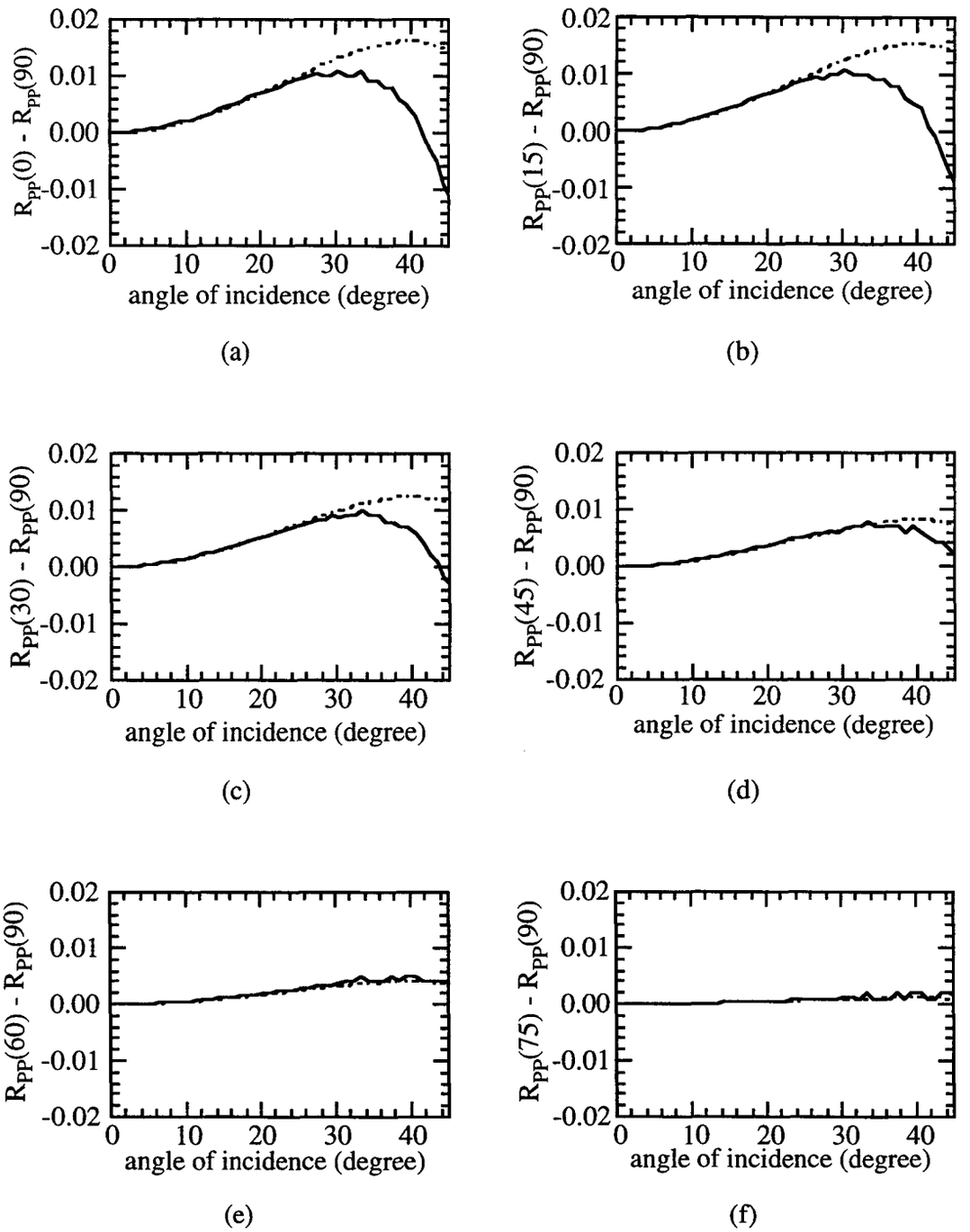

Figure 2.7: Azimuthal variations of the reflection coefficient. Each shows the difference between the AVO trend in some direction and the trend in the isotropic background. The azimuth angles are, from (a) to (f), 0, 15, 30, 45, 60, and 75 degrees, respectively.

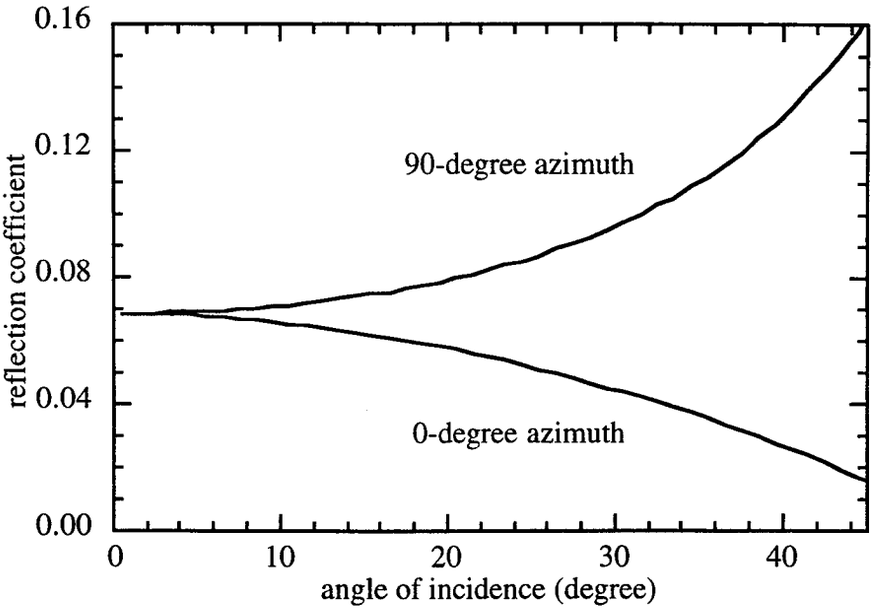

(a)

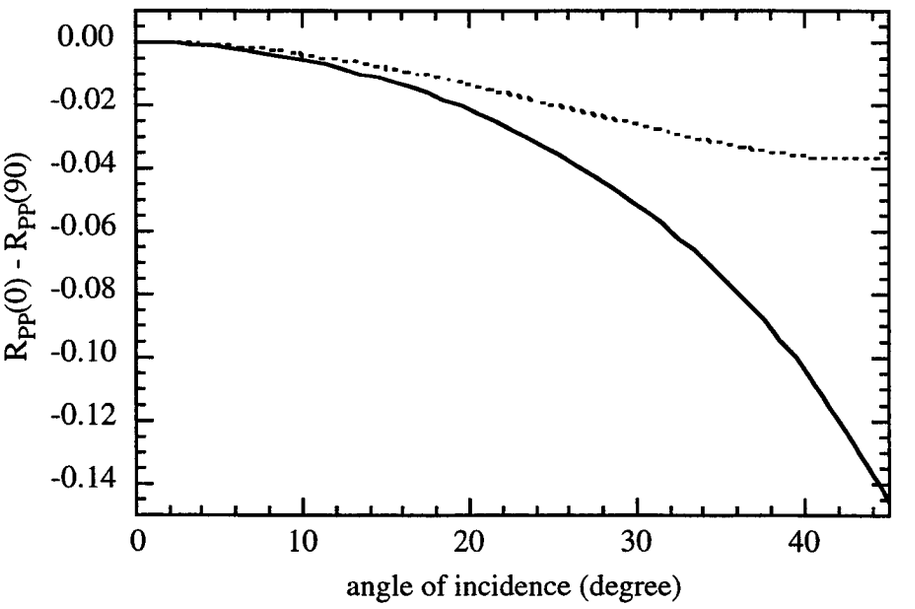

(b)

Figure 2.8: Reflection coefficient curves for a case of model 1. The Thomsen's parameters are $\varepsilon_2 = 0.2$, $\delta_2 = \gamma_2 = 0$, which translates to $\varepsilon_x = -0.14$, $\delta_x = -0.24$. (a) Reflection coefficient curves along 0 and 90-degree azimuth. (b) The contribution of anisotropy to the reflection coefficient, and the estimation using equation (2.37).

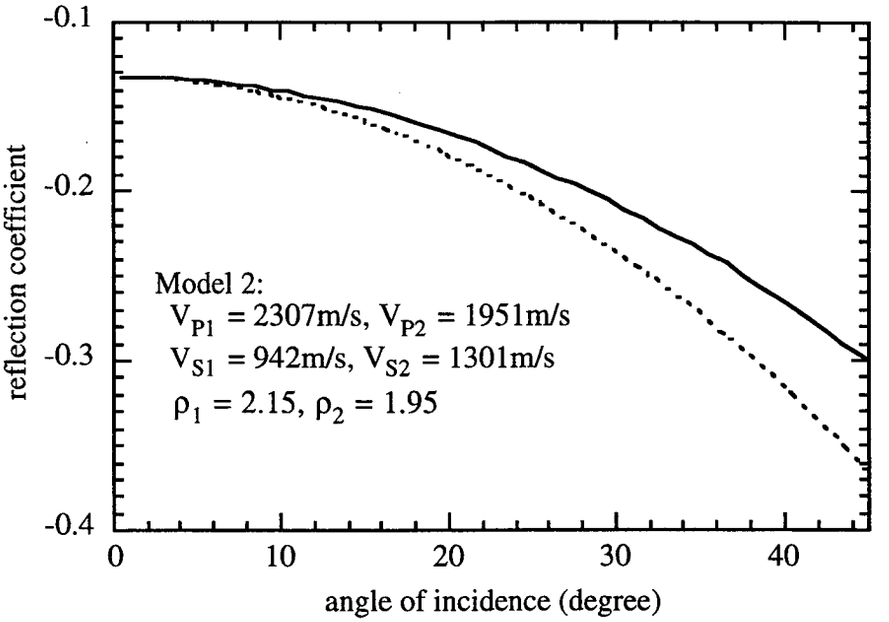

Figure 2.9: P-wave reflection coefficient for model 2. Both upper and lower layers are isotropic.

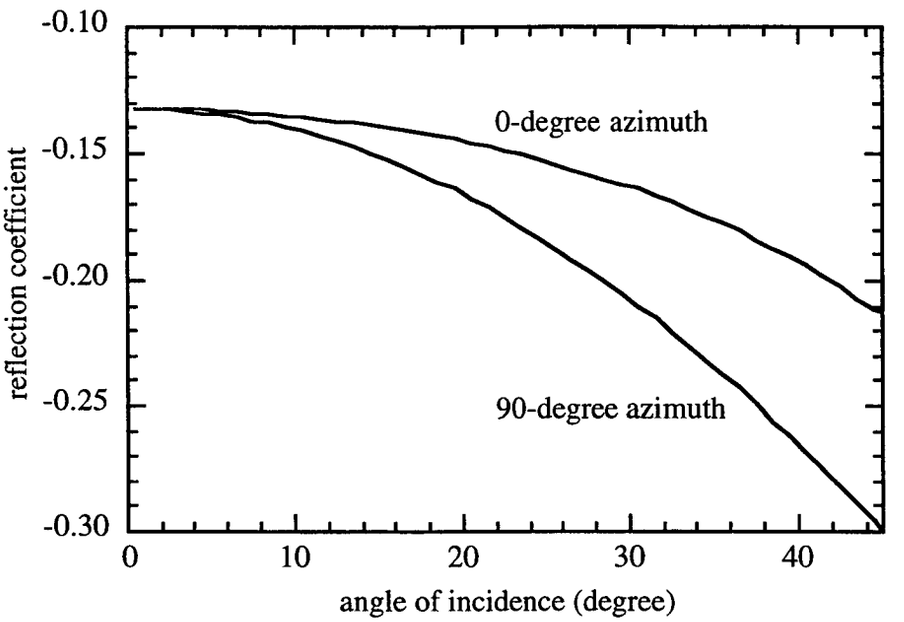

Figure 2.10: Reflection coefficient curves for a case of model 2. The Thomsen's parameters are $\varepsilon_2 = 0.05$, $\delta_2 = 0.3$, and $\gamma_2 = 0.2$.

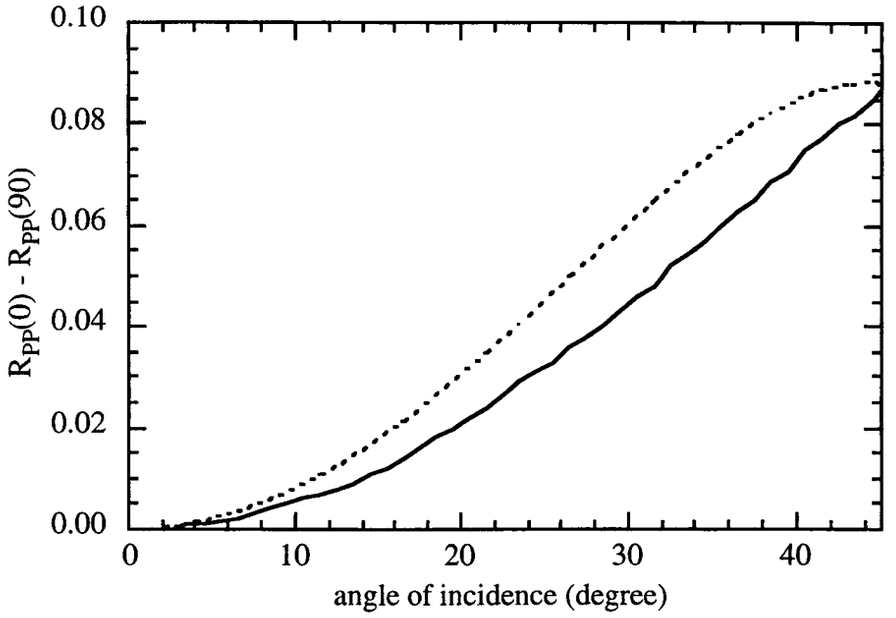

Figure 2.11: The magnitude of azimuthal AVO variations for a case of model 2. The parameters are the same as those in Figure 2.10.

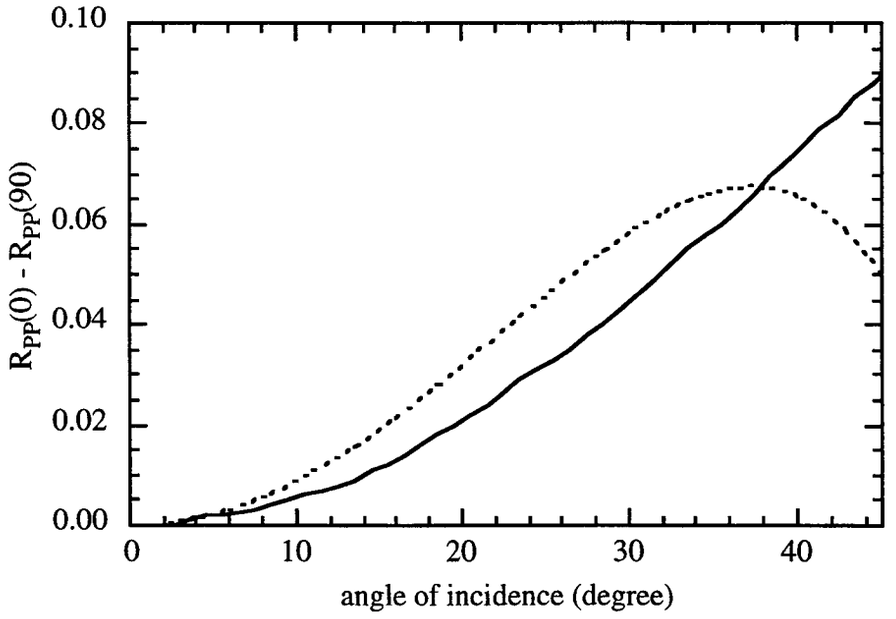

Figure 2.12: The magnitude of azimuthal AVO variations for another case of model 2. The parameters are $\varepsilon_2 = 0.0$, $\delta_2 = 0.4$, and $\gamma_2 = 0.1$.

Figures 2.10 and 2.11 show a TIH case within the background of model 2. The values of ε, δ, and γ are 0.05, 0.3 and 0.2, respectively. Figure 2.10 shows the AVO trend along 0 and 90-degree azimuth. Just like in Figure 2.8 (a), the effect of azimuthal anisotropy is striking — along 90-degree azimuth the magnitude of the reflected P-wave increases three times as fast as in 0-degree azimuth. Figure 2.11 shows numerical result and the estimation of the magnitude of the azimuthal variation of AVO trends in the case. The fit between the curves is acceptable.

Figure 12 presents another case of model 2 with ε, δ, and γ being 0, 0.4, and 0.1, respectively. The figure plots the azimuthal variations of AVO trends.

For the two cases of model 2 the quantity $\gamma - \varepsilon + (\delta/2)$ remains constant. Just as predicted in sections 3 and 4, the azimuthal anisotropic parts of the reflection coefficient curves for these two cases are very similar. The implication of this observation is that azimuthal AVO analysis alone is unlikely to fully resolve the anisotropy parameters. Instead, we can only expect an estimation of $\gamma - \varepsilon + (\delta/2)$.

2.6 Discussion

As shown by numerous cases of shear-wave splitting observed during VSP and multi-component surface seismic surveys, azimuthal anisotropy is a common condition in the earth crust. However, isotropy has almost always been the default assumption when doing AVO analysis, and the effects of azimuthal anisotropy have largely been ignored during seismic explorations. I have demonstrated that AVO anomalies caused by azimuthal anisotropy can be significant compared to those by the discontinuity of other physical properties. For example, an AVO anomaly may come from the contrast of anisotropy parameters ε, δ, and γ of the two layers, rather than Poisson's ratio. Therefore we should consider the azimuthal variation of P-wave reflection coefficients whenever possible when performing conventional AVO analysis.

2.6.1 How important is azimuthal anisotropy?

The first question is how important is azimuthal anisotropy? From the discussion in the previous sections, the answer is positive.

Qualitatively speaking azimuthal anisotropy is very important. Figures 2.8 (a) and 2.10 show huge azimuthal variations of AVO trends under reasonable anisotropy parameters. The reflection amplitude from a gas-water contact may increase with offset when the data is collected in one direction as predicted by Ostrander (1982, 1984), or it may be quite flat or even decrease with offset in another direction. Thus it is possible to miss or falsely identify

natural gas zones because of azimuthal anisotropy. To improve the accuracy of AVO analyses we must generalize our model to include azimuthal anisotropy.

Quantitatively we can also show that azimuthal anisotropy is very important. The AVO anomaly attributed to the difference of Poisson's ration of the two layers is quadratic of the sine of angles of incidence ($sin^2\theta$). Given 0.2 as an example of large contrasts in Poisson's ratio, the coefficient in front of $sin^2\theta$ is roughly 0.45 (Hilterman, 1989). The effect of azimuthal anisotropy, on the other hand, is also proportional to $sin^2\theta$ ($[\Delta\gamma - \Delta\varepsilon + (\Delta\delta/2)]sin^2\theta$). The magnitude of Thomsen's parameters, ε, δ, and γ, under the common condition of weak anisotropy, can achieve 0.1 and more. When the signs are favorable, the anisotropy effect may match $0.45sin^2\theta$, the high-end estimation of the gas effect.

2.6.2 Can we resolve anisotropy parameters from azimuthal AVO?

The magnitude of the azimuthal variation of AVO trends is proportional to the difference of $\gamma - \varepsilon + (\delta/2)$ between the two layers. Figures 11 and 12 show that given similar $\Delta\gamma - \Delta\varepsilon + (\Delta\delta/2)$, the azimuthal AVO variations are almost identical. Hence it is very difficult to resolve ε, δ, or γ individually from azimuthal AVO alone. However, large azimuthal AVO variations always indicate strong azimuthal anisotropy, and therefore are reasons for careful analysis.

Since the reflection coefficient depends on the contrast in physical properties, it is also difficult to tell definitively whether the top or the bottom layer is anisotropic without other information. The situation is worse when both layers have similar anisotropy parameters, resulting in no azimuthal variations of AVO trends at all.

2.6.3 Can we detect natural fractures from azimuthal AVO?

The multi-component shear-wave method currently used for such a purpose in essence measures γ only. The travel time difference between the fast and slow shear-waves is the accumulative effect of γ, and the amplitude difference depends on $\Delta\gamma$ at the interface. The method is well developed and has been proven in real production. However, it is far from ideal in many aspects: (1) The cost of collecting shear-wave data is often several times that of P-wave data, and the data quality is much poorer than its P-wave counterpart; (2) In terms of data availability, most of the existing data are P-wave data, whereas shear-wave data must be specially collected; (3) The processing of shear-wave data is more time-consuming and costly; (4) The effects of weathered shallow layers are difficult to estimate; (5) In some cases the symmetry axis changes with depth, and layer-stripping must be

applied; (6) Shear-wave method measures the accumulative effects, making it difficult to identify the position of the anisotropic media.

Azimuthal AVO analysis may be used to detect natural fractures in tight gas reservoirs. This method, if works, is much better. P-wave data is cheaper to collect and easier to process. Its higher signal-to-noise ratio allows detailed study of reflection amplitudes. The weathering layer almost has no effect on P-wave AVO since the reflection amplitude depends mainly on the physical properties of the two layers across the interface. No layer-stripping is necessary for the same reason. From the appearance and the lack of azimuthal AVO variations we may actually identify P-waves entering and exiting naturally fractured sedimentary layers.

Three-dimensional P-wave datasets have been collected in many areas. The rich information provided by 3-D data has not been fully exploited. Recently people have been using 3-D prestack migration more and more, further improving the accuracy and spatial resolution of amplitude estimation. The developments in the techniques of data collection and processing, together with the ever-increasing computation power, make azimuthal AVO not only feasible, but also practical.

2.6.4 Further studies and conclusion

Several problems need to be further studied. To accurately estimate the azimuthal AVO variations, the source and the receiver arrays should be as isotropic as possible. "What is the optimal source-geophone pattern" is still an open question. Current designs of source-receiver geometry do not take this requirement into consideration, and large biases may be introduced during data collection. Special data processing methods are needed to get rid of the biases and resolve azimuthal anisotropy reliably. More work has to be done to search for good algorithms.

Azimuthal AVO analysis can only give an estimation of $\Delta\gamma - \Delta\varepsilon + (\Delta\delta/2)$. It is not very clear now how to interpret the result and give a reliable fracture model. We may use Hudson's crack model or other models, but test on real data and ground truth are necessary before any conclusions can be made.

The effect of azimuthally-varying attenuation is not understood very well. How it affects the AVO analysis is a difficult question. In some cases azimuthal attenuation may not be a big factor on AVO, and in other cases the observations suggest the contrary. This problem has been ignored in this study.

Finally, let me conclude on a cautious note. The equations derived in this chapter are meant for small contrast in physical properties and weak elastic anisotropy. Numerical

modeling has shown that when used properly, the equations are good till somewhere between 30 and 40-degree angle of incidence. The error increases sharply when the angle of incidence goes beyond 35 degrees, even when the higher order terms are included. We should keep these in mind when using this chapter's results.

Acknowledgment

This work was supported by Stanford Rock Physics Project (SRB), Department of Energy contract DE-AC21-91MC28087-M004, and Gas Research Institute contract 5094-210-3235.

References

Aki, K., and Richards, P. G., 1980, Quantitative seismology, theory and methods, vol. 1: W. H. Freeman and Company.

Alkhalifah, T., and Larner, K., Migration error in transversely isotropic media: Geophys., **59**, 1405-1418.

Allen, J. L., and Peddy, C. P., 1993, Amplitude variation with offset: Gulf Coast Case Studies: Geophysical Developments Series, Volume **4**, Soc. Expl. Geophys.

Auld, B. A., 1973, Acoustic fields and waves in solids, vol 1: John Wiley and Sons.

Banik, N. C., 1984, Velocity anisotropy of shales and depth estimation in the North Sea Basin: Geophys., **49**, 1411-1419.

Banik, N. C., 1987, An effective anisotropy parameter in transversely isotropic media: Geophysics, **52**, 1654-1664.

Berryman, J. G., 1979, Long-wave elastic anisotropy in transversely isotropic media: Geophys., **44**, 896-917.

Bhagavantam, S., Crustal symmetries and physical properties: Academic Press, 1966.

Blangy, J. P., 1994, AVO in transversely isotropic media — An overview: Geophys., **59**, 775-781.

Bortfeld, R., 1961, Approximation to the reflection and transmission coefficients of plane longitudinal and transverse waves: Geophys. Prosp., **9**, 485-503.

Castagna, J. P., 1993, AVO analysis — Tutorial and review, *in* Castagna, J. P. and Bacus, M., Eds., Offset-dependent reflectivity: Theory and practice of AVO analysis: Soc. Expl. Geophys., 3-36.

Castagna, J. P., and Smith, S. W., 1994, Comparison of AVO indicators: A modeling study: Geophysics, **59**, 1849-1855.

Chapman, C. H., 1976, Exact and approximate generalized ray theory in vertically inhomogeneous media: Geophys. J. R. astr. Soc., **46,** 201-233.

Crampin, S., Chesnokov, E. M., and Hipkin, R. A., 1984, Seismic anisotropy — the state of the art: Geophys. J. R. astr. Soc., **76,** 1-16.

Crampin, S., 1987, Origins of shear-wave splitting; answers, questions, and speculations: 57nd Ann. Int. Mtg., Soc. Expl. Geophys., Expanded Abstracts, 919.

Daley, P. F., and Hron, F., 1977, Reflection and transmission coefficients for transversely isotropic media: Bull. Seismic Soc. Am., **67**, 661-675.

Fatti, J. L., Smith, G. C., Vail, P. J., Strauss, P. J., and Levitt, P. R., 1994, Detection of gas in sandstone reservoirs using AVO analysis: A 3-D seismic case history using the Geostack technique: Geophys., **59**, 1362-1376.

Hilterman, F., 1989, Is AVO the seismic signature of rock properties?: 59th Ann. Int. Mtg., Soc. Expl. Geophys., Expanded Abstracts, 559.

Hudson, J. A., 1980, Overall properties of a cracked solid: Math. Proc. Camb. Phil. Soc., **88**, 371-384.

Hudson, J. A., 1981, Wave speeds and attenuation of elastic waves in material containing cracks: Geophys. J. R. Astr. Soc., **64**, 133-150.

Hudson, J. A., 1991, Crack distributions which account for a given seismic anisotropy: Geophys. J. Int., **104**, 517-521.

Levin, F. K., 1994, Reflection point behavior in transversely isotropic solids: Geophys., **59**, 309-314.

Liu, X, 1994, Nonlinear elasticity, seismic anisotropy, and petrophysical properties of reservoir rocks: Ph.D. dissertation, Stanford University, Stanford, California.

Mueller, M., 1992, Using shear waves to predict lateral variability in vertical fracture intensity: The Leading Edge, **59**, no. 2, 29-35.

Nur, A., 1971, Effects of stress on velocity anisotropy in rocks: J. Geophys. Res., **76**, 2022-2034.

Ostrander, W. J., 1982, Plane-wave reflection coefficients for gas sands at nonnormal angles of incidence: 52nd Ann. Int. Mtg., Soc. Expl. Geophys., Expanded Abstracts, 216-218.

Ostrander, W. J., 1984, Plane-wave reflection coefficients for gas sands at nonnormal angles of incidence: Geophys., **49**, 1637-1648.

Pelissier, M. A., Thomas-Betts, A., and Vestergaard, P. D., 1991, Azimuthal variations in scattering amplitudes induced by transverse isotropy: Geophys., **56**, 1584-1595.

Rutherford, S. R., and Williams, R. H., 1989, Amplitude-versus-offset variations in gas sands: Geophys., **54**, 680-688.

Schoenberg, M., and Protázio, J., 1992, 'Zoeppritz' rationalized and generalized to anisotropy: J. Seismic Expl., **1**, 125-144.

Schulz, R., Mavko, G., and Nur, A., 1994, Application of a phenomenological theory for describing the influence of the static stress field on seismic wave propagation: SRB report, **55-B**, paper J.

SEG/EAEG, 1992, How useful is amplitude-versus-offset (AVO) analysis?: Joint SEG/EAEG summer research workshop, August 9-14, 1992, Big Sky, Montana, USA, Technical Program and Abstracts.

Shuey, R. T., 1985, A simplification of the Zoeppritz equations: Geophys., **50**, 609-614.

Thomsen, L., 1986, Weak Elastic Anisotropy: Geophys., **51**, 1954-1966.

Thomsen, L., 1988, Reflection seismology over azimuthally anisotropic media: Geophys., **53**, 304-313.

Thomsen, L., 1993, Weak anisotropic reflections, *in* Castagna, J. P. and Bacus, M., Eds., Offset-dependent reflectivity: Theory and practice of AVO analysis: Soc. Expl. Geophys., 103-111.

Wright, J., 1987, The effects of transverse isotropy on reflection amplitude versus offset: Geophys., **52**, 564-567.

Yin, H., 1992, Acoustic velocity and attenuation of rocks: isotropy, intrinsic anisotropy and stress induced anisotropy: Ph.D. Dissertation, Stanford University, Stanford, California.

Chapter 3

Fracture detection using 3-D P-wave data

Abstract

In tight gas reservoirs it is critical to detect and characterize the natural fractures that control gas storage and mobility. The multi-component shear-wave method (Alford, 1986) adopted by the industry is rather expensive, which motivates us to search for other techniques.

Natural fractures can have many effects on the seismic properties of rocks, such as lower velocity, velocity anisotropy, and higher attenuation. These effects may be reflected in the characteristics of P-wave data. This chapter will show that theoretically it is possible to use these characteristics to identify fractured regions. P-wave data are cheaper to acquire and process than shear-wave data, and in many areas P-wave data are already available.

Three methods are disscussed: (1) azimuthal variations of traveltime; (2) azimuthal variations of AVO trends; and (3) frequency-related seismic attributes.

The azimuthal variations of traveltime and AVO trends are quadratic in the sine of angle of incidence. Therefore, P-wave azimuthal anisotropy can be detected only when the offset is at least comparable to the target depth. The maximum amount of P-wave traveltime variations is approximately one half of the traveltime difference between the fast and the slow shear-waves, which can be tens of milliseconds.

Azimthal traveltime analysis is useful for detecting both fluid-filled and gas-saturated fractures, whereas azimuthal AVO analysis is effective only for fluid-filled fractures. Therefore, the best fracture indicator in tight gas reservoirs is P-wave traveltime anisotropy.

3.1 Introduction

Vast amount of natural gas exists in naturally fractured, low-permeability reservoirs. In such tight gas reservoirs, the permeability of the matrix rock can be lower than one microdarcy, while regional, systematic fracture sets can easily increase the permeability by one or two orders in magnitude, sometimes more. Often times commercial production of natural gas is feasible only when the wells are drilled into naturally fractured gas-bearing formations. Therefore, it is very important to identify naturally fractured regions in tight gas reservoirs. The crucial parameters for successful drillings include the location, density, and orientation of the fractures.

Regional fractures can be observed from the outcrops. Figure 3.1 shows a typical fracture pattern in the Wasatch formation in the Piceance basin, southwestern Colorado (Lorenz et al., 1991). The primary set of sub-parallel fractures (trending left-to-right) is more regular and evenly-spaced, and the secondary set of fractures is somewhat irregular. The spacing of the primary fractures is about 1 meter. Similar fracture patterns have been found in many other places.

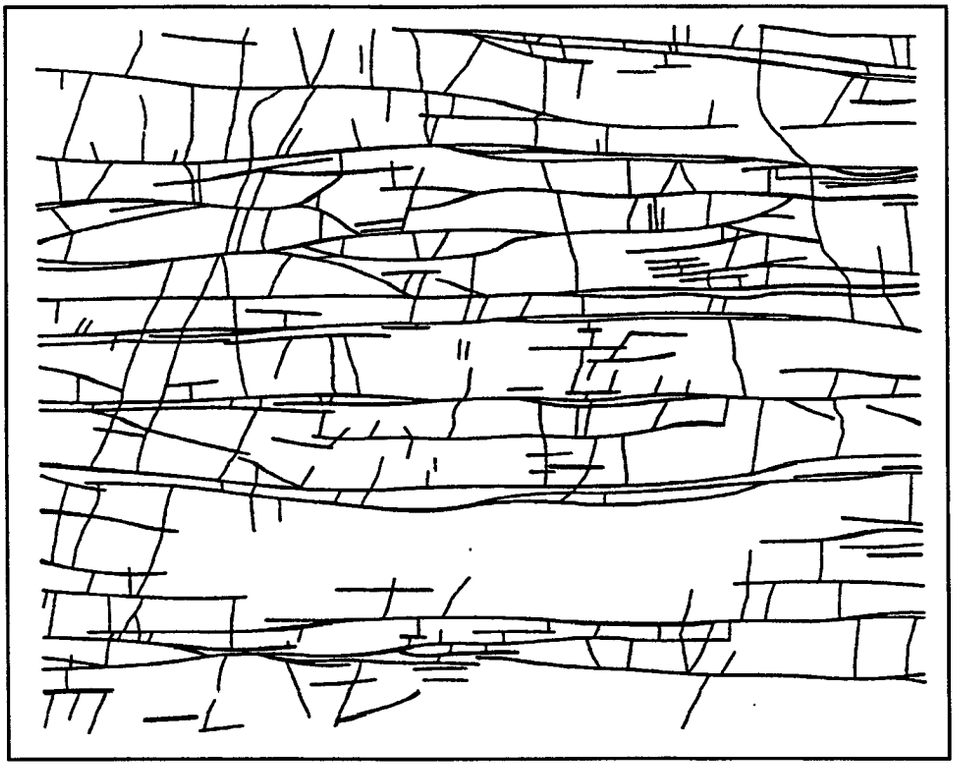

Figure 3.1: Planar view of the fracture pattern in Wasatch formation (sandstone), Piceance basin, northwestern Colorado (From Lorenz et al., 1991).

Fractures like those in Figure 3.1 would most likely introduce azimuthal anisotropy, that is, transverse isotropy with a horizontal symmetry axis, in an otherwise isotropic rock matrix (Hudson, 1980, 1981). Rock physics can predict the physical properties of the fractured rock and the behaviors of the waves traveling in the rock. For example, vertically-traveling shear-waves have different velocities depending on the polarization, and the shear-wave polarized inside the fracture plane has a higher velocity than that polarized perpendicular to the fracture plane.

The multi-component shear-wave method (Alford, 1986) currently adopted by the oil industry exploits this phenomenon. Alford (1986) designed an algorithm to analyze the orientation of the symmetry axis based on the four components of shear-wave data. The fracture density can be estimated by examining the velocity difference, the traveltime, and the relative reflection coefficients of the fast and slow shear-waves (Mueller, 1992).

In essence, the multi-component shear-wave method measures γ, the Thomsen's parameter for shear anisotropy. The travel time difference between the fast and slow shear-waves is the accumulative effect of γ, and the amplitude difference depends on $\Delta\gamma$ at the interface.

There are several disadvantages of shear-wave methods relative to P-wave methods:

- *High cost of data collection*: A shear-wave survey uses twice as many shots and channels as a similar P-wave survey. Furthermore, since shear-waves travel much slower than P-waves, far longer recording time is required to target the same reflector, resulting in a four to eight-fold increase in data volume.
- *High cost of data processing*: Shear-wave data suffer heavily from ground roll and other noise. Special time-consuming algorithms must be used to improve the signal-to-noise ratio.
- *Shallow layer problem*: The statics problem is much more serious because of longer traveltimes. Sometimes the shallow layers even contribute a large portion to the observed anisotropy. The effects are difficult to estimate.
- *Data availablity*: Most land and almost all marine data are P-wave, whereas shear-wave data must be specially collected.

In this chapter I discuss possible ways to detect natural fractures using *P-wave* data.

Theoretical and laboratory results suggest that fractures can have many effects on the seismic properties of rocks, such as lower velocity, velocity anisotropy, and higher attenuation. These changes in the physical properties of rocks may be reflected in the characteristics of P-wave data. For example, we may observe velocity anisotropy through azimuthal variations of traveltime or amplitude-versus-offset (AVO) trends. We may also

identify regions with high attenuation by examining the frequency content of the seismic traces.

Three-dimensional P-wave datasets have been routinely collected in many areas. The rich information provided by 3-D data has not been fully exploited. Recently people have been using 3-D prestack migration more and more, further improving the spatial resolution and the accuracy of amplitude estimation. The developments in the techniques of data collection and processing, together with the ever-increasing computation power, make azimuthal AVO and velocity analysis not only feasible, but also practical.

The P-wave method, if it works, would be very valuable. At the very least, it can be used to identify possible fractured zones for later detailed study using the more expensive shear-wave method.

The rest of this chapter is divided into four sections. Section 2 studies how to detect fractures from the azimuthal variations of velocity and traveltime. Section 3 discusses azimuthal AVO trends resulted from fractured rocks. Section 4 briefly explores the possibility of using the frequency content of seismic traces to detect regions with high attenuation. Section 5 concludes the chapter.

3.2 Azimuthal variations of velocity and traveltime

Of all the measurable attributes of surface seismic data, traveltime is probably the most reliable. For a long time, it was the sole purpose of seismic exploration to obtain images of underground structures from traveltime information. Even recently, with the increasing popularity of amplitude-versus-offset (AVO) analysis and other techniques, velocity analysis from traveltime in common-midpoint (CMP) gathers is still the most fundamental technique of seismic data processing.

It is well-known that preferentially oriented cracks or fractures can introduce anisotropy in an otherwise isotropic rock (Nur, 1971; Hudson, 1980, 1981). To detect natural fractures using conventional P-wave data instead of multi-component shear-wave data, the first thing to consider is the azimuthal variations of P-wave traveltime caused by velocity anisotropy.

For simplicity let us consider a rock containing parallel cracks. Conceptually the rock is softer in the direction normal to the crack plane than in other directions, and the P-wave velocity is lower. The orientation-dependent variation of velocity will translate to azimuthal variation of traveltime for the same source-geophone distance in a 3-D seismic survey. If the azimuthal traveltime variation is large enough, we should be able to use it to detect velocity anisotropy, and therefore identify underground fractures.

It is not surprising that up to now people have rarely used the azimuthal variations of P-wave velocity or traveltime to detect natural fractures. Only in recent years have 3-D seismic surveys been used routinely in oil and gas exploration, and the main purpose of most 3-D surveys is still limited to imaging structures. The anisotropy effects of fractures, on the other hand, are very weak and may be easily missed. Furthermore, most of the 3-D surveys are not designed and the data not processed with anisotropy in mind, which makes identifying anisotropy even more difficult.

There are several issues that need to be addressed. The first is how much traveltime variation we can expect in an azimuthally anisotropic environment. The second is how many fractures does it take to create a detectable anisotropy. Beyond these there are practical issues such as designing source and geophone arrays, finding optimal and automated ways to process the data, and estimating fracture densities and orientations from anisotropy.

In this section I will give simple formulas to measure the amount of anisotropy based on azimuthal traveltime variations. It is more difficult to estimate fracture parameters, which depend heavily on the fracture models. I will use Hudson's crack model (Hudson, 1980, 1981) to illustrate some basic points. The practical issues are better left to the geophysicists conducting real surveys.

3.2.1 Traveltime equation

The basic traveltime equation as a function of offset in isotropic media is well-known. Figure 3.2 shows the simplest case of a single horizontal layer. The relationship between traveltime t and offset x is (Yilmaz, 1987)

$$t^2(x) = t^2(0) + \frac{x^2}{\mathrm{v}^2}, \tag{3.1}$$

where $t(0)$ is the vertical two-way traveltime, and v is the P-wave velocity of the isotropic medium.

In an azimuthally anisotropic environment, the velocity depends not only on the angle of incidence θ, but also on the azimuth ϕ of the line connecting the source and the receiver. If the medium is transversely isotropic with a horizontal symmetry axis in the x-direction, the magnitude of the group velocity V of the P-wave is (Sena, 1991)

$$\mathrm{V}^{-2}(\theta, \phi) = a_0 + a_1 \sin^2\theta + a_2 \sin^4\theta. \tag{3.2}$$

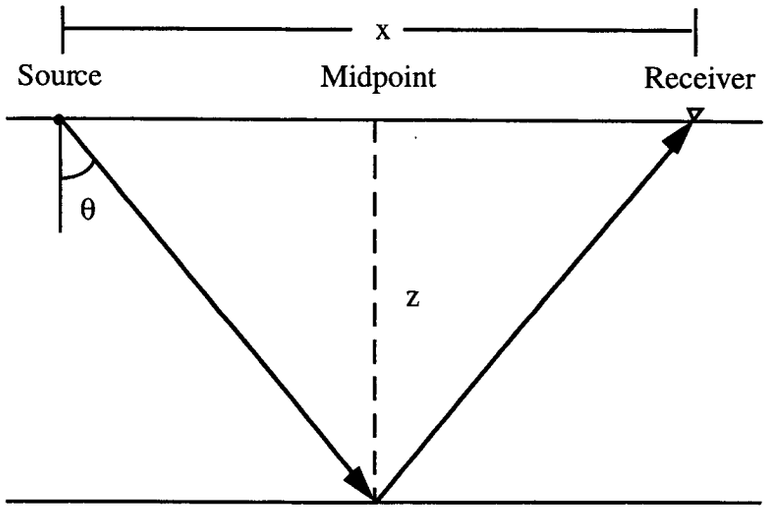

Figure 3.2: Source-receiver geometry of a single horizontal reflector.

The coefficients a_0, a_1, and a_2 are defined as folllows:

$$\begin{aligned} a_0 &= \alpha^{-2}(1-2\varepsilon), \\ a_1 &= 2\alpha^{-2}(2\varepsilon-\delta)\cos^2\phi, \\ a_2 &= 2\alpha^{-2}(\delta-\varepsilon)\cos^4\phi, \end{aligned} \tag{3.3}$$

where α is the P-wave velocity in the direction of the symmetry axis, and ε and δ the Thomsen's parameters of transverse isotropy defined in the intrinsic coordinate system of the medium (Thomsen, 1986).

Combining equations (3.1) and (3.2), we can write the traveltime equation as follows: (Sena, 1991)

$$t^2(x,z,\phi) = \left(\frac{2z}{\mathrm{V}_v}\right)^2 + \left[\left(\frac{z}{\mathrm{V}_\gamma}\right)^2 + \left(\frac{x}{2\mathrm{V}_h}\right)^2\right]\frac{x^2}{z^2+(x/2)^2}, \tag{3.4}$$

where V_v, V_γ, and V_h are called the vertical velocity, the skew moveout velocity, and the horizontal moveout velocity, respectively (Sena, 1991). Written in terms of a_0, a_1, and a_2 as shown in equations (3.3), these velocities are

$$\begin{aligned} \mathrm{V}_v &= a_0^{-1/2}, \\ \mathrm{V}_\gamma &= (a_0+a_1)^{-1/2}, \\ \mathrm{V}_h &= (a_0+a_1+a_2)^{-1/2}. \end{aligned} \tag{3.5}$$

Notice that coefficients a_1 and a_2 are azimuth-dependent.

3.2.2 Azimuthal traveltime variations

Written explicitly in terms of coefficients a_0, a_1, and a_2, the traveltime equation (3.4) becomes

$$t^2(x,z,\phi) = (x^2 + 4z^2)a_0 + x^2 a_1 + x^2 a_2 \sin^2\theta. \tag{3.6}$$

The first term on the right-hand side of equation (3.6) is azimuth-independent, and the second and third terms are azimuth-dependent. When the azimuth is an odd multiple of $\pi/2$, the azimuth-dependent part vanishes. Thus the traveltime variation, the azimuth-dependent part of equation (3.6), can be written as

$$t^2(x,z,\phi) - t^2\left(x,z,\frac{\pi}{2}\right) = x^2 a_1 + x^2 a_2 \sin^2\theta. \tag{3.7}$$

Now with the necessary tools ready, I can compute the azimuthal variations of the P-wave traveltime as a fraction of the total two-wave traveltime, as follows:

$$\begin{aligned}
\frac{\Delta t}{t} &\equiv \frac{t(x,z,\phi) - t(x,z,\pi/2)}{t(x,z,\pi/2)} \\
&\approx \frac{x^2 a_1 + x^2 a_2 \sin^2\theta}{2(x^2 + 4z^2)a_0} \\
&= (2\varepsilon - \delta)\cos^2\phi \sin^2\theta + (\delta - \varepsilon)\cos^4\phi \sin^4\theta \\
&\approx (2\varepsilon - \delta)\cos^2\phi \sin^2\theta.
\end{aligned} \tag{3.8}$$

The second term on the right hand side of equation (3.8) is omitted in the last step because, as shown later in this section, the magnitude of $\delta - \varepsilon$ is less than or comparable to that of $2\varepsilon - \delta$. Even when the angle of incidence is as large as 30 degrees, the magnitude of the second term is only about a quarter of that of the remaining term.

A few observations can be made from equation (3.8):

- The azimuthal variation of traveltime is quadratic in the sine of angles of incidence. Therefore, traveltime variations can be detected only when the seismic data contains traces with large angles of incidence. As a rule of thumb, the largest offset of the seismic traces should be comparable to the depth of the targeted reflector.
- The azimuthal variation of traveltime is linear in Thomsen's anisotropy parameters ε and δ. For reasonably large offsets that are comparable to the depth of the target, the azimuthal variation of traveltime $\Delta t/t$ can amount to a few percent even in weakly anisotropic environments. For one second of two-way traveltime, a few percent translates into tens of milliseconds, a significant amount easily observable.

- The azimuthal variation of traveltime is quadratic in the cosine of azimuth. Given an azimuth-binned 3-D CMP gather, we can fit the traveltime surface using statistical methods to increase the reliability of data processing.

3.2.3 Fracture models

The multi-component shear-wave methods estimate shear-wave anisotropy (γ), while 3-D P-wave methods measure mostly P-wave anisotropy ($2\varepsilon - \delta$). Even though qualitatively we can say that larger ($2\varepsilon - \delta$) indicates higher fracture densities, sometimes we may want to quantify the fracture parameters.

Any quantitative description of fractures depends on the fracture models. The most widely used is Hudson's crack model (Hudson, 1980, 1981, 1990). According to Hudson (1981), when a rock contains one set of parallel cracks aligned in the x_3-direction, the first-order correction of the rock's stiffness matrix is

$$\mathbf{c}^1 = -\frac{va^3}{\mu}\begin{bmatrix} \lambda^2U_3 & \lambda^2U_3 & \lambda(\lambda+2\mu)U_3 & 0 & 0 & 0 \\ \lambda^2U_3 & \lambda^2U_3 & \lambda(\lambda+2\mu)U_3 & 0 & 0 & 0 \\ \lambda(\lambda+2\mu)U_3 & \lambda(\lambda+2\mu)U_3 & (\lambda+2\mu)^2U_3 & 0 & 0 & 0 \\ 0 & 0 & 0 & 2\mu^2U_1 & 0 & 0 \\ 0 & 0 & 0 & 0 & 2\mu^2U_1 & 0 \\ 0 & 0 & 0 & 0 & 0 & 0 \end{bmatrix}, \tag{3.9}$$

where a is the mean radius of the cracks, v the number density of the cracks, and λ and μ the Lamé moduli of the solid uncracked rock. U_1 and U_3 are non-dimensional quantities depending on the internal condition of the cracks and Poisson's ratio of the uncracked material. Hudson's model assumes dilute concentration of the cracks, which means that va^3 is much less than unity.

In Hudson's model, the Thomsen's parameters of the anisotropy induced by the cracks are

$$\begin{aligned} \varepsilon = \frac{c_{11}-c_{33}}{2c_{33}} &= \frac{\left(\lambda+2\mu-\frac{va^3}{\mu}\lambda^2U_3\right)-\left[\lambda+2\mu-\frac{va^3}{\mu}(\lambda+2\mu)^2U_3\right]}{2\left[\lambda+2\mu-\frac{va^3}{\mu}(\lambda+2\mu)^2U_3\right]} \\ &\approx \frac{va^3}{\mu}\frac{4\lambda\mu+4\mu^2}{2(\lambda+2\mu)}U_3 \\ &= \frac{2va^3(\lambda+\mu)U_3}{\lambda+2\mu}, \end{aligned} \tag{3.10}$$

$$\begin{aligned}\delta &= \frac{(c_{13}+c_{44})^2-(c_{33}-c_{44})^2}{2c_{33}(c_{33}-c_{44})} = \frac{(c_{13}+c_{33})(c_{13}-c_{33}+2c_{44})}{2c_{33}(c_{33}-c_{44})} \\ &\approx \frac{(c_{13}^0+c_{33}^0)(c_{13}^1-c_{33}^1+2c_{44}^1)}{2c_{33}^0(c_{33}^0-c_{44}^0)} \\ &= \frac{[\lambda+\lambda+2\mu]\left[-\frac{va^3}{\mu}\lambda(\lambda+2\mu)U_3+\frac{va^3}{\mu}(\lambda+2\mu)^2U_3-4va^3\mu U_1\right]}{2(\lambda+2\mu)(\lambda+\mu)} \\ &= 2va^3\left(U_3-\frac{2\mu}{\lambda+2\mu}U_1\right),\end{aligned} \tag{3.11}$$

and

$$\gamma = \frac{c_{66}-c_{44}}{2c_{44}} = \frac{\mu-(\mu-2va^3\mu U_1)}{2(\mu-2va^3\mu U_1)} \approx va^3U_1. \tag{3.12}$$

With the anisotropy parameters, we can compute the coefficient of the azimuthal variations of traveltime, as follows:

$$2\varepsilon-\delta = 2va^3\left(\frac{2\mu}{\lambda+2\mu}U_1+\frac{\lambda}{\lambda+2\mu}U_3\right). \tag{3.13}$$

Hudson (1981) computed the values of U_1 and U_3 for several special cases. We can use his results to further simplify equation (3.13).

1) Fluid-filled cracks

In the model of a fluid-filled crack, there is no shear traction on the crack, and the displacement discontinuity may exist only in the transverse direction. The quantities U_1 and U_3 are (Hudson, 1981)

$$\begin{aligned}U_1 &= \frac{16}{3}\frac{\lambda+2\mu}{3\lambda+4\mu}, \\ U_3 &= 0.\end{aligned} \tag{3.14}$$

Hence

$$2\varepsilon-\delta = \frac{64}{3}va^3\frac{\mu}{3\lambda+4\mu} \approx 3.0va^3. \tag{3.15}$$

For comparison the amount of shear-wave anisotropy is

$$\gamma = \frac{16}{3} va^3 \frac{\lambda + 2\mu}{3\lambda + 4\mu} \approx 2.3 va^3. \tag{3.16}$$

In the last step of the derivation of equations (3.15) and (3.16), λ and μ are assumed equal. The anisotropy parameters are all proportional to the fracture parameter va^3. In the discussion that follows, I will drop this term and deal with the scaled coefficients only.

Equations (3.15) and (3.16) indicate that the anisotropy parameters $2\varepsilon - \delta$ and γ, which control the amount of compressional- and shear-wave traveltime variations respectively, are comparable when Poisson's ratio is 0.25.

Figure 3.3 shows $2\varepsilon - \delta$ and γ, scaled by va^3, as functions of Poisson's ratio of the uncracked rock. For a wide range of Poisson's ratio, $2\varepsilon - \delta$ is greater than or at least comparable to γ .

2) Dry cracks

In the model of a dry crack, there is no traction on the crack surface, and the displacement discontinuity remains the same as a fluid-filled crack. U_1 is still given by equations (14), thus γ is the same as in equation (3.16). The quantity U_3 is (Hudson, 1981)

$$U_3 = \frac{4}{3} \frac{\lambda + 2\mu}{\lambda + \mu}, \tag{3.17}$$

and the coefficient of azimuthal traveltime variations is

$$2\varepsilon - \delta = 2va^3 \left(\frac{4}{3} \frac{\lambda}{\lambda + \mu} + \frac{32}{3} \frac{\mu}{3\lambda + 4\mu} \right) \approx 4.4 va^3. \tag{3.18}$$

As in equation (15), λ is assumed equal to μ in the last step of derivation.

Figure 3.4 shows $2\varepsilon - \delta$ and γ, scaled by va^3, as functions of Poisson's ratio of the uncracked rock for the case of dry cracks.

3.2.4 Discussion

1) P-wave anisotropy vs. shear-wave anisotropy

Since gas saturated rocks usually have low Poisson's ratio, from Figure 3.4 we can see that $2\varepsilon - \delta$ is approximately twice as large as γ in gas-bearing formations. However, this

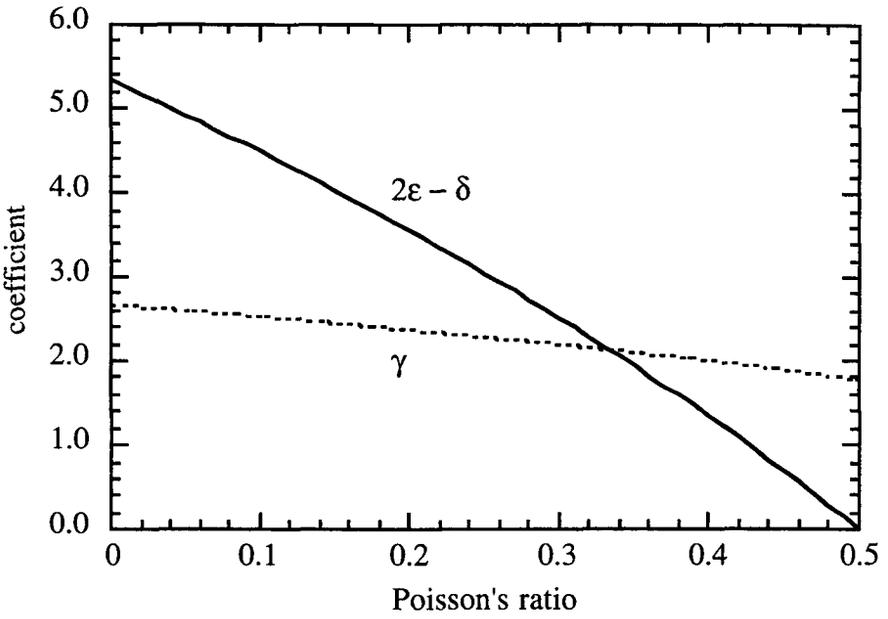

Figure 3.3: Anisotropy parameters $2\varepsilon - \delta$ and γ (scaled by va^3) of rocks with fluid-filled cracks as a function of Poisson's ratio of the uncracked rock.

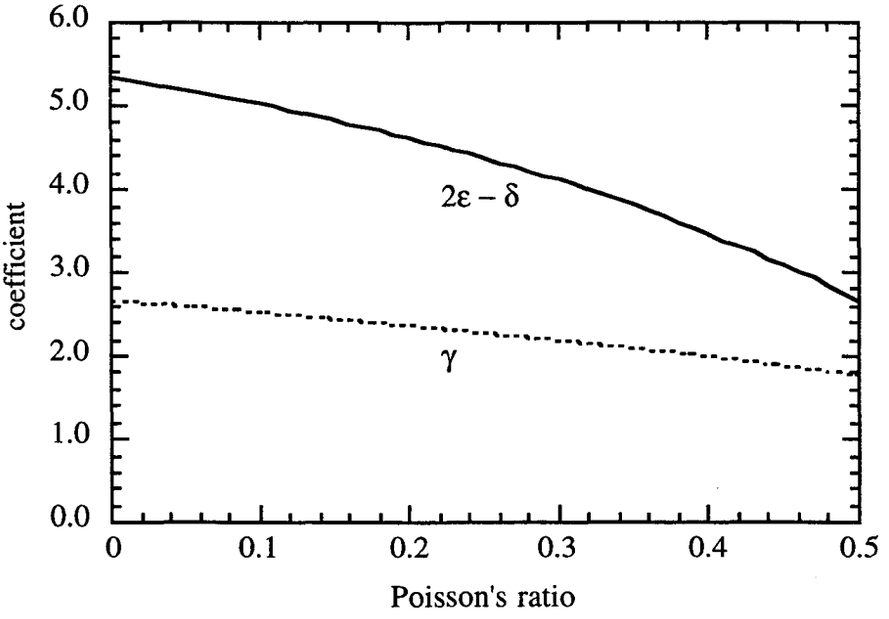

Figure 3.4: Anisotropy parameters $2\varepsilon - \delta$ and γ (scaled by va^3) of rocks with dry cracks as a function of Poisson's ratio of the uncracked rock.

is not to say that the amount of P-wave anisotropy is bigger than that of shear-wave anisotropy.

When scaled by the total traveltime, Δt_S, the traveltime difference between the vertically traveling fast and slow shear-waves, depends only on γ, while Δt_P, the azimuthal variations of P-wave traveltime, depends not only on $2\varepsilon - \delta$, but also on $sin^2\,\theta$ as well. Given 30 degrees as an example of very large angle of incidence, $\Delta t_P / t_P$ is about one half of $\Delta t_S / t_S$. Considering large traveltime differences often observed in studies of shear-wave splitting, we can certainly expect to see a significant amount of azimuthal variations of P-wave traveltime in azimuthally anisotropic environments.

Recently Lynn et al. (1995) published an observed case of azimuthal P-wave traveltime in a fractured gas field in the Wind River Basin in central Wyoming. The depth of the target is from 5,000 to 10,000 feet, and the geophone offset is from 50 to 10,000 feet. The maximum amount of the traveltime variation is about 50 milliseconds, compared to a two-wave P-wave traveltime of 2 seconds.

2) The sign of $(2\varepsilon - \delta)$

When the angle of incidence remains unchanged, a P-wave traveling parallel to the fracture plane is faster than P-waves in other azimuths. Thus the quantity $(2\varepsilon - \delta)$ should always be positive. Note that this is true for the cases of both fluid-filled and dry cracks. Equations (3.13), (3.15) and (3.17) confirm our intuition.

3) $(2\varepsilon - \delta)$ vs. $(\delta - \varepsilon)$

In the derivation of equation (3.8) the term with $(\delta - \varepsilon)$ is omitted. To justify the omission we use equations (3.10), (3.11), (3.14), and (3.17) and write

$$\delta - \varepsilon = \begin{cases} -\dfrac{64}{3}\dfrac{\mu}{3\lambda + 4\mu} v a^3, & \text{fluid - filled} \\ \left(\dfrac{8}{3}\dfrac{\mu}{\lambda + \mu} - \dfrac{64}{3}\dfrac{\mu}{3\lambda + 4\mu}\right) v a^3. & \text{dry} \end{cases} \tag{3.19}$$

Figure 3.5 shows $(\delta - \varepsilon)$, scaled by va^3, as functions of Poisson's ratio of the uncracked rock. Comparing with Figures 3.3 and 3.4, the magnitude of $(\delta - \varepsilon)$ is indeed no greater than that of $(2\varepsilon - \delta)$.

4) Multilayered Media

The traveltime equation for multilayered media is much more complicated (Sena, 1991). The traveltime depends on the velocities V_v, V_γ, and V_h of each layer, parameters that are very difficult to determine without other information. To deal with this problem, I propose that we get a rough estimation of anisotropy by scaling the traveltime variation by the ratio of the estimated time spent in the fractured layers and the total traveltime.

5) Azimuthal stacking velocities

In seismic data processing, we often compute the normal moveout (NMO) of a CMP gather with the highest possible stacking velocity, and correct the entire CMP gather with the same velocity. When the environment is azimuthally anisotropic, the stacking velocity may be good only for the traces with azimuth close to $\pi/2$ or $3\pi/2$. All other traces would be undercorrected by the amount determined by equation (8). Hence even for structure imaging, using a single stacking velocity for an entire CMP gather may not give the best stacking result. A few tens of milliseconds of NMO undercorrection may be large enough to reduce rather than enhance the useful signals. In conclusion, in an azimuthally

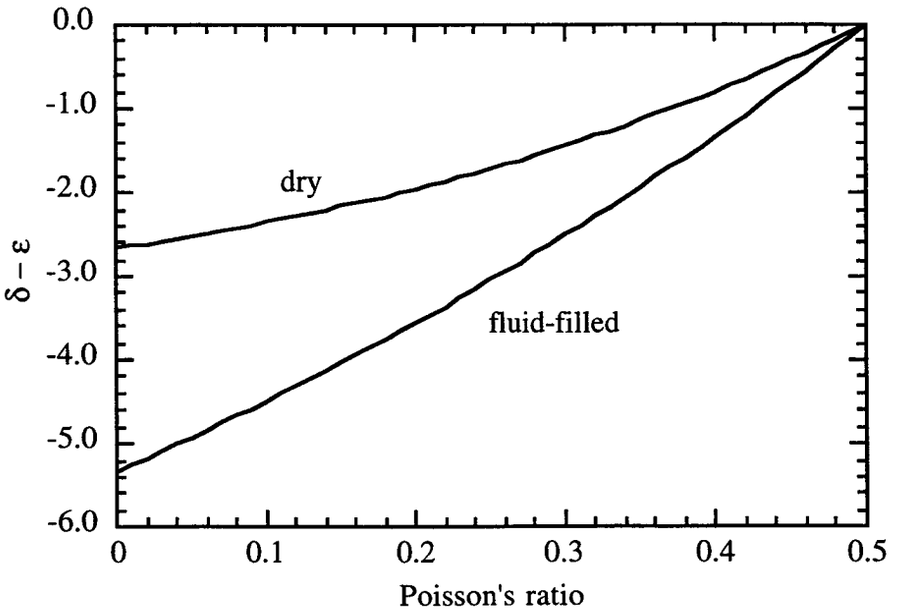

Figure 3.5: Anisotropy parameters $\delta - \varepsilon$ (scaled by va^3) of rocks with fluid-filled or dry cracks as a function of Poisson's ratio of the uncracked rock.

anisotropic environment, we should sort the data into azimuth-binned CMP gathers and stack them using azimuthally-varying stacking velocities. Fortunately, with increasingly powerful computers, it is not very expensive to do so.

6) Conclusion

Comparing Figures (3.4) and (3.5), we conclude that given the same fracture density and size, dry or gas-saturated cracks will have a larger effect on azimuthal traveltime variations than fluid-filled cracks. In tight gas reservoirs, the cracks are filled with gas, and we can expect significant traveltime variations when fractures are present. This conclusion certainly helps our effort to detect fractures using P-waves.

The multi-component shear-wave method detect fractures by the amount of traveltime difference between the fast and the slow shear-waves. It determines the fracture orientation from the angle used in Alford rotation. Using 3-D P-wave data, it is also possible to estimate the density and the orientation of the fractures. The amount of the azimuthal traveltime variation is an indicator of the fracture density, and the azimuth with the biggest stacking velocity gives the orientation of the fracture planes.

3.3 Fracture detection using azimuthal AVO

Azimuthal traveltime variations discussed in the previous section measure the accumulative effect of P-wave azimuthal anisotropy. When the thickness of the fractured layers is small compared to the depth of the target reflector, there will be hardly any azimuthal variations of traveltime at all. In this case, studying azimuthal variations of AVO trends can be very helpful.

Fracture-induced azimuthal anisotropy may result in azimuthally-varying AVO trends. Since the reflection coefficient depends on the physical properties of the two layers across the reflection interface, layer thickness is usually not a problem. For example, a deeply-buried thin layer with fractures may give a large azimuthal AVO variation even if there are no traveltime variations.

This section uses the results in chapter 2 and Hudson's crack model (Hudson, 1980, 1981) to study the possibility of detecting natural fractures using AVO analysis.

3.3.1 Azimuthal AVO

The effect of azimuthal anisotropy on AVO trends is studied in detail in chapter 2. To summarize briefly, the azimuthal variation of AVO trends is

$$R_{PP}(\phi,\theta)-R_{PP}(90°,\theta)\approx\left(\frac{\Delta\delta-2\Delta\varepsilon}{2}+4\kappa\Delta\gamma\right)sin^2\theta cos^2\phi, \qquad (3.20)$$

where $R_{PP}(\phi,\theta)$ is the reflection coefficient, θ the angle of incidence, ϕ the azimuth, and κ the square of the V_S-V_P ratio. And Δ refers to the difference of physical properties between the two layers across the interface.

Similar to equation (3.8), the azimuthal variations of AVO trends are quadratic in the sine of angles of incidence and the cosine of azimuth. The difference is that the coefficient depends on the contrast of anisotropy parameters across the interface. Hence the azimuthal AVO variation is mostly a localized effect at the reflection interface, rather than an accumulative one along the whole ray path. Another difference between equations (3.8) and (3.20) is that all three Thomsen's anisotropy parameters ε, δ, and γ may affect the coefficient. In other words, the anisotropy of shear-wave velocity is very important.

3.3.2 Azimuthal AVO under Hudson's model

For Hudson's model of rocks containing dilute concentration of circular cracks, the coefficient in equation (3.20) that controls the azimuthal AVO variations is

$$\frac{\Delta\delta-2\Delta\varepsilon}{2}+4\kappa\Delta\gamma\approx\Delta\left(\gamma-\frac{2\varepsilon-\delta}{2}\right)=\Delta\left[va^3\frac{\lambda}{\lambda+2\mu}(U_1-U_3)\right], \qquad (3.21)$$

where for simplicity 4κ is approximately one. The coefficient depends on the result of U_1-U_3, which at first sight can be either positive or negative. I will show below that Hudson's model only allows it to be positive.

Using equations (3.14) and (3.16), we can write the coefficient of azimuthal AVO vraiations for rocks containing fluid-filled or dry cracks as

$$\frac{\Delta\delta-2\Delta\varepsilon}{2}+\Delta\gamma=\Delta\left(\frac{16}{3}\frac{\lambda}{3\lambda+4\mu}va^3\right)\approx\Delta(0.76va^3), \qquad \text{(fluid-filled)} \quad (3.22)$$

and

$$\frac{\Delta\delta-2\Delta\varepsilon}{2}+\Delta\gamma=\Delta\left[va^3\left(\frac{16}{3}\frac{\lambda}{3\lambda+4\mu}-\frac{4}{3}\frac{\lambda}{\lambda+\mu}\right)\right]\approx\Delta(0.10va^3), \text{ (dry)} \quad (3.23)$$

respectively. Again λ and μ are assumed equal in equations (3.21) and (3.22). Figure 3.5 shows the amount of $(\delta-2\varepsilon)/2+\gamma$, scaled by va^3, as a function of Poisson's ratio of the uncracked rock for the cases of fluid-filled and dry cracks.

Equations (3.22) and (3.23), and Figure 3.6 demonstrate that the effect of fluid-filled cracks on AVO trends is many times bigger than that of dry cracks. This is exactly the opposite to the effect of cracks on traveltime. Especially when the Poisson's ratio is low and the cracks are dry, there will not be any observable azimuthal variations of AVO trends. This observation suggests that azimuthal traveltime analysis, or its inverse, azimuthal stacking-velocity analysis, be the first choice when searching for natural fractures in tight gas reservoirs using 3-D P-wave data.

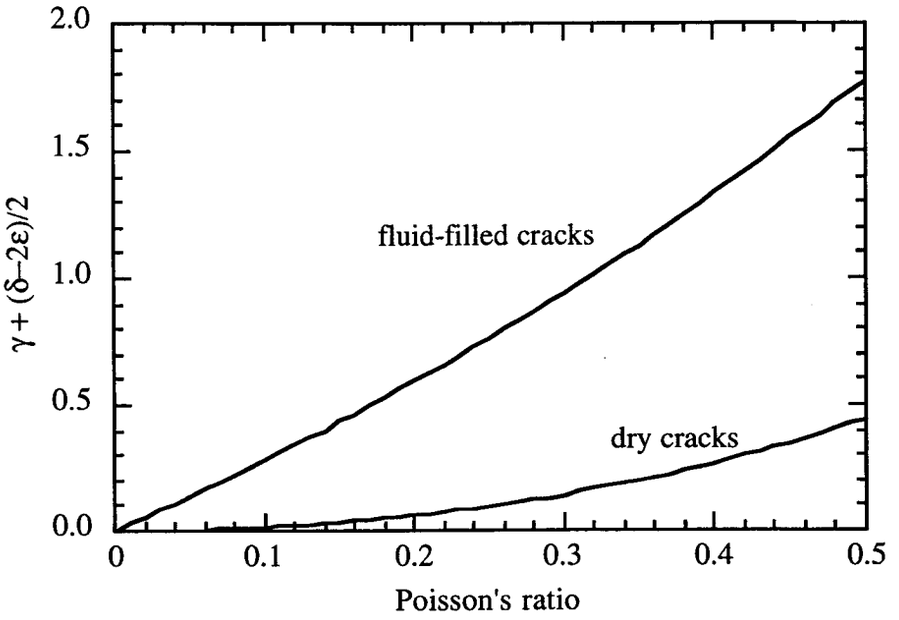

Figure 3.6: $(\delta-2\varepsilon)/2+\gamma$, scaled by va^3, as a function of Poisson's ratio of the uncracked rock for the cases of fluid-filled and dry cracks.

3.4 Fracture detection with frequency content

The P-wave techniques discussed so far rely on the observation and measurement of anisotropy. It is desirable to develop methods that study other aspects of the fracture effects. This is especially important when neither 3-D P-wave data nor shear-wave data are available.

Frequency related P-wave seismic attributes are possible candidates. They qualitatively measure the attenuation effects and can be used as a (weak) indicator of fractures.

The effect of fractures on attenuation has been studied both theoretically and experimentally by many authors (Hudson, 1981, 1991; Crampin, 1978, 1984; Mavko and

Nur, 1979; Mukerji & Mavko, 1994). In general fractured rocks have higher attenuation because of the scattering effects of the cracks and the fluid-related dissipation between the crack surfaces. When waves pass through a highly fractured zone, high frequency components tend to have a greater loss than low frequency ones. The shape of the power spectrum of the seismic traces can be used as an attribute in our search for fractures by identifying high attenuation zones.

The so-called "center frequency" of the pre-stack P-wave data is an indication of relative changes in the high frequency components of the power spectrum. The algorithm for calculating the center frequency is as follows. First extract a small section of the seismic trace at a certain depth determined by the target reflector with a tapered window, then compute the power spectrum $p(f)$ of the sequence using a fast Fourier transform, and finally calculate the center frequency f_c using

$$f_c = \left[\frac{\sum_0^{f_N} f_i^n p(f_i)}{\sum_0^{f_N} p(f_i)} \right]^{\frac{1}{n}}, \tag{3.24}$$

where f_N is the Nyquist frequency and n is an arbitrary constant.

The center frequency is computed for each trace. Since the spectrum of a trace is heavily influenced by the spectrum of the source and the response of the geophone, some kind of surface-consistent correction can help us separate these effects that are not related to natural fractures.

In chapter 4, I test some of these ideas with the P-wave data from our field survey. The result is promising. The area with low center frequences coincides with the fractured region identified by shear-wave analysis.

3.5 Conclusion

Theoretically it is possible to detect natural fractures with P-wave data. Azimuthal variations of traveltime and AVO trends, and frequency-related seismic attributes are all candidates for fractures indicators. With 3-D one-component survey, we may be able to map regions of P-wave anisotropy and estimate fracture parameters.

The azimuthal variations of traveltime and AVO trends are quadratic in the sine of angle of incidence. Therefore, P-wave azimuthal anisotropy can be detected only when the offset is very large. Theory and practice show that an offset comparable to the target depth is both effective and achievable.

The maximum amount of P-wave traveltime variations is approximately one half of the traveltime difference between the fast and the slow shear-waves. Even in weakly anisotropic environments, the variations can be tens of milliseconds.

Azimthal traveltime analysis is useful for detecting both fluid-filled and gas-saturated fractures, whereas azimuthal AVO analysis is effective only for fluid-filled fractures. Therefore, the best fracture indicator in tight gas reservoirs is P-wave traveltime anisotropy.

Frequency-related P-wave attributes, though weak indicators of fractures, are easy to compute and do not require 3-D data. They can be used as pre-screen tools, or helpful hints when no other information is available.

References

Alford, R. M., 1986, Shear data in the presence of azimuthal anisotropy: Dilley, Texas, Expanded Abstracts, 56th Ann. Int. SEG Mtg., Houston, Texas, p. 476-479.

Crampin, S., 1978, Seismic wave propagation through a cracked solid: polarization as a possible dilatancy diagnostic, Geophys. J. R. Astron. Soc., 53, 467-496.

Crampin, S., 1984, Effective anisotropic elastic constants for wave propagation through cracked solids, Geophys. J. Roy. Astr. Soc., 76, 135-145.

Heloise, B. L., Bates, C. R., Simon, K. M., and Dok, R. V., The effects of azimuthal anisotropy in P-wave 3D seismic: Expanded Abstracts, 65th Ann. Int. SEG Mtg., in press.

Hudson, J. A., 1980, Overall properties of a cracked solid: Math. Proc. Camb. Phil. Soc., **88**, 371-384.

Hudson, J. A. , 1981, Wave speeds and attenuation of elastic waves in material containing cracks, Geophys. J. Roy. Astr. Soc., **64**, 133-150.

Hudson, J. A., 1990, Overall elastic properties of isotropic materials with arbitrary distribution of circular cracks, Geophys. J. Int., **102**, p. 465-469.

Hudson, J. A., 1991, Crack distributions which account for a given seismic anisotropy, Geophys. J. Int., 104, 517-521.

Lorenz, J. C., Teufel, L. W., and Warpinski, N. R., 1991, Regional fractures I: a mechanism for the formation of regional fractures at depth in flat-lying reserviors: The American Association of Petroleum Geologists Bulletin, **75**, No. 11, 1714-1737.

Mavko, G. and Nur, A., 1979, Wave attenuation in partially saturated rocks: Geophysics, 44, 161-178.

Mueller, M., 1992, Using shear waves to predict lateral variability in vertical fracture intensitiy: The leading Edge, **11**, no. 2, p. 29-35.

Mukerji, T. and Mavko, G., 1994, Pore fluid effects on seismic velocity in anisotropic rocks, in press, Geophy.

Nur, A., 1971, Effects of stress on velocity anisotropy in rocks: J. Geophys. Res., **76**, 2022-2034.

Sena, A. G., 1991, Seismic traveltime equations for azimuthally anisotropic and isotropic media: Estimation of interval elastic properties, Geophys., **56**, 2090-2101.

Thomsen, L., 1986, Weak Elastic Anisotropy: Geophys., **51**, 1954-1966.

Yilmaz, Ö., 1987, Seismic data processing,: Society of Exploration Geophysicists.

Chapter 4

Integrated seismic study of naturally fractured tight gas reservoirs

Abstract

Multi-component shear-wave seismology is at present the only established surface seismic technique to study natural fractures that are critical to production in tight gas reservoirs. This technique, however, is very specialized and suffers from high cost and low efficiency. On the other hand, theoretical studies have shown that it is possible to detect natural fractures using conventional P-wave data. The field project reported in this chapter is an attempt to study the feasibility of this idea and an opportunity for us to gain experience in the field of fracture detection.

We collected about 50 kilometers of nine-component surface reflection seismic data at the southern boundary of the Powder River Basin in Wyoming. My interest, besides studying fractures with the standard shear-wave techniques, is to explore P-wave methods and to correlate P-wave seismic attributes with the results of shear-wave analysis.

There is probably no single seismic attribute that will always tell us all that we need to know about fracture zones. Therefore, my approach in this project is to integrate the principles of Rock Physics into a quantitative processing and interpretation scheme that exploits, where possible, the broader spectrum of fracture zone signatures: (1) anomalous compressional and shear wave velocity; (2) increased velocity anisotropy; (3) amplitude vs. offset (AVO) response, and (4) variations in frequency content.

Throughout the field site, the fracture *directions*, inferred from the shear-wave rotation analysis on all four lines, trend consistently SW-NE – all generally within about 20° of each other. These trends were taken to be equal to the polarization direction of the

fast shear wave after rotation. The fracture *intensity* was taken to be proportional to relative time difference between the fast and slow shear waves at each location. This travel time difference (inferred fracture intensity) is highly variable throughout the site – the corresponding shear-wave anisotropy in the Frontier-Niobrara zones ranges from near zero to as much as 7 percent. The regions of largest anisotropy along the four lines can be interpreted with two localized zones of relatively intense fracturing.

Several attributes of the P-wave data were found to be consistent with, and possibly indicators of fractures: Strong lateral variations in P-wave reflectivity, AVO response, and frequency content were observed. Although we did not attempt to model quantitatively their response, they could be indicators of gas and fractures. However, such scalar attributes along a single 2-D line – no matter how striking – cannot give information about the direction of fractures that is so critical for designing wells. It is possible that with more work, we could learn to combine these scalar attributes with independent fracture direction information (for example from regional trends, or measured stress directions) to quantitatively characterize fractures. We recommend further work in learning to quantify the various P-wave scalar attributes associated with fractures.

Perhaps most intriguing are the several indications of P-wave anisotropy that I observed. Azimuthal variations of AVO response and P-wave stacking velocity were observed at two locations where lines intersect. The azimuthal velocity variation is consistent with the directions of the fracture model.

Important conclusions are that P-wave fracture attributes look promising, but at the same time 2-D single component surveys are likely to be inadequate for fracture mapping. In our survey, only two line intersections allowed us to even look for azimuthal P-wave variations. We recommend looking for these variations in 3-D single component data. 3-D data will allow, in general, a more complete sampling of azimuths at many CDPs. Partly as a result of this work, new 3-D studies are underway to look for fracture-related azimuthal variations of P-wave stacking velocity and AVO.

4.1 Introduction

In situ permeability can be largely controlled by natural fracture systems. In tight formations, which can include sandstones, shales, limestones, and coal, often the only practical means to extract hydrocarbons is by exploiting the increased drainage surface provided by natural fracture zones (Szpakiewicz et al., 1986; Lorenz et al., 1986). Before effectively using these fractures, the practical difficulties that must be overcome include: locating the position of fracture zones, determining the orientation and intensity of fracturing, and characterizing the spatial relationships of these fractures relative to reservoir heterogeneities which might enhance or inhibit the eventual gas flow.

Reflection seismic methods are, and will continue to be, the key geophysical tool for imaging these heterogeneities in the subsurface of the earth. Seismic methods provide a unique combination of penetration range and resolution that is not achievable by any other means. During the last ten years, considerable emphasis has been placed on seismic velocity anisotropy as the key indicator of fractures. Multicomponent VSP and surface reflection seismic studies have shown striking evidence for anisotropy, primarily from shear wave splitting (Alford, 1986; Crampin et al., 1986; Mueller, 1992). Most seismic studies have focused only on these relatively expensive multi-component (shear-wave) methods. Yet, we have not exploited fully the velocity, amplitude, and frequency information in the better-established and more cost-effective single-component (P-wave) data.

This field project, jointly funded by the U.S. Department of Energy, Amoco and Arco, is part of a larger fracture research project that includes:

- Rock Physics studies of the anisotropic viscoelastic signatures of fractured rocks,
- theoretical studies of fracture detection using P-wave data,
- acquisition and processing of seismic reflection field data, and
- interpretation of seismic and well log data.

The study site is in a producing field operated by Amoco and Arco at the southern boundary of the Powder River Basin in Wyoming. During the winter of 1992-1993 we collected about 50 kilometers of nine-component reflection seismic data and obtained existing log data from several nearby wells. This chapter describes the geologic setting, along with the collection, processing, and interpretation of the seismic data.

Although part of the field project is to apply the standard shear-wave techniques, the real goal in this project is to find non-shear wave methods (i.e., single component, P-

wave data). The motivations are: (1) Four and nine-component data are 50 - 500% more expensive to collect and process than conventional P-wave data; (2) Most existing data (including all marine data) are conventional compressional-wave data; (3) More and more 3D P-wave data of higher quality are becoming available, and a variety of their orientation-dependent attributes may be used to study the anisotropic properties of the Earth (Lewis, 1989).

There is probably no single seismic attribute that will always tell us what we need to know about fracture zones. Therefore, my approach in this project is to integrate the principles of Rock Physics into a quantitative processing and interpretation scheme that exploits, where possible, the broader spectrum of fracture zone signatures:

- anomalous compressional and shear wave velocity,
- increased velocity anisotropy,
- amplitude vs. offset (AVO) response,
- variations in frequency content.

As part of the project I have refined some of the theoretical rock physics tools discussed in chapters 2 and 3. These tools are very useful for linking the observed seismic signatures to the physical description of the fractured rock.

Numerous field studies have repeatedly demonstrated evidence of in situ seismic anisotropy. The majority of these have employed analyses of shear-wave splitting observed in reflection surveys (e.g.., Alford, 1986; Willis et al., 1986, Mueller, 1992) and vertical seismic profiles (VSPs) (Beydoun et al., 1985; Crampin et al, 1986; Johnston, 1986). Crampin (1978, 1988) and Crampin et al. (1980, 1985), among others, have also observed evidence of shear wave splitting above small earthquakes. Mueller (1992) found, in addition, that shear wave splitting can be accompanied by differences in reflectivity between the two principle components. We have also found evidence of fracture-related anisotropy for both P- and S-waves in this DOE-sponsored field study of fractured reservoirs.

4.2 Regional geologic framework and site description

The "Fort Fetterman" site is located at the southwestern boundary of the Powder River Basin, north of the town of Douglas, in Converse County, east-central Wyoming. The detailed descriptions of the regional geologic framework and the survey site are given in Appendix B.

This study is primarily concerned with Upper Cretaceous sediments. Figure 4.1 shows the regional stratigraphy. The major source rocks are Lower Cretaceous shales (Skull Creek and Mowry) and the Upper Cretaceous Niobrara Formation, which is also a reservoir itself.

The Niobrara Formation is a series of fractured marine chalks and limestones interbedded with calcareous shales and bentonites, and the Frontier Formation is fractured, offshore marine bar sand containing interbedded shales. They are both important oil and gas reservoirs in the study area.

Studies of the Frontier Formation in adjacent basins have found closely spaced fractures that are confined to individual sand members and form vertically discontinuous strands. Within the study area, fracture identification (dipmeter) logs demonstrate that the Frontier Formation also contains fracture sets. Core descriptions indicate that the Frontier is a fine grained, tight sandstone with a trace of oil. The formation velocity from the sonic log (Figure 4.1) is about 15,400 ft/sec, and the density is 2.5 g/cm^3.

The Niobrara Formation is also a low permeability reservoir. Porosities in the Niobrara chalk are around 8 percent. In the study area, the formation velocity is approximately 13,300 ft/sec, and the density is about 2.3 - 2.5 g/cm^3.

The survey site is in a producing tight gas field operated by Amoco and Arco. We collect log data, mainly in paper form, and completion information from about 16 wells. Dry, gas, oil, and gas-oil wells are clustered in the survey area, indicating the presence of strong reservoir heterogeneity.

4.3 Seismic data acquisition

The seismic data collection work was contracted to Amoco's Party 45, which is operated by Grant-Tensor. Four vertical component and four rotating base-plate horizontal component trucks were used as the seismic sources throughout the data collection.

4.3.1 Field layout and geophones

The original plan was to shoot two two-dimensional seismic lines, lines 1 and 2, with funding from the DOE and Amoco. Line 1 strikes northeast and line 2 northwest (Figure 4.2). Their lengths are 13.8 km and 16.6 km, respectively. Later, during the data acquisition stage, we obtained additional funding from Amoco and Arco/Vastar Resources to shoot two shorter lines, line 3 (10.8 km) and line 4 (8.1 km). These are both nearly parallel to line 1. This arrangement gives us far more extensive coverage of the

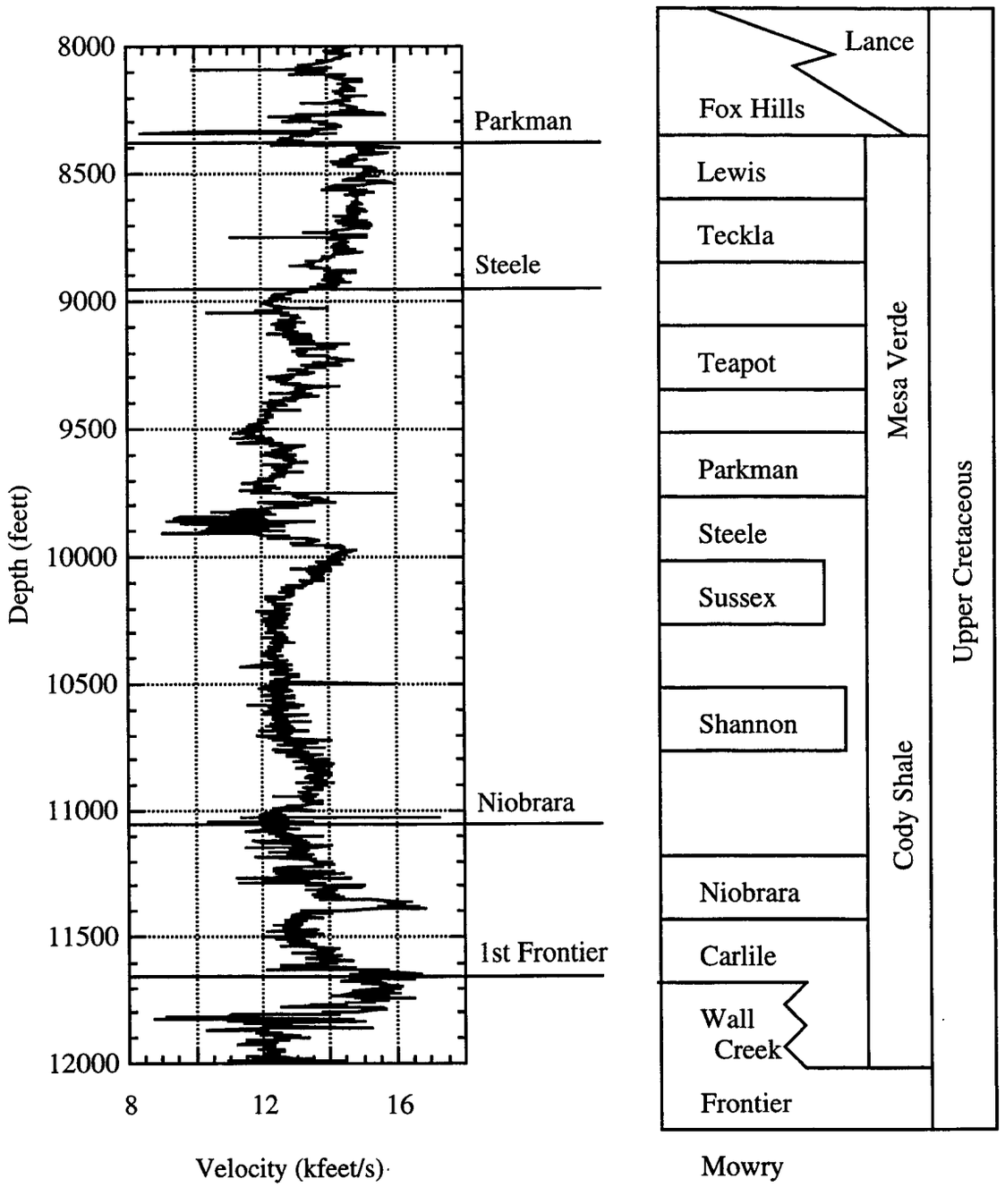

Figure 4.1: Region Stratigraphy. (a) Sonic log from Apache #36-1 State well marked with formation tops. (b) Upper Cretaceous stratigraphy, Powder River Basin (from Wyoming Geol. Assoc. Guidebook).

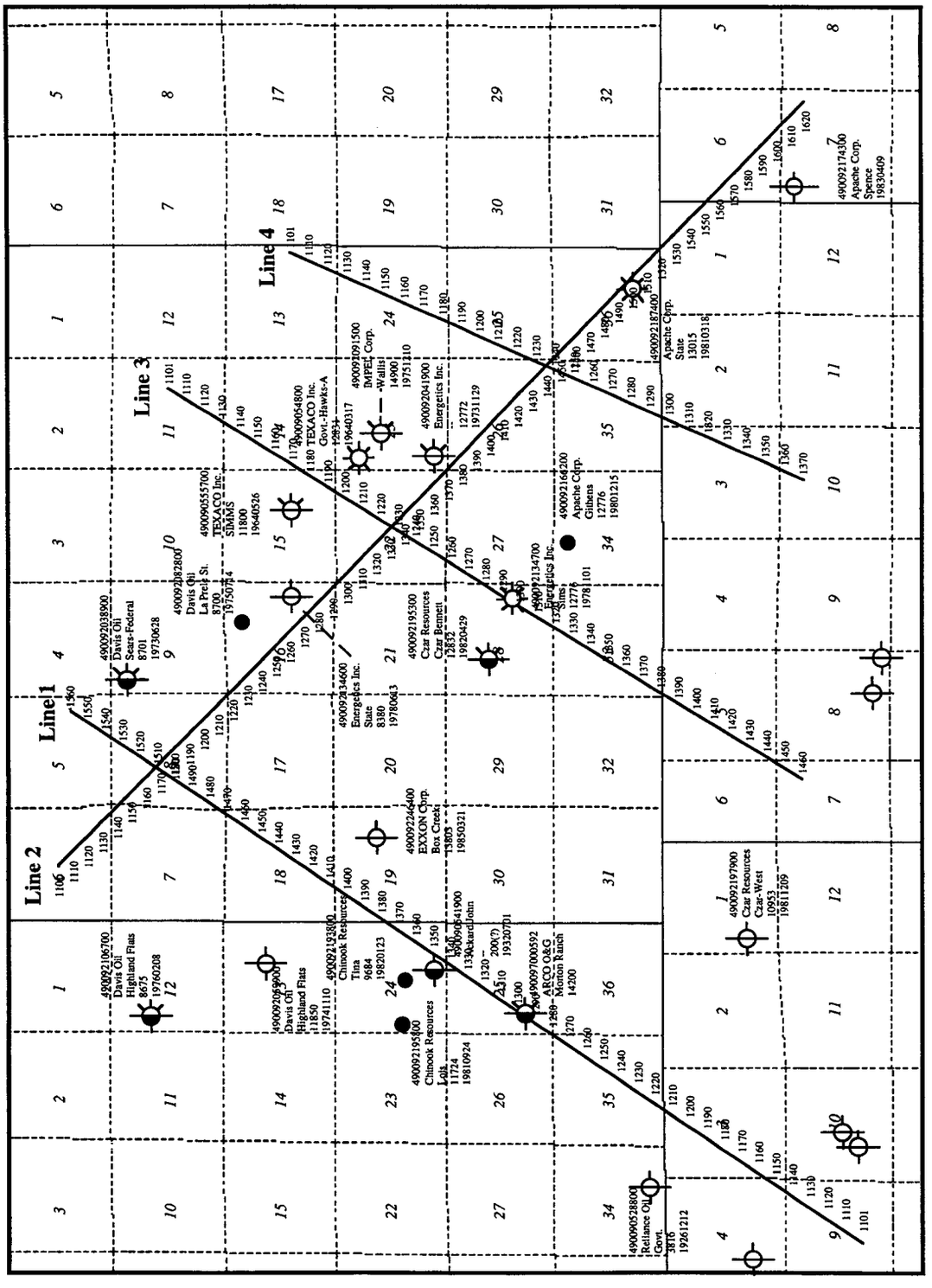

Figure 4.2: Base map of the study site showing locations of survey lines 1 to 4 and 26 wells. The caption next to a well indicates the well's API number, operation company, name, total depth, and completion date.

survey area and the data reveal interesting lateral variations in terms of compressional wave amplitude, azimuth-dependent stacking velocity, shear wave splitting and P-SV/SH wave conversion.

The model of the geophones used in the seismic survey was SGR IV, manufactured by Geospace. The geophone spacing (group interval) was constant throughout the study at 30 meters. In each group there were six compressional-wave geophones polarized in the vertical direction. The geophones were evenly spaced at 5 meter intervals and centered on the group flag. Six horizontal (shear-wave) geophones were deployed in the same spatial pattern with their polarization parallel to the survey line, and six geophones had their polarization perpendicular to the survey line (Figure 4.3). A low-cut filter (3Hz) and 60Hz rejection were applied in the field. This geophone group allowed us to record all three components of the seismic signal from each shot. To simplify our discussion, we shall call the vertical component P, the in-line component S1 and the cross-line component S2.

There were 721 channels in every shot gather. Channel 1 was an auxiliary channel used for noise control purposes. Channels 2-241 recorded P-wave from the source. The in-line and cross-line components of the reflected shear-waves were recorded by channels 242-481 and 482-721, respectively. 60/180 split was used for most of the shots except for those at the end of the lines. This gave a maximum offset of 5,400 meters (18,000 feet) for most of the shot records, although sometimes the offset could be as large as 7,200 meters (24,000 feet). Note that the target depths of interest were at about 3,300 meters (11,000 feet).

4.3.2 Sources

We used three types of vibroseis sources. Conventional vertical (P-wave) vibrators generate nearly vertical particle motion by shaking the ground up and down, while shear-wave vibrators shake the ground horizontally. Two orthogonal polarizations are possible for the shear wave sources. We chose one to be in-line with the survey line (S1) and the other perpendicular to it (S2). Because we use three types of sources and receivers, and all three components of every shot are recorded, we obtain nine different sets of data for each survey line. In the later discussion we shall call them by their source and receiver types, such as P-P, denoting signals recorded from P sources to P receivers , and S1-S2 from in-line shear sources to cross-line shear receivers.

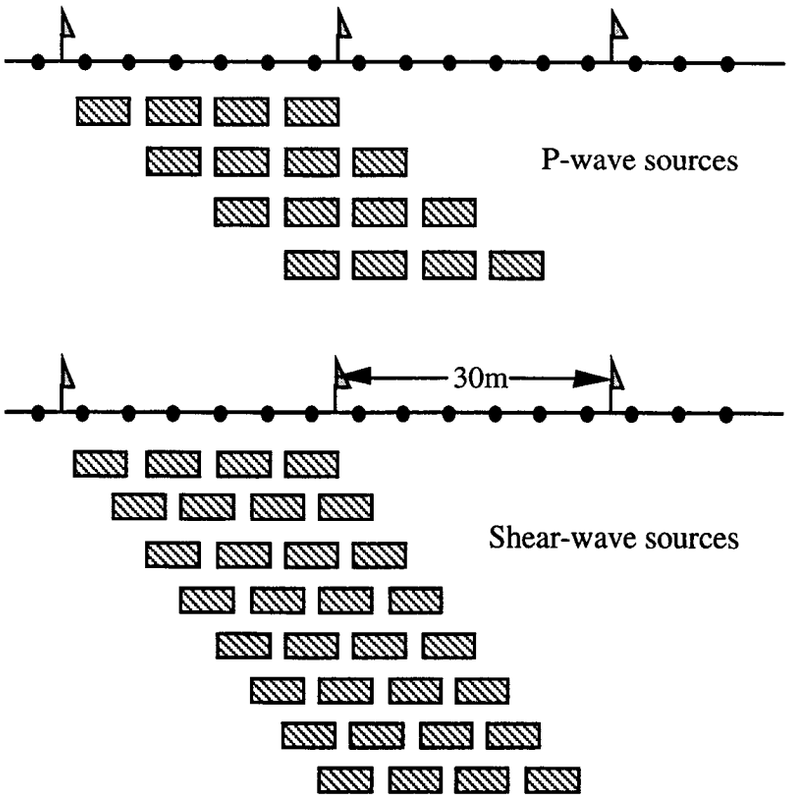

Figure 4.3: Geometry of the source and geophone arrays. The group interval is 30 m. For each component, six geophones are spaced evenly at 5 meter intervals and centered on the group flag. The moveup is 7.5 m for the vertical component trucks, and 3.75 m for the horizontal component trucks.

Four vibrator trucks aligned along the survey line are used simultaneously for each type of source (Figure 4.2). High quality signals were obtained by ground force phase locking on the vibrators. Every "shot" consisted of several sweeps. The trucks uniformly moved forward along the line a small distance after each sweep. The number of sweeps was four for P-wave sources and eight for shear sources. Higher number of sweeps for shear sources was necessary because shear-waves usually attenuate faster than P-waves. To maintain the same source group length the move-up was 7.5 meters for P-wave sources and 3.75 meters for shear-wave sources. Diversity stack summing was performed in the field.

After analyzing the test shot gathers and taking into account the depth of our targets, the large offset of the geophone array and the data volume, we decided that 4 msec sampling rate (125 Nyquist frequency) was appropriate for this project. Most of the P-wave signal energy was limited within 10 - 50Hz frequency band while no discernible shear-wave signal existed beyond 30Hz. The P-wave vibrators swept from 7 to 90 Hz

and the shear-wave vibrators from 7 to 50 Hz. All sources swept for 10 seconds and the receivers listen for 18 seconds, which gave us 8 second data per channel after correlation. This was based on the fact that the two-way travel time of the deepest target was about 2.5 seconds for P-wave and 4.5 seconds for shear wave.

Our design of the field layout followed the well-known stack array approach. Signals from a number of evenly spaced sources and receivers were stacked to form a single shot gather. This kind of stack array is commonly used to suppress the ground roll and other coherent noises (Anstey, 1986; Hildebrandt et al., 1986). Our design is illustrated in Figure 4.3. The VP stations were centered between the flags, and the VP interval was 60 meters (shot every other group). The field parameters are summarized in Table 4.1.

Sometimes a vibrator truck would malfunction and a few shots were collected with only three vibrators. In such cases more sweeps were done to compensate for the loss of total source energy.

Figure 4.4: Vibrator trucks used in the seismic survey.

Table 4.1: Acquisition parameters.

Group interval	30.0 meters
Three-component sources, three-component receivers	
6 geophones per group component, centered on the flag	
240 channels per component, 180/60 split-spread shooting	
Four vertical (P-wave) vibrators, four rotating base-plate horizontal vibrators	
P-wave	4 sweeps, 7.5 meter move-up
Shear-wave	8 sweeps, 3.75 meter moveup
Frequency range: P-wave 7-90Hz, shear-wave 7-50Hz	
Sweep length	10 seconds
Listen length	18 seconds
Record length	8 second
Field Filter	3 Hz low-cut, 60 Hz rejection

4.3.3 Dataset

The data acquisition work was done between October 26, 1992 and January 17, 1993. According to the observer's sheet, the ground was wet most of the time during the shooting of line 1 and line 2, and afterwards it was covered with snow while shooting lines 3 and 4.

The data were delivered in SEGY format on 21 8mm exabyte tapes. For each survey line the file number starts from 1 and increases in increment of one. There are 749, 832, 584, and 425 files for lines 1, 2, 3 and 4, respectively. The total data volume is roughly 17 gigabytes.

The convention for numbering the sources is the same for all four lines. For a given line, the source point number starts with 101 as the last three digits. The P-wave sources are numbered in 1000 series, S1 (in-line shear) sources in 2000 series and S2 (cross-line shear) sources in 3000 series. The noise files are numbered in 5000 series. For example, the first P-wave, S1 and S2 sources are numbered 1101, 2101 and 3101, respectively, even though they are actually at the same location. The geophones are numbered in a similar fashion, with P-wave geophones in 1000 series, S1 geophones in 2000 series and S2 geophones in 3000 series, starting with 101 as the last three digits.

A few header words are preloaded in the SEGY files. Their name, byte offset, length and format are listed in table 4.2. SHT_STAT, REC_STAT and CDP_SHAT represent shot, receiver and CDP station numbers.

The ground survey was carried out in October, 1992, and the measurement of the absolute x-y coordinates and elevation for every station was compiled in four ASCII files, one for each line. The data was delivered in IBM PC format.

Table 4.2: Header words preloaded in the data.

Name	Byte offset	byte length	format
SHOT	9	4	INT
SGRSN	191	2	INT
GLCFNF	193	2	INT
DATE	195	4	INT
PERPOF	199	4	INT
SHOT10	203	4	INT
OLDOFF	207	4	INT
STATIC	211	2	INT
LINNDX	213	2	INT
TYPE	215	2	INT
DCBIAS	271	4	IBMFL
CDP-STAT	183	2	INT
SHT-STAT	185	2	INT
REC-STAT	187	2	INT

4.3.4 SGR gain problem

After data acquisition of the four nine-component seismic lines, we plotted the stacking chart display of the line 2 S2-S2 trace amplitudes after spherical divergence correction (Figure 4.5). In Figure 4.5 each pixel represents the root-mean-square (RMS) amplitude of a trace within a time window, which was selected to contain a fixed set of events. The receiver and source station numbers were used as the horizontal and vertical coordinates in the plot. The checkered appearance suggested a gain problem of the recording instrument.

Our partner at Amoco also noticed the problem and investigated the causes. A program bug caused "most traces recorded on 4-channel SGRs (SGRNO > 400) to be 1/16 of the correct amplitude". The correction is made by simply multiplying amplitudes in each erroneously recorded trace by 16. A map of the affected traces is available for this purpose.

Figure 4.6 (a) shows the amplitude plot of the corrected line 2 S2-S2 traces of line 2. It looks normal and consistent with the amplitude plot of the traces after applying AGC correction (Figure 4.6 (b)). It is essential to correct the gain problem before any true amplitude processing, otherwise no conclusions drawn from true amplitude can be trusted.

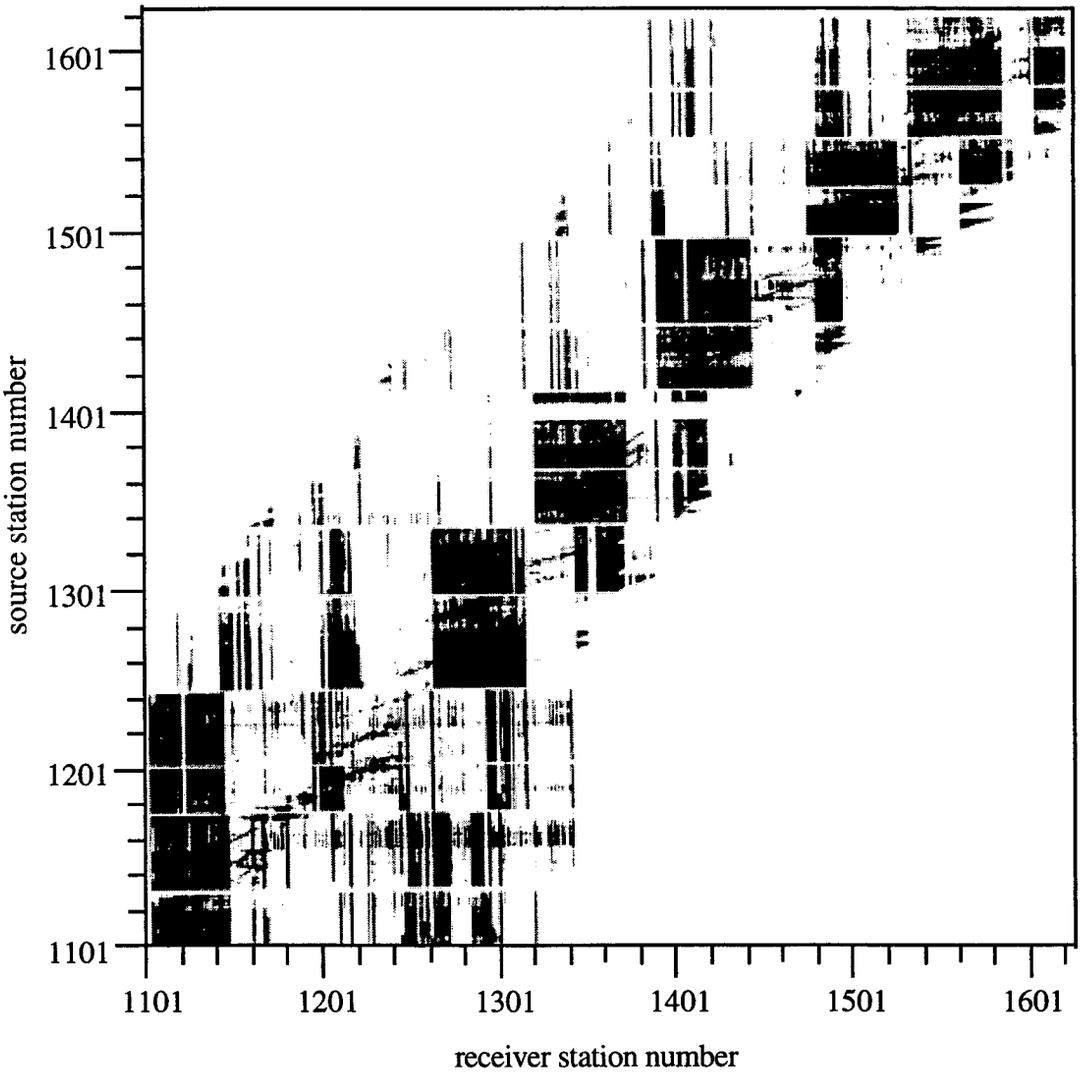

Figure 4.5: RMS amplitudes of S2-S2 traces without gain correction. The horizontal and vertical coordinates are geophone and source station numbers, respectively. The patchy appearance indicates the systematic severe gain errors that contaminated the data before applying the corrections.

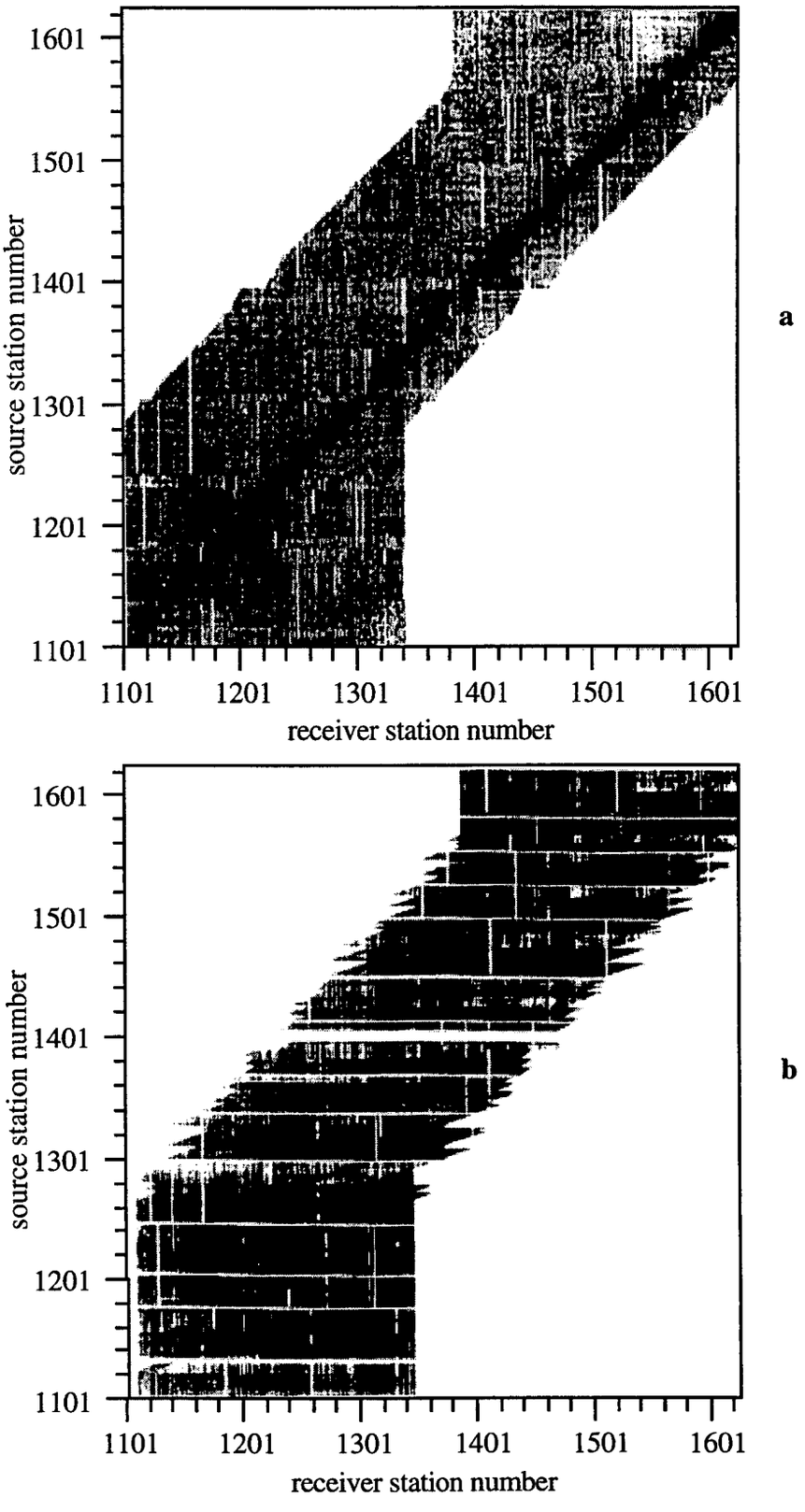

Figure 4.6: RMS amplitudes of S2-S2 traces of line 2. (a) after gain correction, (b) after applying AGC.

4.4 shear-wave data and validation

Lab measurements (Banik, 1984; Thomsen; 1986, Vernik and Nur, 1992), VSP (Beydoun et al., 1985; Crampin et al., 1986; Johnston, 1986) and surface seismic data (Alford, 1986; Lewis, 1989; Mueller, 1992) have shown that sedimentary rocks are often anisotropic. One of the major sources of anisotropy is the inclusion of natural fractures.

Multi-component shear-wave exploration techniques have long been used in the oil industry to study the anisotropic properties of the Earth (Alford, 1986; Wallis et al., 1986; Thomsen, 1986; Lewis, 1989). Shear-wave splitting has been observed in various places and reported by many authors. Crampin and others have argued convincingly that shear-wave splitting is the result of azimuthal anisotropy, which may be stress-induced or related to non-randomly oriented fractures in the Earth's crust.

In tight gas reservoirs, azimuthal anisotropy is often related to natural fractures. If this is the case, the preferred orientation of the fractures can be obtained from the rotation angle of the shear-wave splitting analysis, and the relative density of fractures is indicated by the amount of travel time difference between the fast and slow shear waves after rotation. This method has been demonstrated to be successful in identifying highly fractured regions, for example in the Austin chalk (Mueller, 1992).

In our study we explore new methods to study fractures in tight gas reservoirs using also P-wave data. We will begin by using the well-developed shear-wave techniques combined with well control to obtain a reference model of fracturing in the region. The results of our P-wave data processing and interpretation will then be compared to the shear-wave model for validation.

4.4.1 Raw Data and Gain Correction

Figures 4.7 and 4.8 show two typical field records of the shear-wave data. Automatic gain control (AGC) has been applied to balance the amplitudes. Notice that no consistent hyperbolic-shaped events are identifiable in the raw shear-wave data in Figure 4.7, and Figure 4.8 is only marginally better. The relatively noise-free time window that we often see in P-wave data between the first arrivals and the surface waves simply does not exist in the shear-wave data because of the small velocity difference between the shear-waves and the surface waves. Serious ground roll contamination, together with strong attenuation, resulted in low signal-to-noise ratio and loss of higher signal frequencies.

There is an interesting feature in Figure 4.9 that is worth explaining. The record is dominated by a sequence of hyperbolas with similar amplitude and perfect period, whose

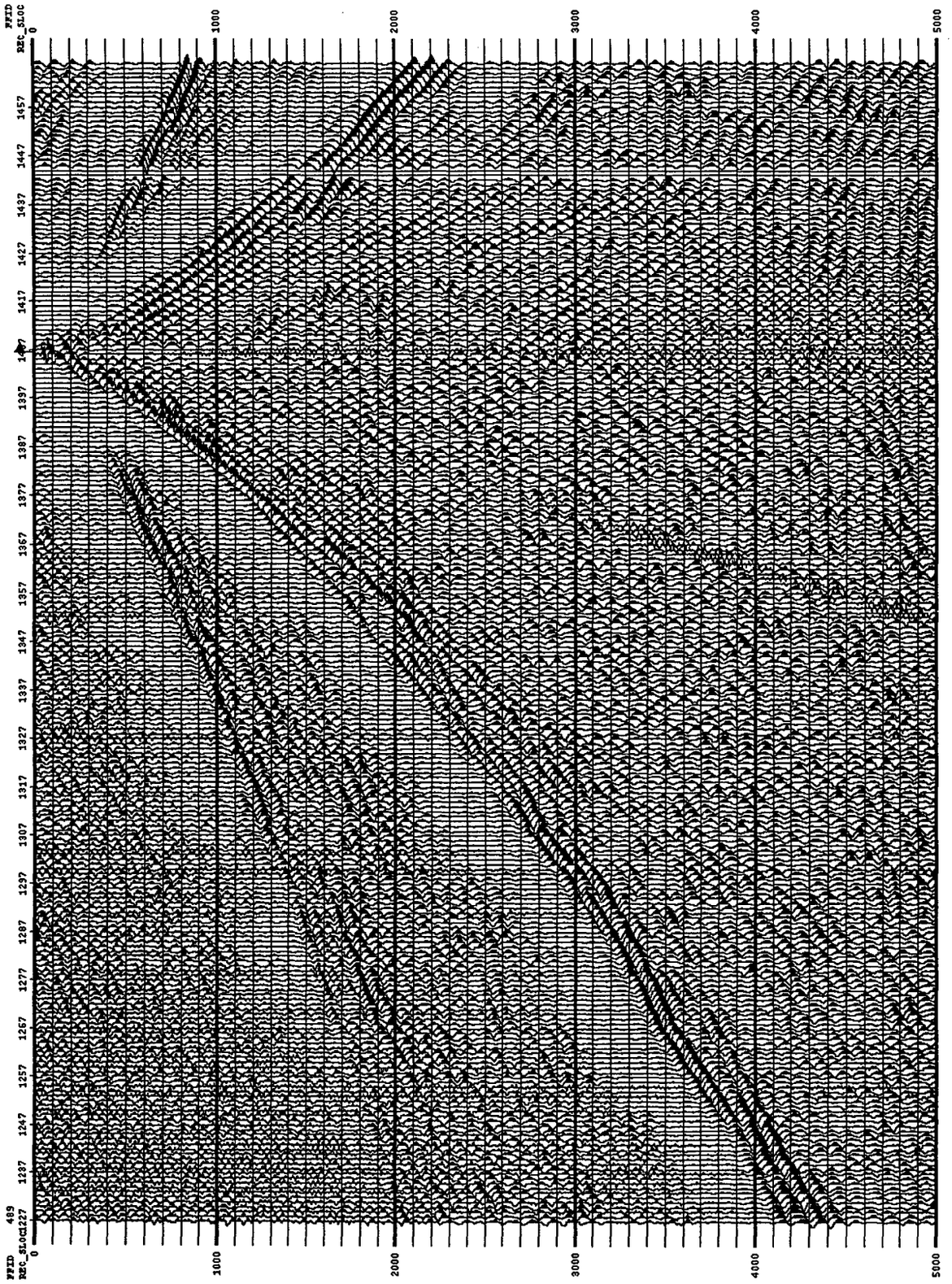

Figure 4.7: S1-S1 field record 489 of line 2 (AGC applied).

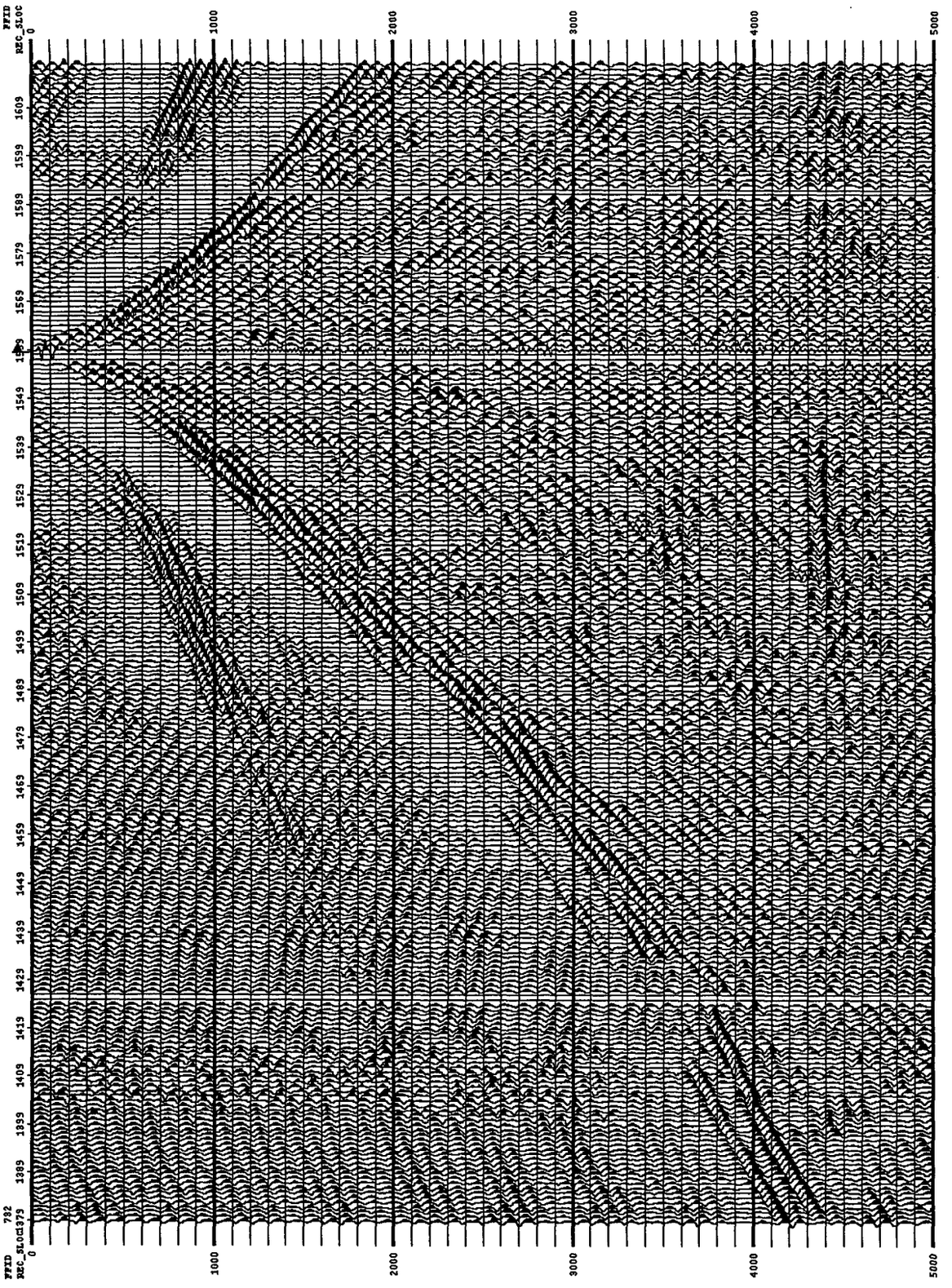

Figure 4.8: S1-S1 field record 732 of line 2 (AGC applied).

center is not at the location of the source vibrators. In fact, when the field records are examined one by one, the center of those hyperbolas appears stationary at flag 1408 on line 2 and flag 1406 on line 3. Unfortunately, these nicely shaped "events" record cultural noise from a mill near the intersection of lines 2 and 3. The mill acts as a fixed off-line source and constantly generates noise. The noise source is located at a strategic position and a large portion of our data is contaminated, which further complicated the data processing. The existence of this noise source was not discovered during the field test stage because the test location was too far away from the mill to detect its noise. There is no mention of this problem in the observer's sheet.

The average power spectrum of 20 traces of the shear-wave data is shown in Figure 4.9. The spectral analysis was performed on the raw data with only a time window from 2 to 5 seconds applied, and the result was normalized by the maximum frequency component. The magnitude of the frequency components drops sharply by about 30db from 10 to 20 Hz and remains stable thereafter. The flat tail of the power spectrum represents the ambient noise level.

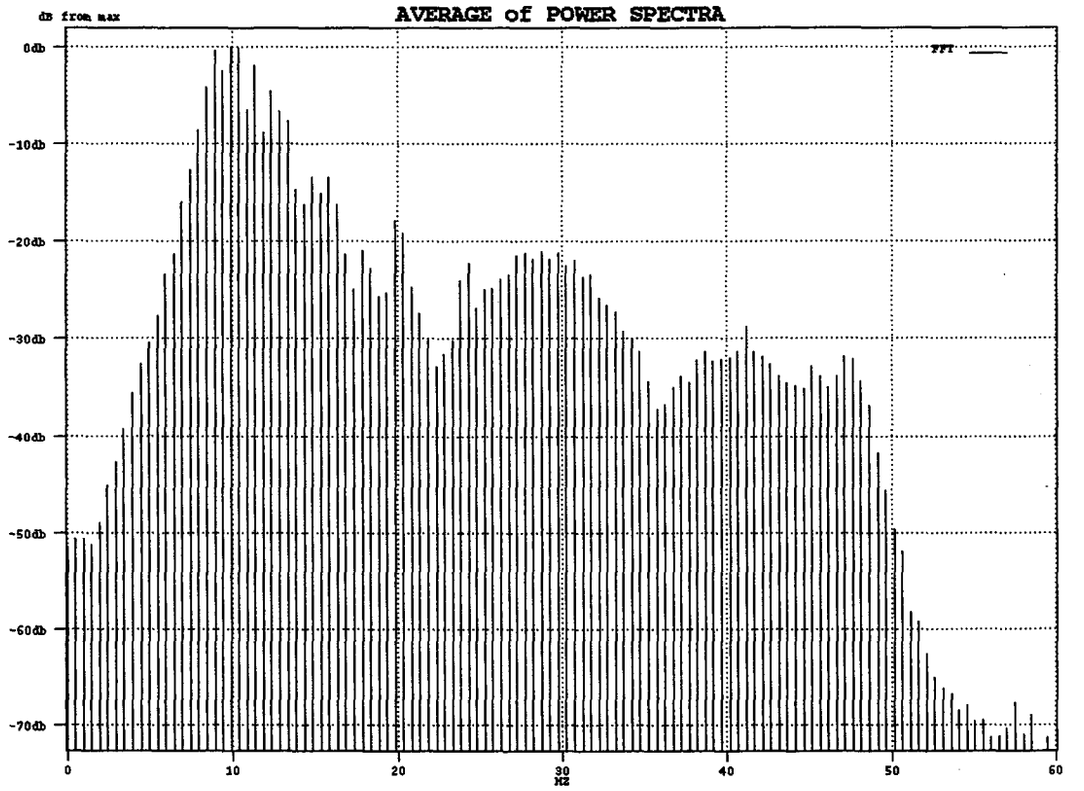

Figure 4.9: Power spectrum of shear-wave data.

Figure 4.10 shows the frequency panels in 10 Hz intervals of a shear wave field record. As expected, there is not much useful information beyond 20 Hz. Based on the observations from Figures 4.9 and 4.10, we conclude that for our shear-wave data, a sampling rate of 8 msec is more than adequate for the purpose of signal processing. All raw shear data were decimated from 4 msec to 8 msec sampling rate, thus effectively halving the data volume and speeding up the processing by almost a factor of 2. The Nyquist frequency corresponding to 8 msec sampling rate is 62.5Hz, which is three times the useful signal frequency. After the desampling, the size of one component of the shear-wave data set is about 140 Mbytes for the longer lines (1 and 2) and 80 Mbytes for the shorter lines (3 and 4).

The first step of the data processing was to correct the gain error using the gain correction table provided by Amoco. The whole data set was scanned trace by trace, and whenever the entry in the gain correction table for a trace is 1, indicating a correction is needed, that trace was multiplied by 16. The detailed discussion of the gain problem and the format of the gain correction table can be found in a separate document "SGR gain problem on Ft. Fetterman data". Gain correction is important because the Alford rotation method used to determine the orientation of the anisotropy totally depends on the relative amplitudes of the four-component shear-wave data. Although the rotation method has been shown not sensitive to the strength of the two orthogonal shear-wave sources (e.g., Lewis, 1989), an unbalanced gain like this is severe enough to render any result unreliable.

4.4.2 Noise reduction

As with most shear-wave data, ours were highly contaminated with ground roll. In P-wave data, coherent noise such as ground roll is often isolated in the F-K (frequency - wave number) space and thus can be eliminated using F-K dip filtering. However, in our shear-wave data most of the signal energy lies within the 10 to 20 Hz frequency band, which is almost the same as for the ground roll, and the signal velocity is similar to that of surface waves. In this case no isolation between the signal and the noise existed in the F-K space. F-K filtering was not very effective for improving the signal-to-noise ratio. As an example, Figure 4.7 shows a field record from line 2, and Figure 4.11 shows its F-K spectrum. As we can see, there is no apparent signal-noise separation, and we can not expect F-K filtering to improve the signal-to noise ratio. The test result of performing F-K dip filtering is shown in Figure 4.12. For this test a fan filter with parameters (-15 to 15Hz, -3,200 to 3,200 feet/sec) was used as the reject zone.

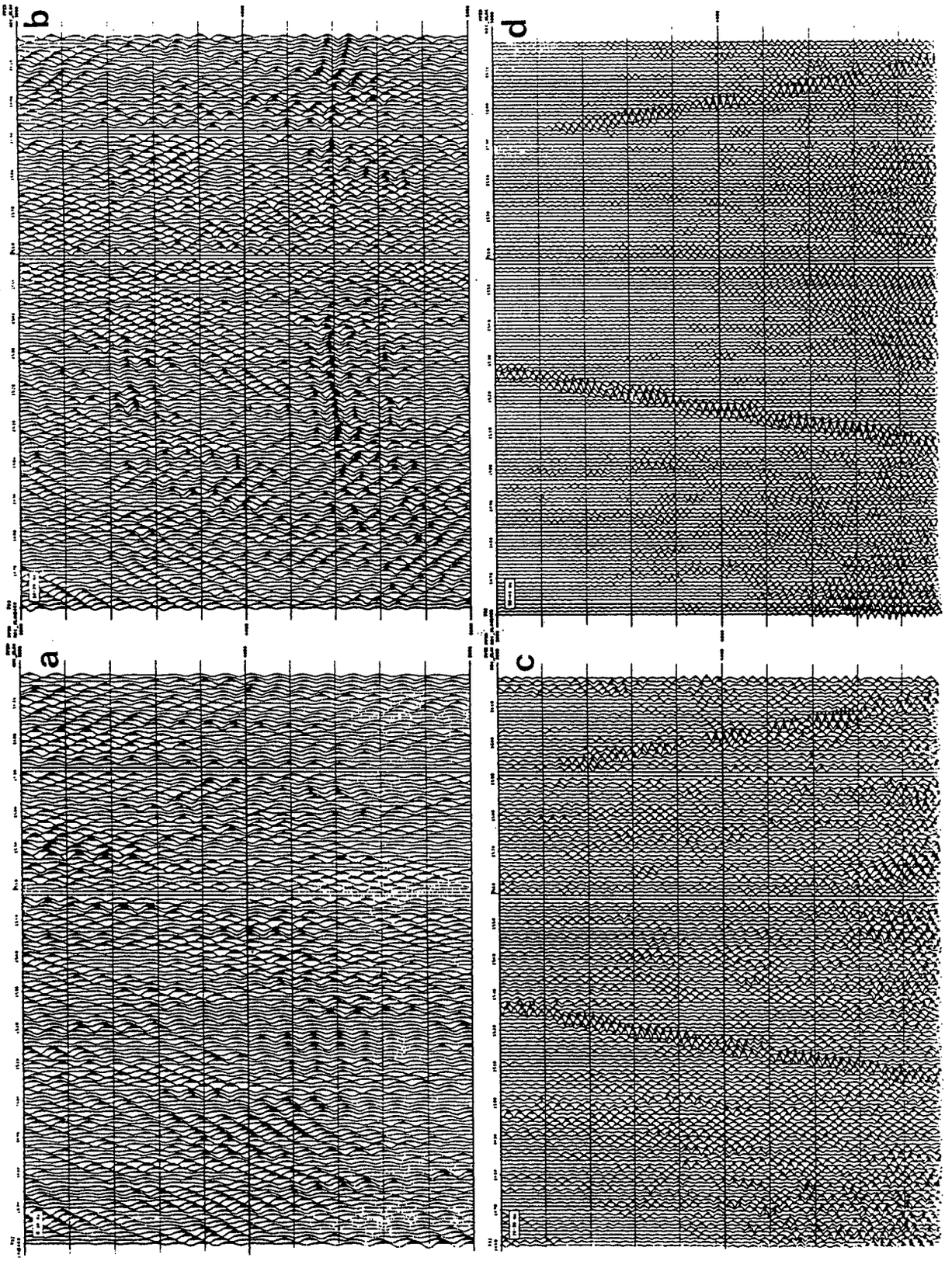

Figure 4.10: Frequency panels of S1-S1 data. (a) 0-10 Hz, (b) 10-20 Hz, (c) 20-30 Hz, (d) 30-40 Hz.

Another strong noise source was the mill located near the intersection of lines 2 and 3. The noise could be characterized by its stationary position in time and space and its near-perfect period. In terms of frequency and velocity, the noise was essentially surface waves and was therefore difficult to remove. To make things worse, the magnitude of the noise did not decrease with time in the records, and thus it affected deeper events more than shallower ones.

Seismologists at Amoco told us that the data could be somewhat improved by heavy τ-p filtering. The software they used, however, was developed in-house and was not available to us. We used ProMAX[1] to process the seismic data and chose not to repeat their noise reduction procedure.

We speculate that one could capitalize on the stationary character of the cultural noise and use a "spatial" filter to remove the surface wave coming from the off-line mill by linearly combining the data recorded by the in-line and cross-line geophones. We did not invest our time to further study this possibility for the following reasons. First, Alford rotation, which is a linear combination of the four component shear-wave data, will enhance the signal and reduce the noise automatically. Second, our processing result without heavy-duty noise reduction shows acceptable quality for the purpose of this study, which is mainly to establish a shear-wave reference model for our study of natural fractures using P-waves.

4.4.3 Velocity analysis

The first step of conventional velocity analysis is to select stacking velocity functions that will flatten the reflected events in the CDP gathers. On most of the field records of our shear-wave data we could hardly see any events (Figure 4.7), so velocities could not be picked prestack. Since at most CDPs our data had between 60 and 80-fold coverage, stacking greatly increased the signal-to-noise ratio. Therefore, our velocity analysis was based entirely on the quality of the stacked section

The velocity function at a CDP station was picked interactively using ProMAX's Interactive Velocity Analysis module. The quality of the stacked traces adjacent to the CDP station was inspected visually for maximum power and continuity until an "optimal" velocity function was found. This procedure was repeated every 40 CDPs. The resulting velocity field was used as a base for further adjustment. To fine-tune the velocity functions, we modified the base velocity field by ±3%, ±5%, ±7% and ±9%, and

[1] ProMAX is a trademark of Advance Geophysical Corp.

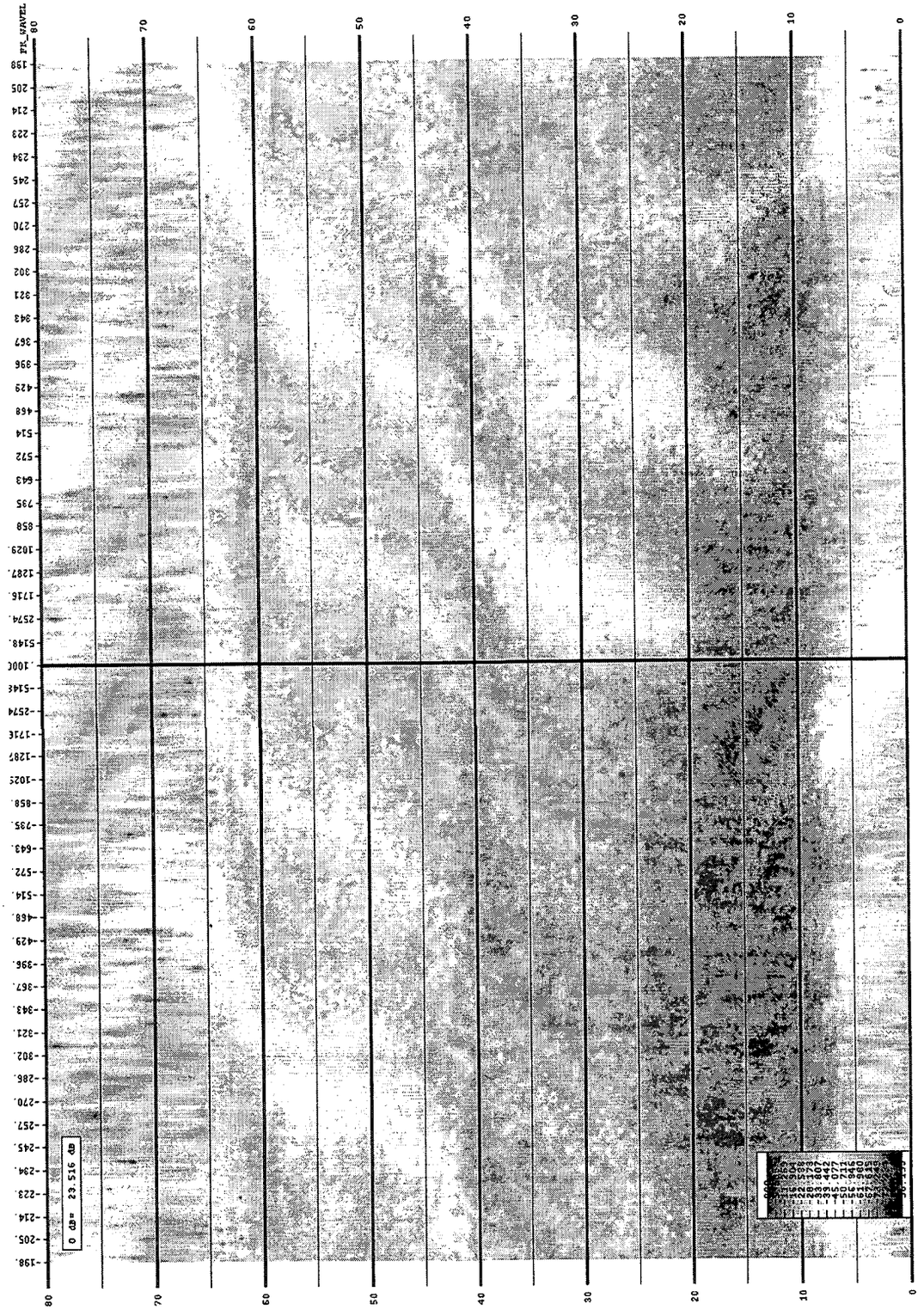

Figure 4.11: F-K spectrum of field record 489 of line 2.

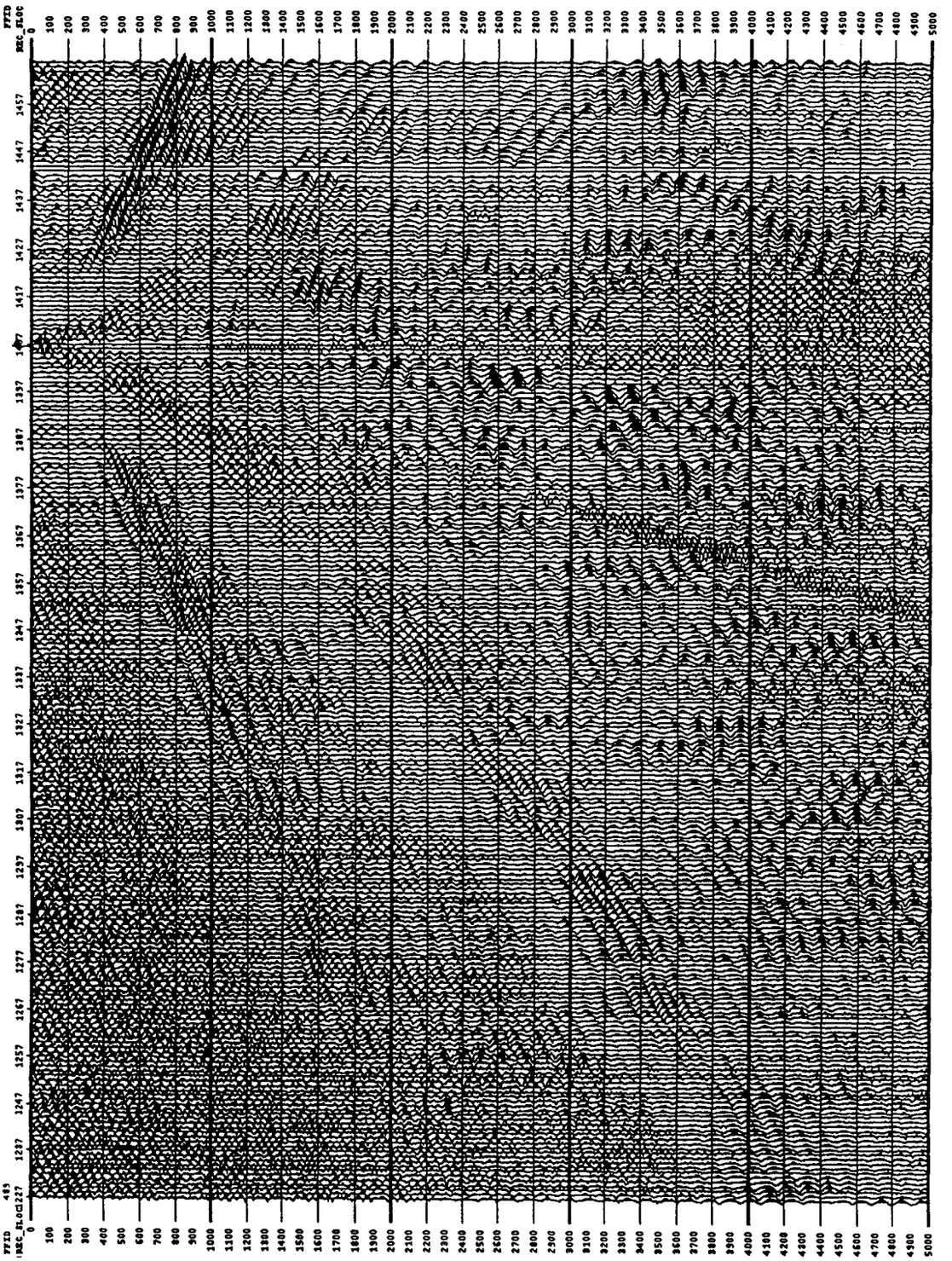

Figure 4.12: Field record 489 after F-K filtering.

stacked the data with the modified velocities. Small changes were then made to achieve the best stack result.

Conventional velocity analysis can be accurate to a few percent. Ours is most certainly worse. Furthermore, the velocity difference between the two shear-wave modes at our survey site is estimated to be no more than a few percent. Hence we saw no need to do velocity analysis separately for each of the four shear-wave components. A single velocity field was used to obtain the final stacks of a survey line, and the same velocity field was used to stack the rotated shear-wave data.

4.4.4 Statics

Time shifts of the reflection caused by the laterally varying shallow layers are a major problem for shear-wave data processing. The statics can cause more severe problems for shear-wave data than for P-wave data, because shear velocities are lower, and the time shifts tend to be bigger. Obtaining a good statics solution was a challenge and it required a lot of effort.

Elevation statics were applied to the data prior to stacking. The replacement velocity used was 3500 feet/sec and the datum elevation was chosen to be 4500 feet. The refraction static solutions were provided by M. Mueller at Amoco. After NMO correction, maximum power autostatics was applied over a 4-5 second time window.

4.4.5 Stack

With such a low signal-to-noise ratio, stacks with preserved amplitude were usually very poor. Even spherical divergence corrections could amplify some of the noise out of proportion. Therefore we found it useful to apply AGC to traces before stacking. The time window used for AGC was 1,000 msec. The flow chart of the stacking is listed in Table 4.3, and Figure 4.13 shows a portion of the final stack of line 2.

It is tempting to match the major events on the stack of shear-wave data to those on the stack of conventional P-wave data. Figure 4.14 shows the event ties between compressional-wave stack and shear-wave (S2-S2) stack. The time scale of the shear-wave stack was adjusted uniformly to compensate for the velocity difference between compressional and shear waves. The match is reasonable but not great. We have to bear in mind that P-waves and shear-waves have different wavelengths, and their acoustic impedance contrasts are not necessarily the same. Since no shear-wave acoustic logs are available, this kind of match is only tentative.

Table 4.3: Flow chart of shear-wave processing

Demultiplex: S1 geophone - channel 242-481, S2 geophone - channel 482-721
Gain correction
Elevation statics, datum elevation 4500 feet, velocity 3500 feet/sec.
Refraction statics
Automatic gain control, window size 1000 msec.
Component separation, CDP sort
Velocity analysis (quality controlled by mini-stack)
NMO
Maximum power autostatics
Final stack
Band-pass filter 8/12.5-20/25 Hz

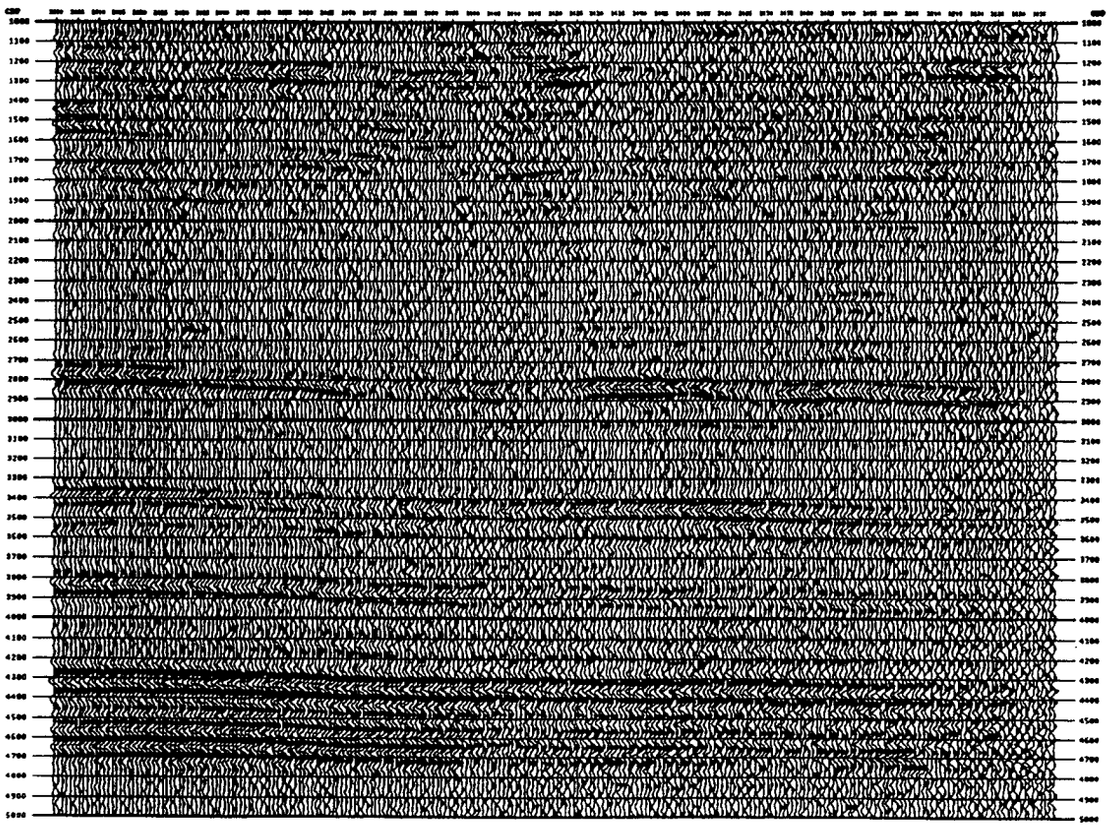

Figure 4.13: S2-S2 stack section of line 2.

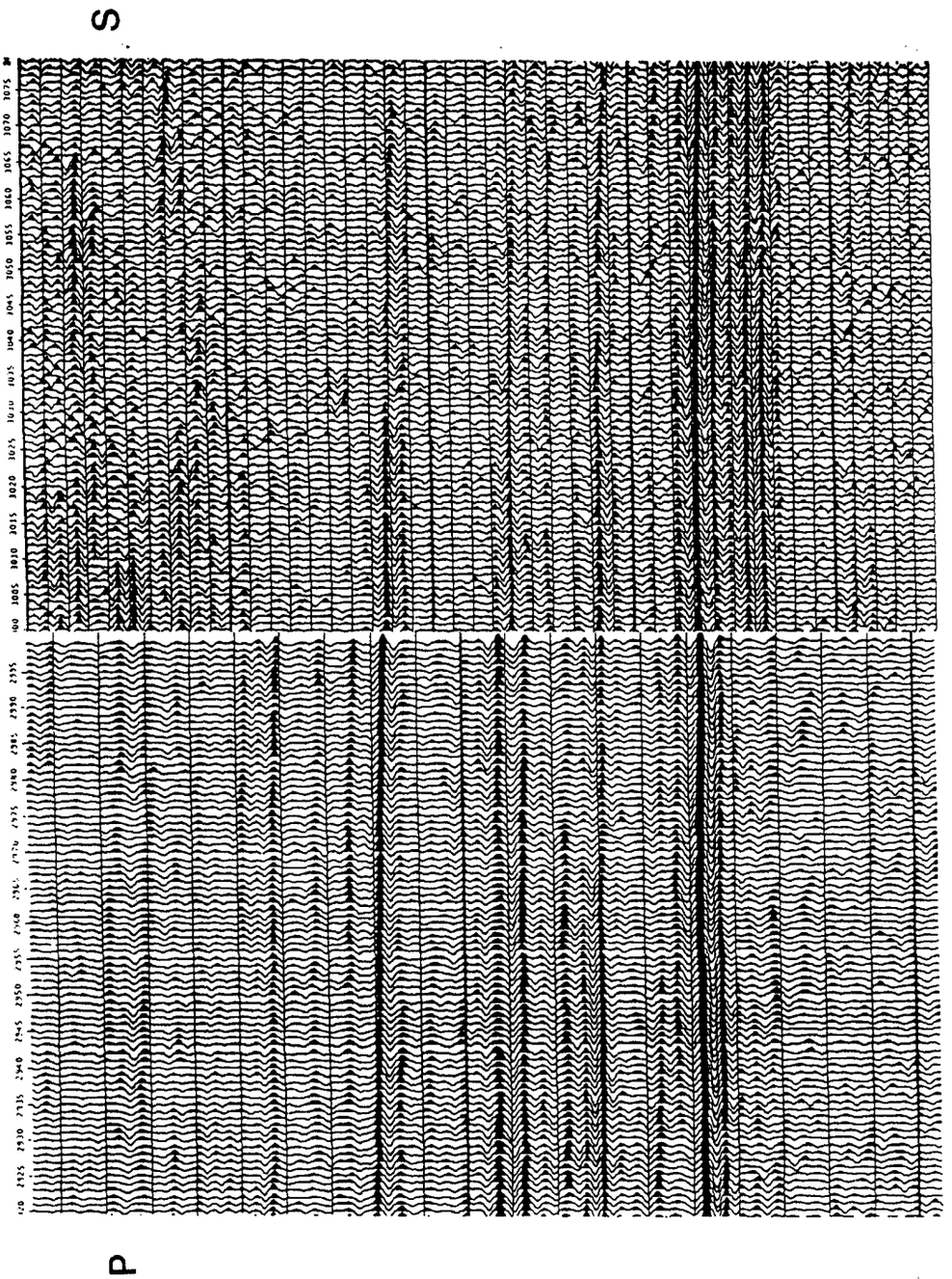

Figure 4.14: Event ties between P-P and S2-S2 stack sections of line 2.

Along 3 miles of the southern end of line 1 and 2 miles of the southern end of line 3, no events are observable on the S-wave sections. This is mainly due to structural complexity associated with the flexure to the south of the survey area. The rest of the lines show good events after stack, although they are not as continuous as those in the P-wave stacks. The events form several groups, and the most prominent events come from the Frontier formation. It is much harder, however, to identify the exact correspondence between the formations and shear-wave events, because until now no shear-wave sonic velocities are available, and the acoustic impedance contrast of P-wave and shear-wave may be considerably different.

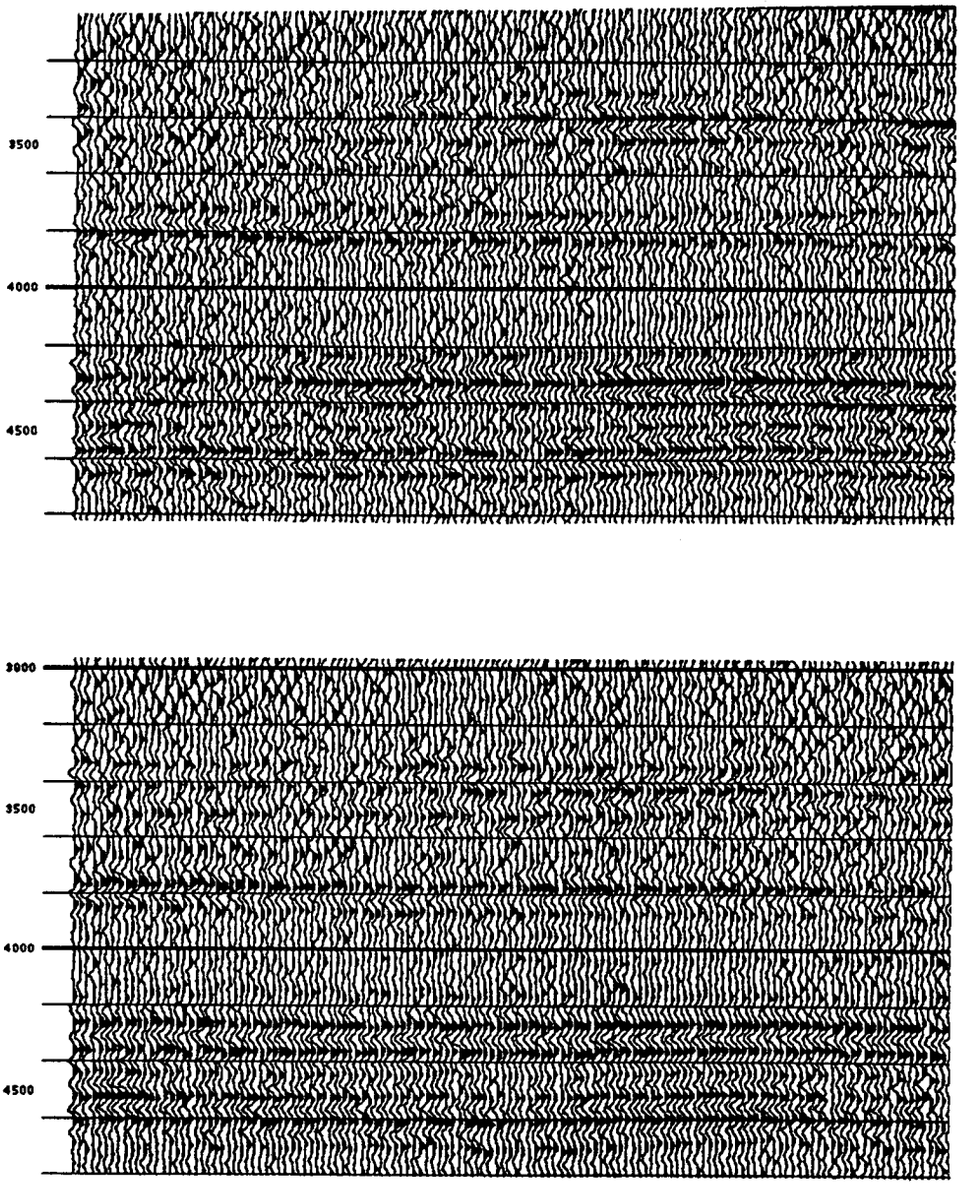

Figure 4.15: S1-S2 and S2-S1 stack sections of line 2.

The cross-components (S1-S2 and S2-S1) (Figure 4.15) observed in the final stacks are the most direct evidence of seismic anisotropy. All four components have comparable amplitudes, suggesting not only a significant amount of anisotropy, but also a considerable angle between line 2 and the symmetry axes.

4.4.6 Alford rotation

One purpose of collecting four-component shear-wave data is to determine the symmetry axes of the anisotropy at the survey site, which is assumed to be caused by nearly vertical natural fractures. The method we use is called Alford rotation (Alford, 1986), which uses shear-wave splitting to identify the symmetry axes of the medium.

Azimuthal anisotropy can come from several situations. For example, if all the fractures in a flat layer are vertical, the resulting effective medium (homogeneous Earth layer with fractures) has a horizontal symmetry axis, which is perpendicular to the fracture plane. Stress can also induce azimuthal anisotropy in an originally isotropic Earth layer if one of the principle stresses is vertical (Yin, 1992). In this case, however, the fractures or microfractures might not be all parallel, but angularly distributed around a horizontal symmetry axis. Azimuthal anisotropy can also be caused by thin layers, without any fractures, if the layers are upturned.

In a flat-layered isotropic Earth an in-line source would generate shear waves polarized only in-line, and a cross-line source would generate shear waves polarized only cross-line. There would be no cross-signal recorded in the cross-line receiver from the in-line source, and vice versa. However, with azimuthal anisotropy, each shear source (in-line and cross-line) generates a shear signal H that is decomposed into two components H_1 (= $H\sin\theta$) and H_2 (= $H\cos\theta$) traveling at different speeds, and polarized along the vertical symmetry planes of the medium (Figure 4.16), where θ is the angle between the source polarization and the symmetry axis of the medium. Each of the shear-waves is, in turn, recorded by each of the two receivers, and there is the possibility of a cross-signal, unless the sources and receivers are polarized in the symmetry planes.

In principle, we can find the symmetry axes by linearly combining the four-component shear-wave data to minimize the cross-signal between perpendicularly polarized sources and receivers . If we "synthesize" a source from the real in-line and cross-line sources such that the new synthetic source has the polarization that is either parallel or perpendicular to the symmetry axis, and similarly rotate the geophones, there will be no cross-components recorded. One approach is to solve for θ directly. However, due to the influence of the strong noise that usually companies shear-wave data, a direct

inversion is often unstable. A more robust method is simply to search through a range of angles θ until the cross-signal is minimized.

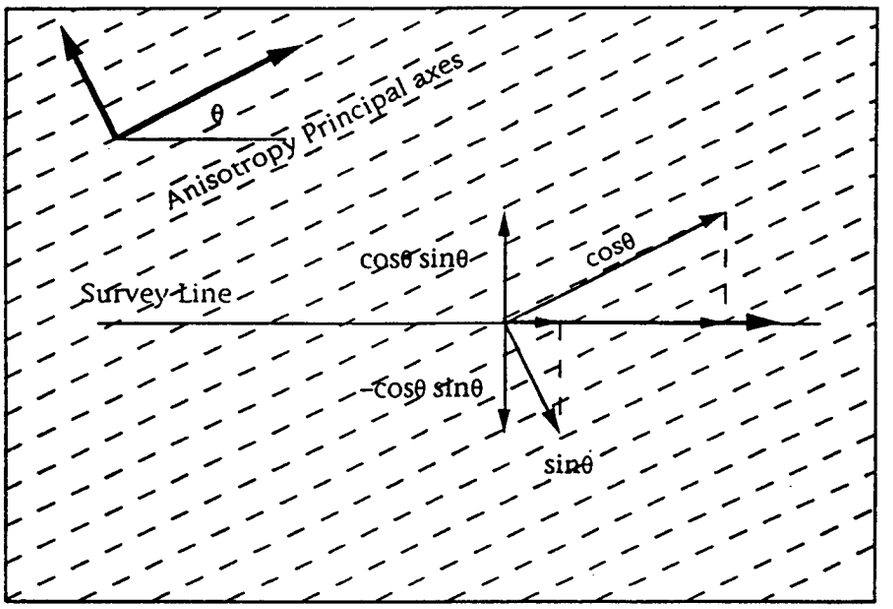

Figure 4.16: Decomposition of shear wave in azimuthal anisotropic medium.

Under a rotation of angle θ, the resulting traces can be computed from the original data in terms of

$$\mathbf{v} = R\begin{pmatrix} u_{11} & u_{12} \\ u_{21} & u_{22} \end{pmatrix}R^{\mathrm{T}}$$

$$= \begin{pmatrix} u_{11}\cos^2\theta + u_{22}\sin^2\theta + & u_{12}\cos^2\theta - u_{21}\sin^2\theta - \\ 0.5\sin 2\theta(u_{12}+u_{21}) & 0.5\sin 2\theta(u_{11}-u_{22}) \\ u_{21}\cos^2\theta - u_{12}\sin^2\theta - & u_{22}\cos^2\theta + u_{11}\sin^2\theta - \\ 0.5\sin 2\theta(u_{11}-u_{22}) & 0.5\sin 2\theta(u_{12}+u_{21}) \end{pmatrix}, \tag{4.1}$$

where u_{11}, u_{12}, u_{21}, and u_{22} are the recorded four-component shear-wave traces, and

$$R = \begin{pmatrix} \cos\theta & \sin\theta \\ -\sin\theta & \cos\theta \end{pmatrix}$$

is the rotation matrix. The appropriate rotation angle will cause the off-diagonal elements of matrix v to vanish. Of course in reality residual noise will always exist and we can not expect the cross-components of the rotated data to be perfectly zero. Only the coherent signals will disappear (or be minimized) after proper rotation.

4.4.7 Rotation Results

After Alford rotation, the processing procedures in Table 4.3 were reapplied and the data set restacked. The rotation was done first in 10 degree increments, and then in 5 degree increments near the proper rotation angle. Stacks with different rotation angles were visually inspected to choose the best angle. Figure 4.17 shows a portion of the stacked four-component data before and after the rotation. Notice that the two cross-components drop below the noise level after proper rotation. Where the events are strong, the rotation angle can be determined within a few degrees; where almost no events are discernible the rotation angle cannot be determined with much confidence.

A problem of multi-component shear-wave analysis is that the symmetry axes of the azimuthal anisotropy may not be the same for all depths. Near-surface layers are often anisotropic, and their anisotropy may be due to weathering or the current stress states that are not related to the fractures thousands of feet deep. Some researchers have suggested that a large part of the observed anisotropy comes from the shallow layers. For VSP data a layer stripping technique can be used to find out the real symmetry axis for each layer. For surface seismic data, the problem is much more difficult, because the geophones must be placed on the ground and the cumulative effects of all the layers are recorded.

We are fortunate that in our survey area the main source of anisotropy seems to come from deeper layers. Figure 4.18 shows part of the S1-S1 and S2-S2 stack sections after rotation. The CDP numbers increase from left to right so that the combined stack section covers a continuous segment of line 2. The transition from S1-S1 to S2-S2 is marked by a vertical line. Notice that the events at 1.5 seconds tie perfectly (marked by arrow a), indicating little or no shallow anisotropy, while there is significant time shift for the events around 4.5 second (arrow b). Actually the amount of time shift varies with depth at that interval associated with our targeted Niobrara and Frontier formation. This result supports the observation from well logs that the Niobrara and Frontier formations are fractured.

Our data processing shows that at any one location a single rotation angle is often enough to eliminate all the cross-component events from shallow to deep layers. This indicates that the symmetry axis of anisotropy does not change much with depth and we don't have to worry about the problem of layer stripping.

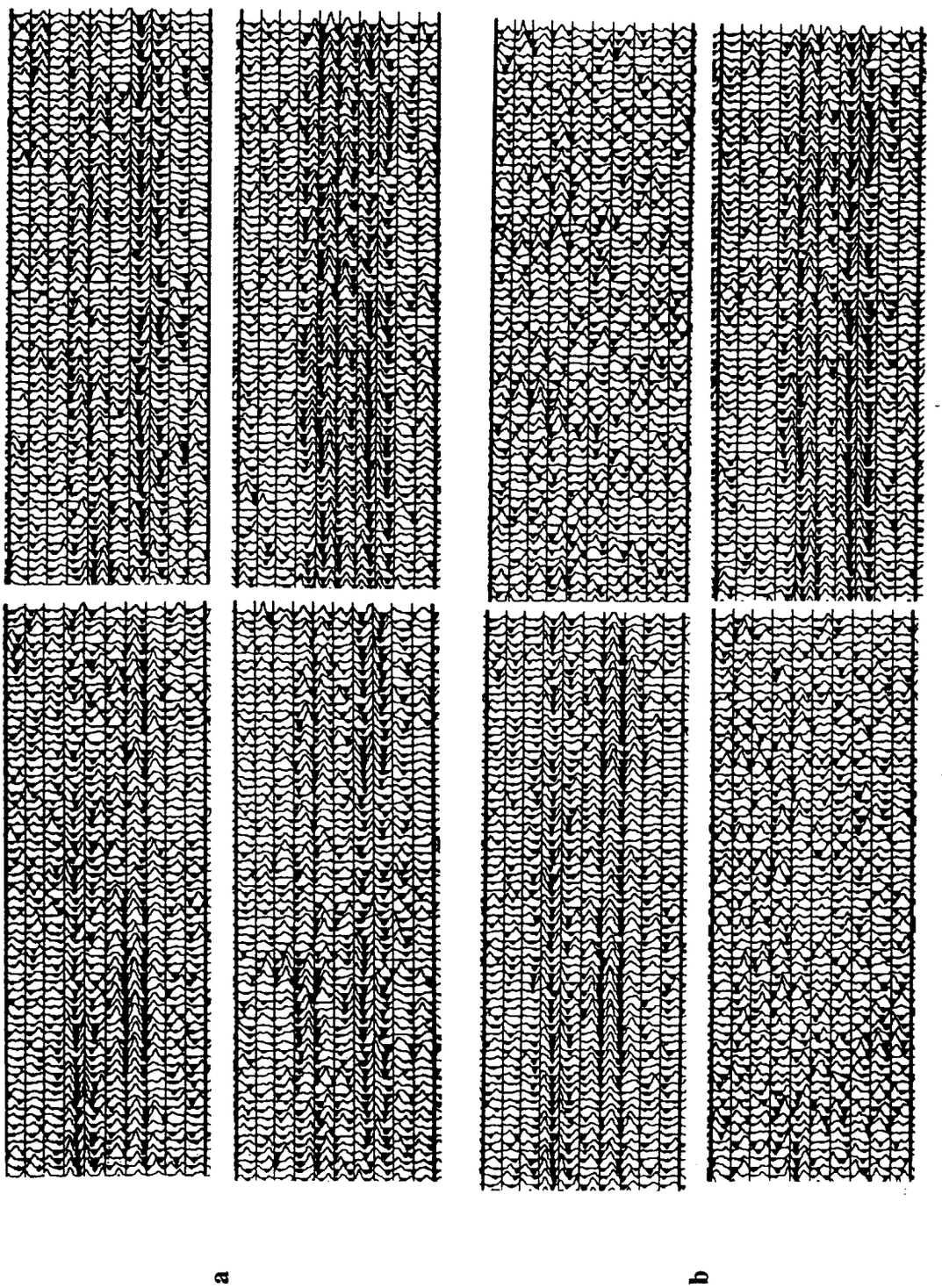

Figure 4.17: Four-component shear-wave stack sections, (a) before Alford rotation, (b) after 20° Alford rotation

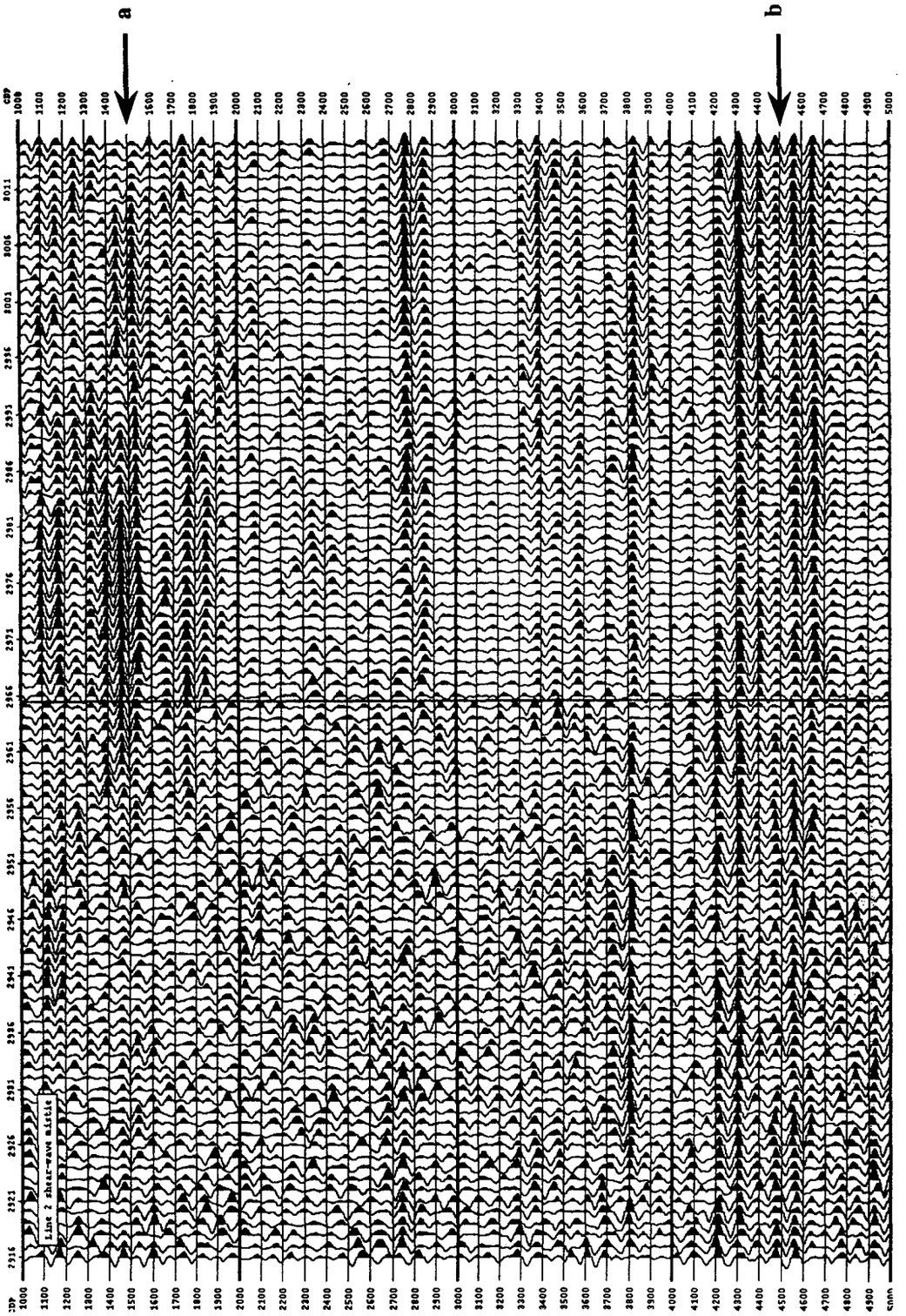

Figure 4.18: Shear-wave misties after Alford rotation. The fast shear wave section is displayed on the left; the slow section, on the right. Events generally tie at 1500 ms (arrow a), but accumulate a mistie by later times (arrow b).

The rotation directions shown in Figure 4.19 are basically consistent for all four lines. A clockwise rotation of about 20° was needed for line 2 to get rid of the cross-components. The rotation angles for lines 1, 3 and 4 were 10°, 20° and 45°, respectively. We have to mention that the data quality of line 1 was especially poor, so that rotation angles can only be determined for the northern half of the line. In the figure, arrows labeled fast indicate the fast shear-wave direction obtained from the rotation. When anisotropy is caused by thin vertical fractures, the fast direction is in the fracture plane. Except for the southern half of line 4, which has ~0° rotation, the fast directions of the survey area are consistently trending northeast.

4.4.8 Traveltime difference

Each of the two orthogonally polarized shear-wave modes has its own velocity in an anisotropic medium, resulting in different travel times for the same event in the corresponding stacked section. A large travel time difference, which is related to strong anisotropy, is used as an indicator of high fracture density.

We estimated the travel time difference as a function of space and time using the cross correlation $C(\tau)$ of the rotated fast and slow traces $S_{11}(t)$ and $S_{22}(t)$ within a moving time window (t_1, t_2),

$$C(\tau) = \frac{\sum_{t=t_1}^{t_2} S_{11}(t) S_{22}(t+\tau)}{\sqrt{\left(\sum_{t=t_1}^{t_2} S_{11}^2(t)\right)\left(\sum_{t=t_1}^{t_2} S_{22}^2(t)\right)}}, \qquad 0 \le \tau \le \tau_{max}, \tag{4.2}$$

where τ is the time shift and τ_{max} is the maximum amount of shift allowed. We set τ_{max} to be 90 msec, because that is roughly the temporal period of the data. The value of τ at which $C(\tau)$ achieves its maximum is defined to be the travel time difference at the center of the time window.

We use a sliding window to compute the time shift at each depth. The result for line 2 is shown in Figure 4.20. In spite of the fluctuations, we can see the regions where the time shifts are large, and that deeper layers have larger time shifts. The maximum value of the cross correlation indicates the similarity between the two rotated shear-wave components. They can be used to represent the reliability of the time shift results.

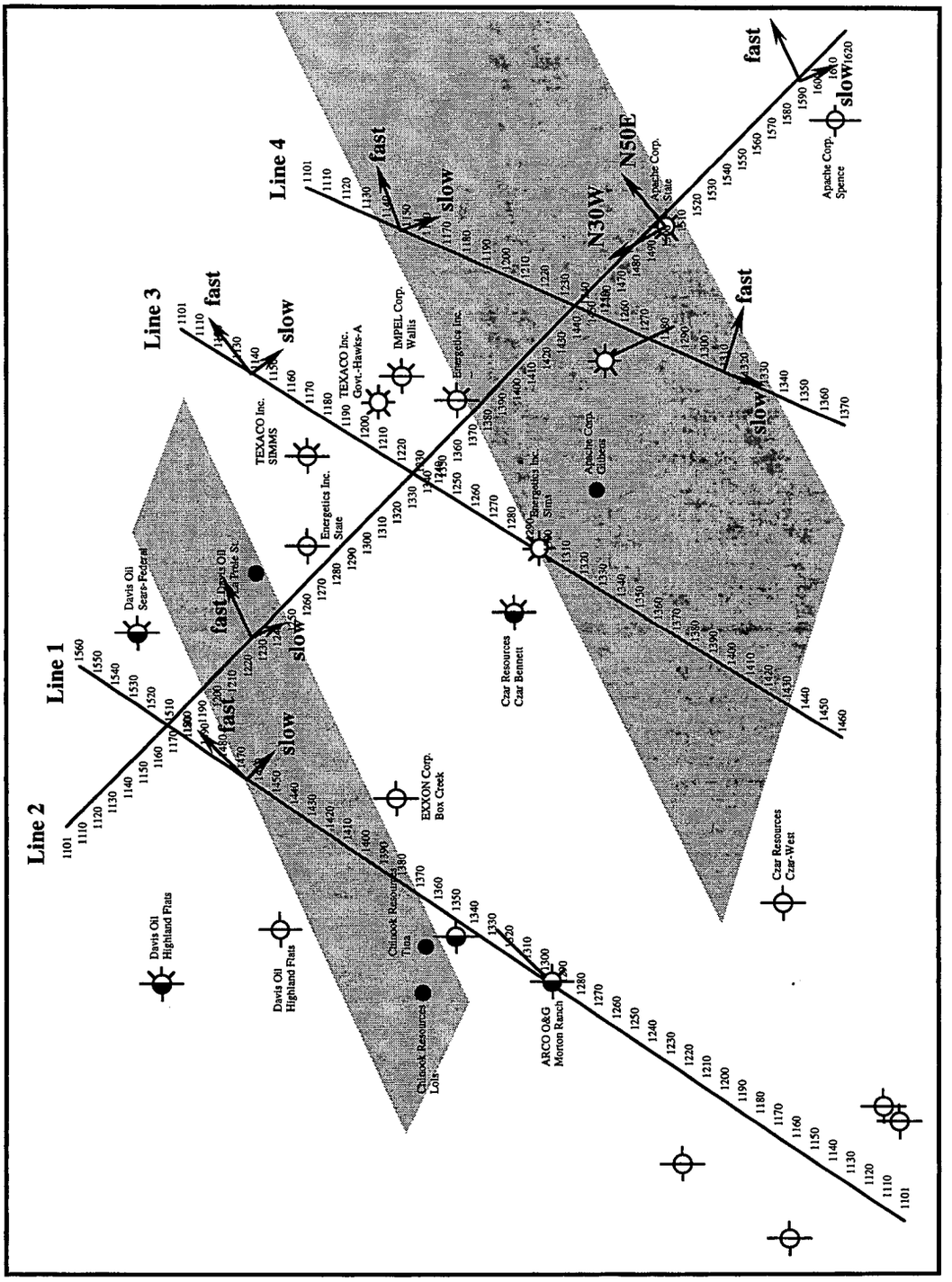

Figure 4.19: The result of four-component shear-wave processing.

The amount of shear-wave splitting varies laterally along the lines, as might be expected. If we use a very large time window, the time shift can be viewed as the average of the whole trace. Figure 4.20 shows the result for a section on line 2 where signals are best. It changes smoothly between a few msec to 40 msec. Figure 4.21 shows the actual stack section. It is plotted using alternating fast and slow traces so that the amount of travel time difference can be easily seen at the boundaries. From Figure 4.21 we can estimate the amount of anisotropy in the Niobrara-Frontier formations. Around 4.2 seconds, for a sequence of events of about 300 msec, the travel time difference increases by 10-20 msec, thus the amount of anisotropy is about 3-7%.

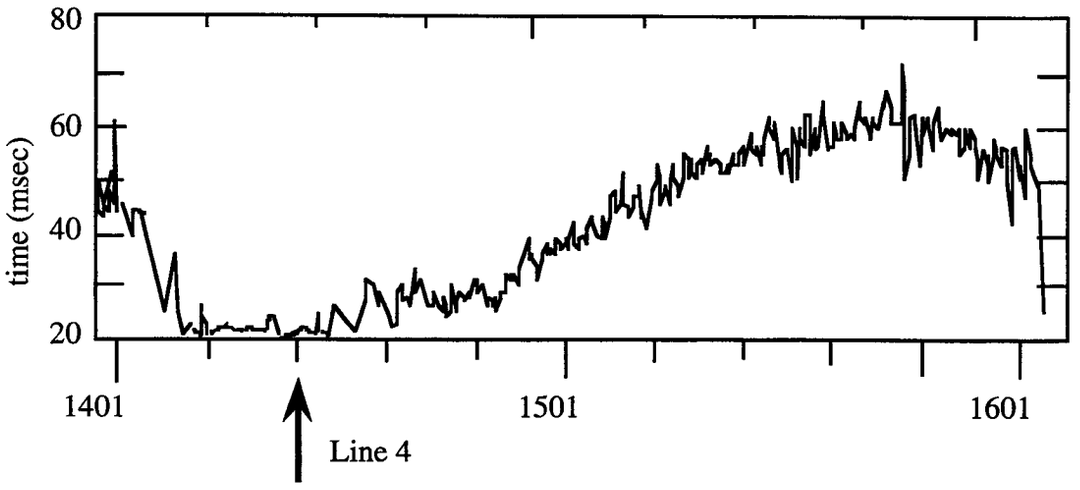

Figure 4.20: Whole trace traveltime difference between the fast and slow shear-wave stack sections of line 2.

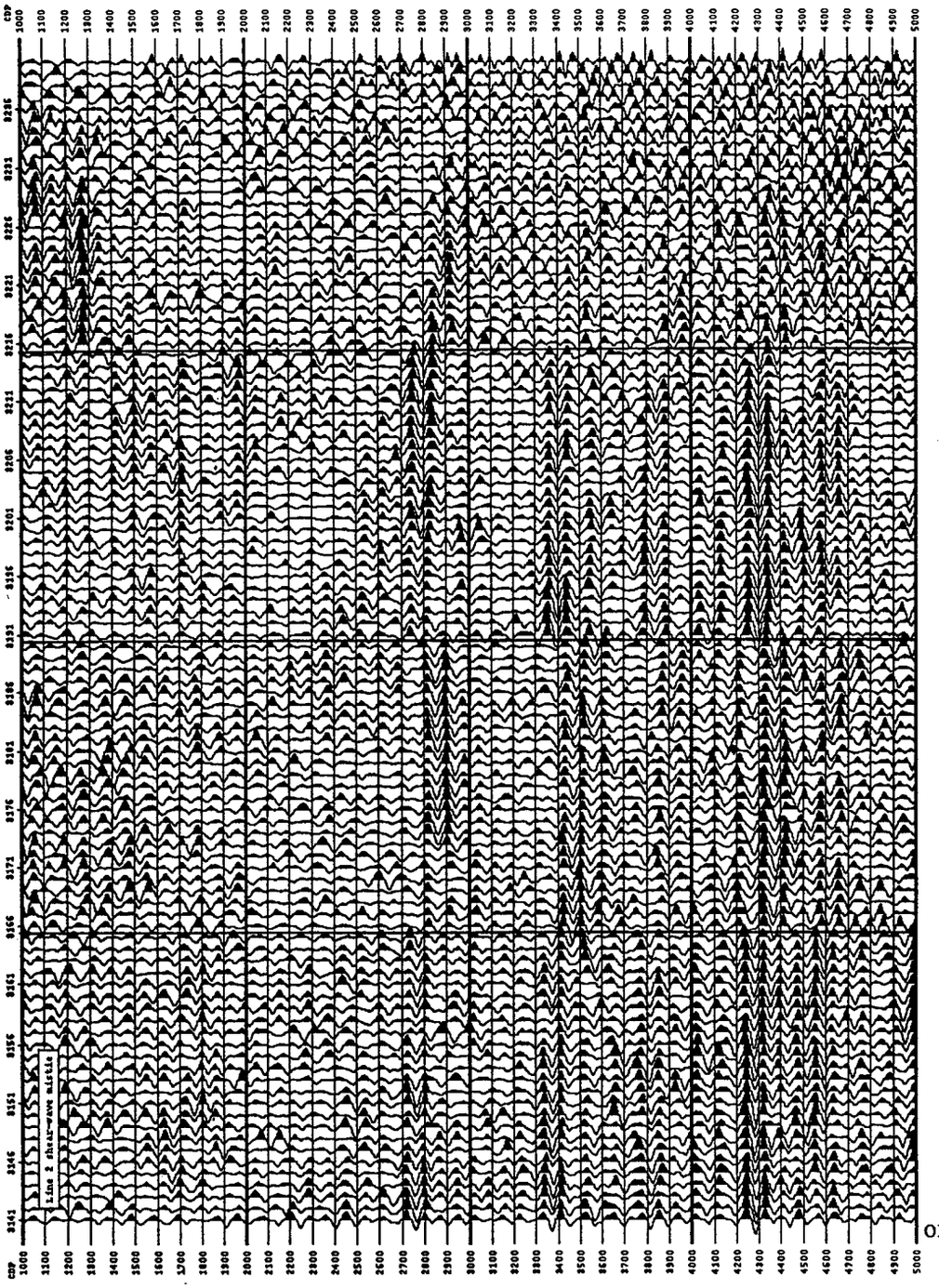

Figure 4.21: Alternating fast and slow shear-wave stacks showing the change of traveltime difference along line 2.

4.4.9 Fracture model for the survey area

Analysis of the shear-wave data, plus subsurface well control, allows us to construct a fracture model for our survey area (Figure 4.19). This model was largely developed by Melinda Gale of Vastar Resources and Mike Mueller of Amoco, and was reported at the 1994 Society of Exploration Geophysicists meeting in Los Angeles.

Throughout the site, the fracture *directions*, inferred from the shear-wave rotation analysis on all four lines, trend consistently SW-NE – all generally within about 20° of each other. These trends were taken to be equal to the polarization direction of the fast shear wave after rotation. These directions are labeled on the figure in a few locations with arrows.

The fracture *intensity* was taken to be proportional to relative time difference between the fast and slow shear waves at each location. This travel time difference (inferred fracture intensity) is highly variable throughout the site – the corresponding shear-wave anisotropy in the Frontier-Niobrara zones ranges from near zero to as much as 7 percent. The regions of largest anisotropy along the four lines can be interpreted with two localized zones of relatively intense fracturing (shown in gray in Figure 4.19).

Before beginning the survey, it was suggested that the fractures at depth would trend more along a NW-SE direction, parallel to the strike of the Casper Arch and the associated flexure along the SW edge of the survey (Figure B.1, Appendix B). These were also interpreted from the second derivative of the known structure at depth. This trend is also seen in surface fractures mapped some km to the south of the survey area (Mueller, pers. comm.). The Amoco-Arco Morton Ranch well was drilled near the midpoint of survey line 1 and completed right before our seismic survey. Based on this pre-survey interpretation, the well went horizontal in the Niobrara-Frontier interval and trended northeast (almost parallel to line 1), aiming to intersect a maximum number of fractures perpendicular to their trends. In fact, it was observed down-hole that it trended within about 20° of the fracture trend, consistent with the interpretation in Figure 4.19. The initial test production at Morton Ranch was quite promising with 165 BOPD, 380 MCFGPD. However, the productivity decreased quickly to about 16 BOPD and 70 MCFGPD (Figure 4.22). The result of this well suggest that, first of all the fractures may have different orientation, thus the horizontal well did not intersect many of them, and secondly, the fractures may be closed because of the loss of pore pressure due to production – consistent with poor fracture connectivity and low fracture density.

The Arco (Vastar Res.) and Amoco Red Mountain 1-H well was drilled near the intersection of line 2 and line 4 after the seismic study, using the interpretation essentially

summarized in Figure 4.19. The total depth was reached on December 30, 1993. Inside the Frontier formation at about 11,511 feet TVD (true vertical depth) the well went horizontal for about 1,100 feet trending southeast. The well was reported hitting numerous fractures, consistent with the fracture model, and the test production on July 18, 1994 showed 1068 MCFGPD, 32BOPD and only 3 barrels of water per day. The initial result demonstrated once again the effectiveness of the four-component shear-wave method developed by Alford (1986). Since the well is fairly new, much information is still not available and this result is only preliminary.

A number of older vertical wells tend to confirm the fracture model. For example the Chinook Lois, Apache Githens, and Energetics Simms wells (Table B.2, Appendix B) all lie within the fracture zones (gray in Figure 4.19) and all have shown reasonable production. A few others outside of the interpreted fracture zones performed much worse.

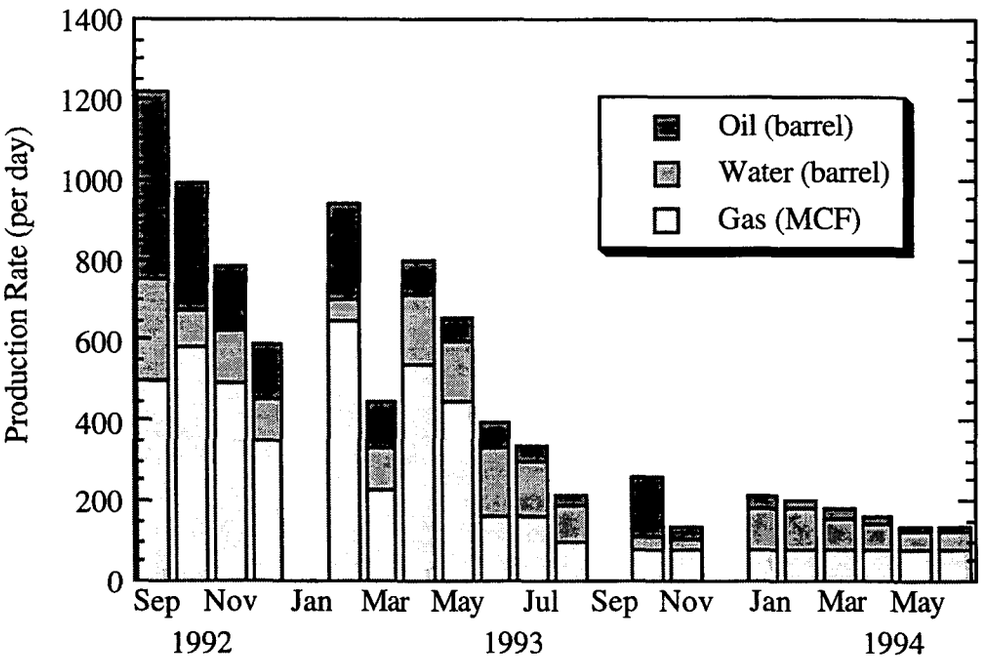

Figure 4.22: Production history of the Amoco-Arco Morton Ranch well.

4.5 P-wave data

P-wave data have traditionally been used to map underground structures. Travel time is usually the only information used to study reservoirs. However, since the early 1980s, people have been trying to use amplitude and amplitude-versus-offset (AVO) information as a hydrocarbon indicator (Ostrander, 1983, 1984; Sengupta, 1987; Blangy, 1992), because AVO can be quite sensitive to Poisson's ratio. In recent years several papers have been published on the effects of anisotropy on AVO (Wright, 1987; Pelissier et al. 1991; Mallick and Frazer, 1991; Blangy, 1994). The results suggest the possibility of using P-wave data (azimuthal AVO and azimuthal stacking velocity) to study anisotropy.

Lower cost is the primary benefit of using P-wave data instead of traditional four-component shear-wave data. Collecting shear-wave data requires special sources and geophones, more time for ground work, and at least twice the amount of shooting time. The data volume can be six times that of P-wave data because shear-wave data require four components and longer travel time. Additional difficulties with shear waves come from low signal-to-noise ratio, serious ground-roll contamination, tougher statics problems, and more processing time. At the same time, 3D seismic methods are becoming more and more routine. Useful information such as amplitude, azimuthal variation of AVO and stacking velocity, and frequency has not been adequately exploited. Our data processing emphasizes P-wave attributes and tried to relate them to anisotropy, and ultimately to natural fractures.

4.5.1 Velocity analysis

For compressional wave data (P-P), the CDP location of a trace is the midpoint between the shot and receiver, which we number as the sum of the source station number and receiver station number. The first station of a line is always numbered 1101, and the CDP numbers are 2202 to 3018 for line 1, 2200 to 3243 for line 2, 2202 to 2920 for line 3, and 2202 to 2742 for line 4. The average fold is about 70 and the distance between adjacent CDP stations is 15 meters (50 feet).

After demultiplexing the traces and loading geometry information into trace headers, we applied a gain correction to each trace of the data set. The reason is that when we recorded the data in the field, some of the recording boxes malfunctioned and applied only one-sixteenth of the normal gain to the traces. (This problem was discovered by Amoco after the acquisition had been finished.) This correction is essential for all detailed amplitude-sensitive processing, such as AVO analysis.

Elevation statics and refraction statics were applied afterward. For elevation statics, the final datum elevation is 4,500 feet and the replacement velocity is 6,500 feet/sec. The refraction statics solution was provided by M. Mueller of Amoco. The values range from -130 to -220 msec.

In the first phase of data processing, we concentrated mainly on stacking velocity analysis. For this stage, automatic gain control (AGC) with an operator gate length of 1,000 msec was applied to balance the traces, which of course destroyed the true amplitude information at the same time. Velocity analysis was done in three passes. In the first pass, velocity functions were determined interactively about every 30 CDPs, using ProMAX's interactive velocity analysis tool. The quality was controlled by both the semblance and the quality of the stacked section near the velocity functions. In the second pass, we slightly changed the velocity function (±3%, ±6%) and re-examined the stack. A small adjustment was made to the velocity functions. Finally, we visually inspected the NMO corrected data at every 10 CDP stations, and used the resulting velocity function in all the final stacks. At the end of each pass, we computed the residual statics and applied the correction to the dataset.

In the next phase, minimum phase spiking deconvolution with a 100 msec operator over a gate 1.5 to 2.6 sec was applied to the dataset corrected for field statics. AGC was used to balance the traces. We did NMO corrections with the final stacking velocity and computed the residual statics by maximum power autostatics methods over time gate 1.8 to 2.5 seconds. The final stack was made by applying the residual statics and then computing the mean traces of the CDP gathers. A 6/12.5-50/60 bandpass filter was applied to the final stack.

The processing steps for compressional wave (P-P) are summarized in table 4.4.

4.5.2 Amplitude analysis

It is much more difficult to obtain true-amplitude stacks because of the strong noise, both random and coherent. The noise tends to be amplified disproportionally by spherical divergence amplitude correction, deconvolution, and inelastic Q compensation. To kill the especially noisy traces, we carried out careful trace editing, we then corrected the cleaned dataset for spherical divergence using 1/distance and for attenuation using 100 as the value of Q.

Inequality of source strength and geophone-ground coupling is another concern when performing true-amplitude processing. Our goal is to determine the true reflectivity, its lateral variation along the survey line, and its dependency on offset. The lateral reflectivity variation may be obscured by the uneven source strength, and the AVO trend

can be lost in the uneven geophone-ground coupling. Surface consistent methods attempt to address this problem (Taner and Koehler, 1981). Ideally, a trace is the convolution of the source signal, the earth filter, the reflection coefficient, and the geophone response, with noise in all these terms. The power of a trace is therefore the multiplication of the power (or gain) of these individual terms. This relation can be linearized by taking the logarithm

$$\log T_{ij} = \log S_i + \log G_j + \log R_{i+j} + \log O_{j-i} + \cdots, \tag{4.3}$$

where T_{ij} is the power of the trace with source i and receiver j, S_i is the energy level of source i, G_j is the strength of the coupling of geophone j with the ground, R_{i+j} is the contribution of reflectivity at CDP station i+j, and O_{j-i} is the offset term (or radiation pattern) for offset j-i. T_{ij} is measured from the seismic traces, and the unknowns are S_i, G_j, R_{i+j} and O_{j-i}. Usually the number of traces is much larger than the number of unknowns. For example, for line 2 there are 261 shots (S_i's), 522 receivers (G_js), 1042 CDP's (R_{i+j}'s), and 480 offset terms (O_{j-i}'s), thus about 2300 unknowns; there are, however, 62,640 seismic traces, which give us a largely over-determined linear system. Standard least-squares methods can be used to solve this problem.

Table 4.4: Processing sequence of P-wave data.

Demultiplex: channels 2-241
Geometry installation
Elevation statics: datum elevation 4500 feet, velocity 6500 feet/sec
Refraction statics
Spherical divergence correction, 1/distance
Attenuation compensation, Q = 100
Spiking deconvolution, operator length = 100 msec, window 1.5-2.6 seconds
CDP sort
Velocity analysis, multiple passes
Surface-consistent amplitude analysis or AGC with operator length 1000 msec
NMO correction
Maximum power autostatics, window 1.8 - 2.5 seconds
Final stacks, both with AGC-corrected amplitude and preserved amplitude
Band-pass filter 6/12.5--50/60 Hz
Migration, stacking velocity

Figure 4.23 shows the source and receiver solutions for two events on line 2. We used as T_{ij}'s the RMS amplitudes within small time windows (about 80 msec) containing the events at 1.9 and 2.5 seconds. Because of the phase change and random noise, the peak amplitude is quite unstable compared to the RMS amplitude, which is considered a better representation of the energy level of events.

Ideally, the source and receiver solutions should be unique for each dataset. They should not depend on the selection of the time window used to compute the trace power, as long as the time window captures the same event for all the traces. We computed the solution twice using different events, the shallower one at 1.9 seconds and the deeper one at 2.6 seconds (Figure 4.23). The similarity between the solutions is an indication of the quality of the solutions themselves. As shown in figure 4.23 (a) and (b), indeed they agree very well. The confidence of the solutions, measured by the distribution of the residuals, is shown in Figure 4.23 (c) and (d). Most of them are above 0.95, with 1 meaning that the solution is perfect.

The source and receiver solutions of the surface consistent amplitude analysis were applied back to the data set to correct for the unevenness of source strength and receiver coupling along each line. All subsequent analysis of AVO trends and lateral amplitude variations were made on this corrected data set, as were the final stacks with preserved amplitude (true amplitude stacks).

We have observed striking amplitude variation in the final true amplitude stacks. Figure 4.24 shows a stacked section of line 3. CDP numbers increase from left to right, corresponding to the line direction from northwest to southeast. Notice the event marked by arrow. The amplitude there is significantly larger than elsewhere along the line, while there is no such amplitude contrast along the shallower event.

To get a global picture, we extracted the peak amplitude of the same event from both line 2 and line 3. A 5-trace mix was applied to the final stack to improve the signal to noise ratio. The results are plotted in Figure 4.25. It is evident that there exists a region of extraordinarily high P-wave reflectivity (bright spot) at the intersection of the two lines (CDP 2600 - 2850 on line 2 and CDP 2420 - 2750 on line 3), indicating a large change in acoustic impedance, which may be the result of gas.

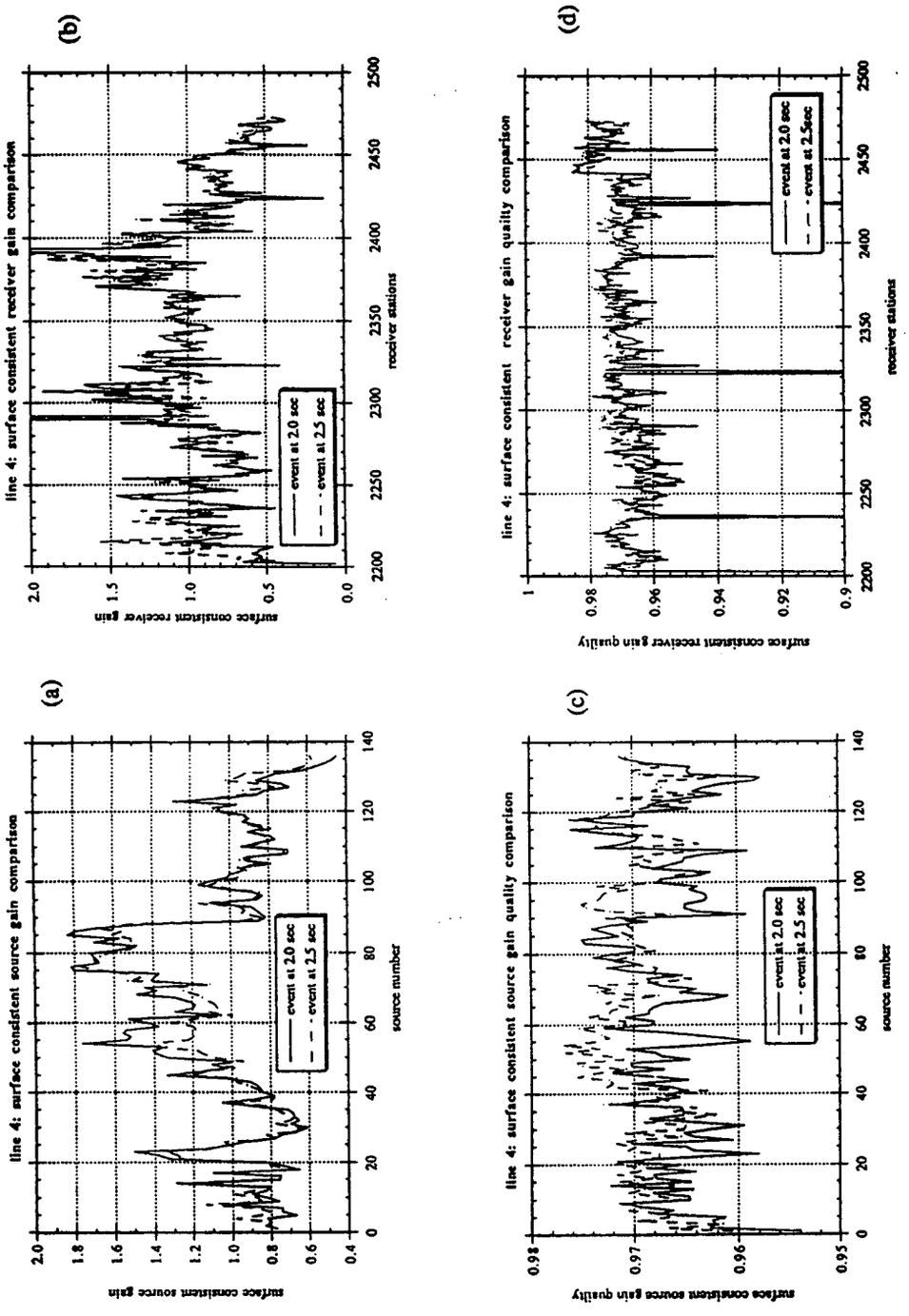

Figure 4.23: Source and receiver solutions of the surface consistent amplitude analysis. The solid and dashed lines are for the solution based on the events at 1.9 and 2.5 seconds, respectively. (a) source solutions, (b) receiver solutions, (c) quality of the source solutions, (d) quality of the receiver solutions.

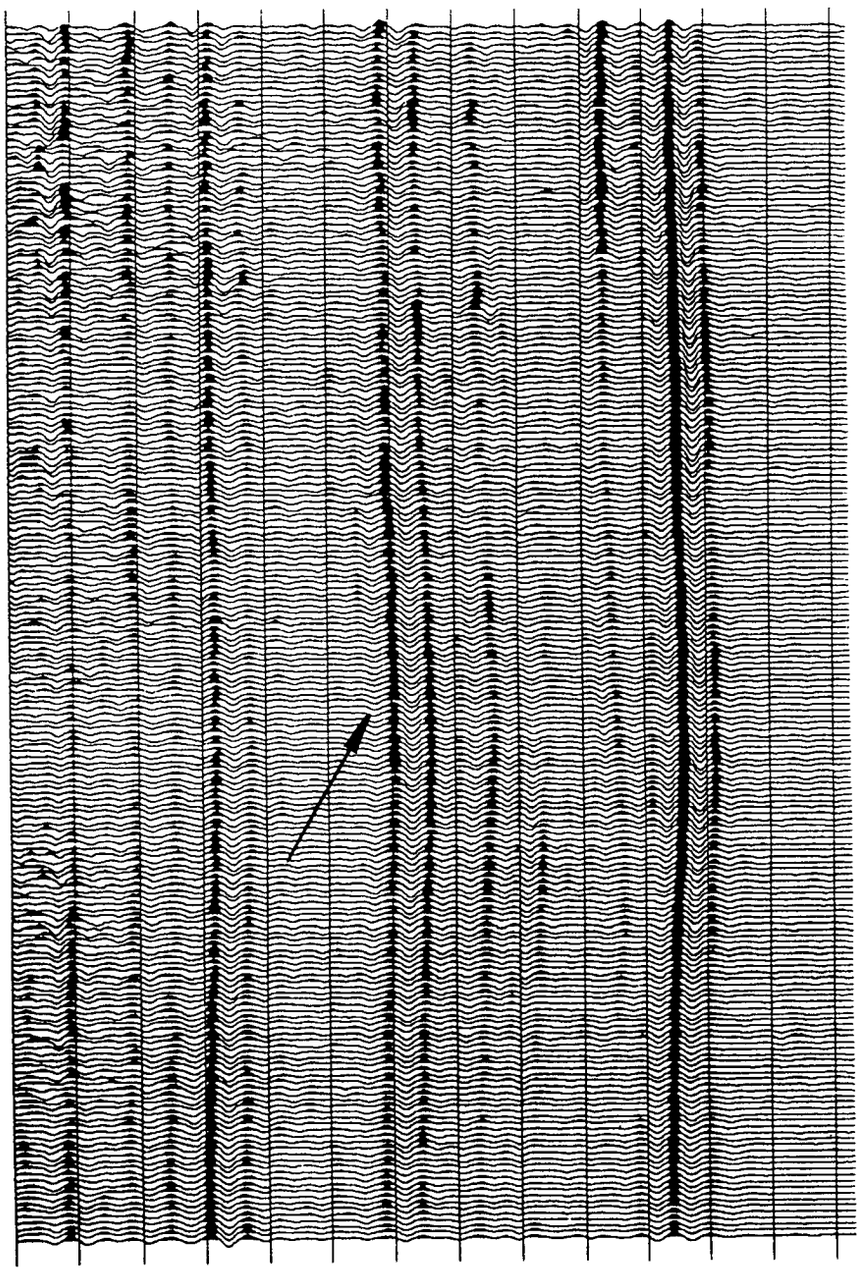

Figure 4.24: True amplitude stack of line 3. Notice the striking amplitude variation of the marked event.

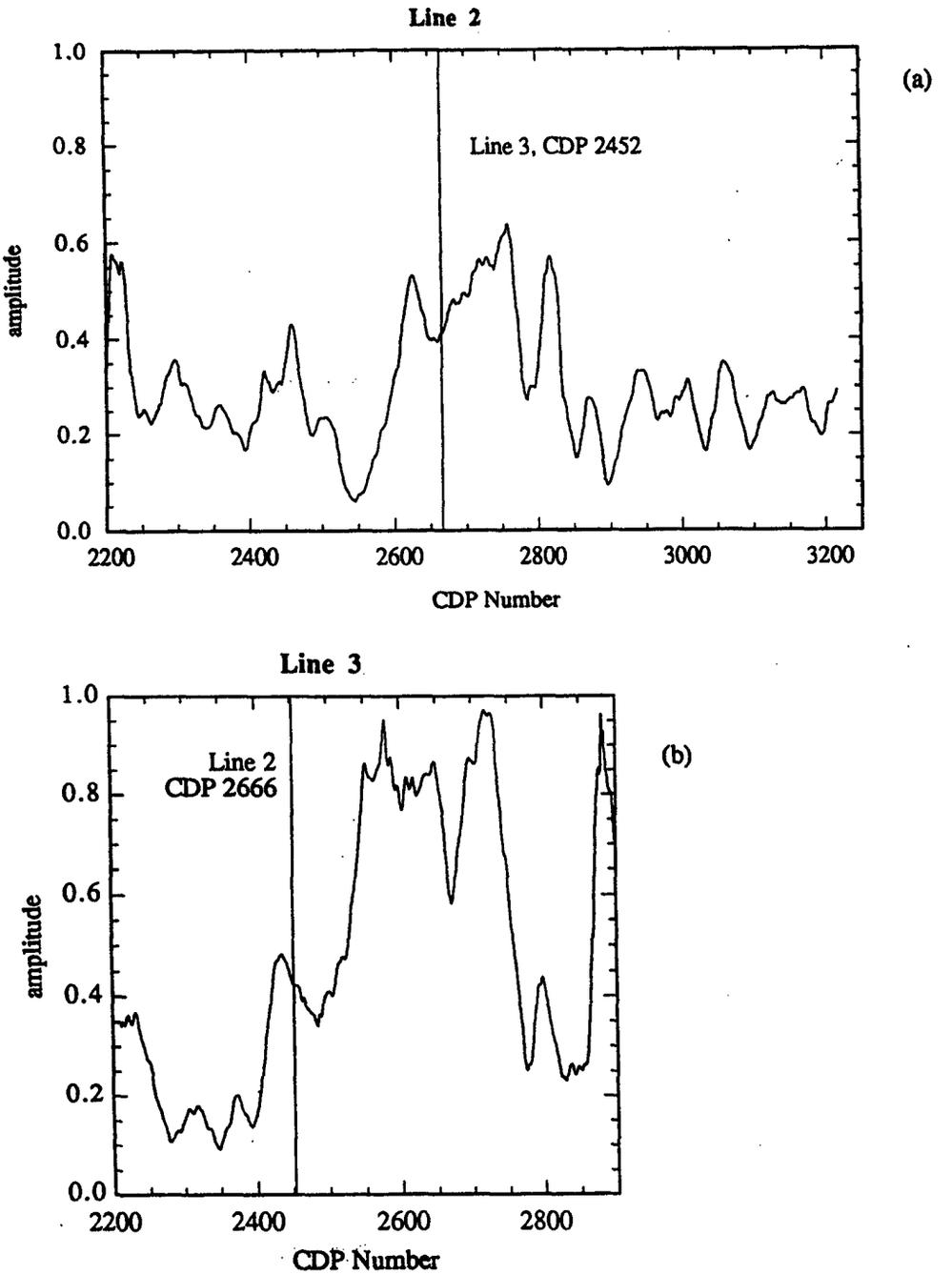

Figure 4.25: Peak amplitudes of the marked event in Figure 4.24. (a) Amplitudes obtained from line 2, (b) amplitudes for the same event from line 3.

4.5.3 Stacking chart display of amplitude

There are two technical problems with amplitude analysis that we have tried to solve efficiently: (1) it is difficult to visualize the lateral variation of reflectivity and AVO trend along a survey line, and (2) it is time-consuming to identify interesting areas for detailed study. Our solution is a stacking-chart display of the amplitudes (Figure 4.26). In Figure 4.26, the horizontal axis shows the geophone station numbers, and the vertical axis shows the source station numbers, just like a regular stacking chart. In this type of plot a horizontal line represents all of the traces in a single shot gather, and a vertical line represents a common receiver gather. The traces of a common offset gather are aligned on a 45° line from lower left to upper right. And finally, the CDP gathers are on the 45° lines from upper left to lower right.

We first ran a 5-trace mix on the shot gathers and then computed the RMS amplitudes of the traces. The time window on the trace where the amplitude is estimated is about 100 msec wide and is centered at 2.5 sec. In Figure 4.26, the RMS amplitude of a trace segment on line 2 is plotted at the location determined by the source and receiver numbers of that trace. Because there are fewer shots than geophone stations, linear interpolation was used to fill the blanks where no data were available.

Several patterns are evident. For example, the signals are much stronger on the northwest half of line 2 (stations 1101 to 1380). This appears to be CDP-consistent, which means it is probably due to subsurface effects. Notice, however, that the horizontal shot-consistent pattern near shot station number 1400 is an artifact of interpolation. There are no real data there.

There are a few distinct AVO trends shown in Figure 4.26. At CDP 2666, the reflection amplitude is very strong and relatively flat with offset. At CDP 2816, the signals are extraordinarily weak at all offsets. The corresponding CDP gather shows that there is almost no observable event. At CDP 2928, however, as offset increases, the reflector amplitude drops gradually, increases sharply and then drops again. At CDP 3004, the amplitude stays high until about 10000 feet. In addition, there also exist local high reflectivity zones (CDP 3004) and low reflectivity zones (CDP 3120).

4.5.4 Center frequencies of pre-stack data

The effect of fractures on acoustic velocity and attenuation has been studied both theoretically and experimentally by many authors (Hudson, 1981, 1991; Crampin, 1978, 1984; Mavko and Nur, 1979; Mukerji & Mavko, 1994). In general fractured rocks have higher attenuation because of the scattering effects of the cracks and the fluid-related

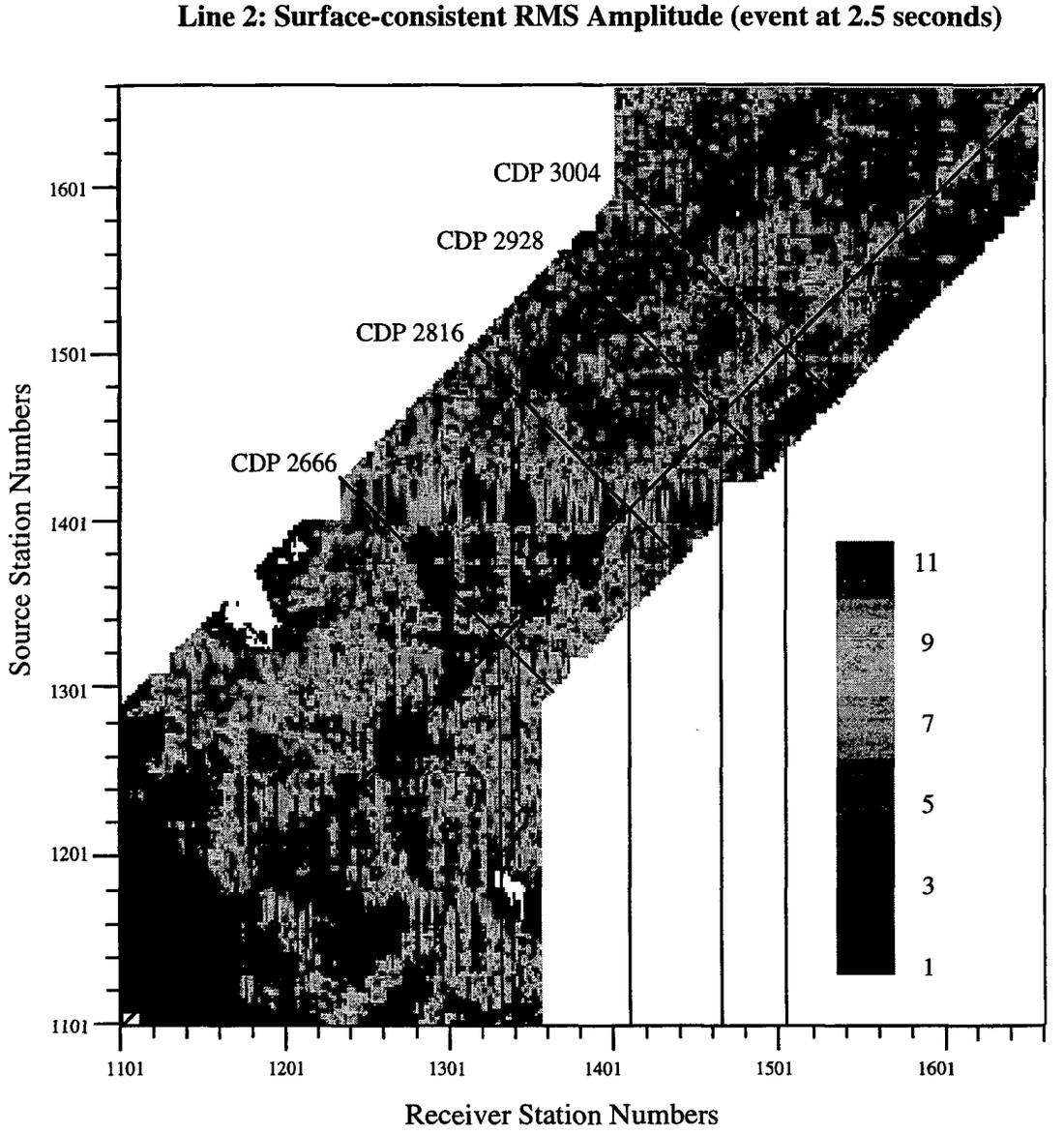

Figure 4.26: Stacking chart display of the RMS amplitudes of the event at 2.2 seconds on line 2. CDP number for any trace is the sum of the source and receiver numbers.

dissipation between the crack surfaces. When waves pass through a highly fractured zone, high frequency components tend to have a greater loss than low frequency ones. The shape of the power spectrum of the seismic traces can be used as an attribute in our search for fractures by identifying high attenuation zones.

We compute the so-called "center frequency" or "center of gravity" of the power spectrum of the pre-stack P-wave data. It is an indication of relative changes in the high frequency components of the power spectrum. The algorithm is as follows. We first resample the final stack using 1 msec sample rate. Resampling is done solely for computational reasons. It allows us to use a time grid independent of the original sampling rate. Then we extract a small sequence of data at a certain depth with a tapered window. The power spectrum $p(f)$ of the sequence is computed using a fast Fourier transform and finally the center frequency f_c is calculated using

$$f_c = \left[\frac{\sum_0^{f_N} f_i^n p(f_i)}{\sum_0^{f_N} p(f_i)} \right]^{\frac{1}{n}}, \tag{4.4}$$

where f_N is the Nyquist frequency and n is an arbitrary constant. In our computation we chose it to be 1, which means that f_N is actually the first moment. Finally we corrected the results for surface-consistent effects and plotted them in a stacking-chart display.

There is always a tradeoff between the temporal resolution and the spectral resolution. If we chose a shorter time series, the time (depth) associated with the center frequency can be determined more accurately, but the uncertainty of the center frequency itself will increase accordingly. A longer time window, on the other hand, means a better frequency estimation, but greater time uncertainty.

Figure 4.27 shows a stacking chart display of center frequencies of the traces of line 2. The length of the time window was 256 msec, approximately corresponding to a sampling rate of 2Hz/sample in the frequency domain. The computation was repeated every 20 msec from 500 to 3,000 msec. In the plot the horizontal axis indicates geophone station numbers, and the vertical axis indicates source station numbers. Dark color means high center frequency (or low attenuation) and white color means low center frequency (high attenuation). Several low frequency zones are marked by arrows. They appear to roughly coincide with the locations along line 2, intersected by the fracture zones shown in Figure 4.19. This is suggests a possible link between low signal frequency (high attenuation) and fracture occurrence.

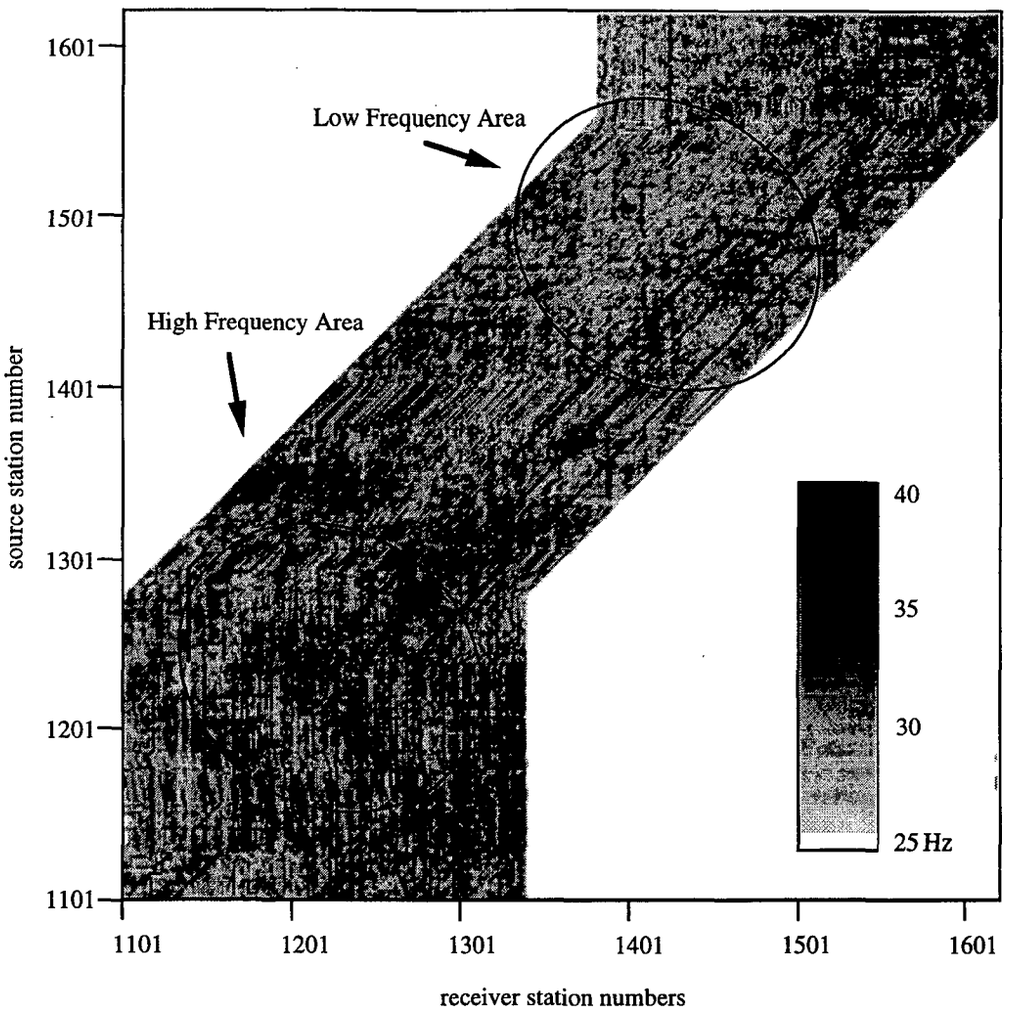

Figure 4.27: Surface-consistent corrected center frequencies of line 2. The length of the time window is 256 msec.

4.5.5 Possible evidence of P-wave anisotropy

The intersection of line 1 and line 2 is very interesting, because it is located within a high density fracture zone (Figure 4.19) and a strong P-SH anomalous zone. The intersection is at CDP 3018 on line 1 and CDP 2340 on line 2. The two lines are approximately perpendicular to each other.

To get a more stable look at amplitudes at the intersection we formed supergathers in each line from 9 adjacent CDP gathers centered on the intersection. Surface-consistent amplitude correction has been applied to all CDP gathers. Then we computed the RMS amplitude of each trace for the event at 2.2 sec on both lines. The time window length is 100 msec. The results are plotted in Figure 4.28 In the direction of line 1, the amplitude stays roughly the same from near to medium offset, and increases suddenly at far offset (Figure 4.28 (a)). In the direction of line 2, the amplitude increases gradually (Figure 4.28 (b)). (The cyclic increases and decreases are probably due to coherent noise.) The NMO corrected CDP gathers are also shown in Figure 4.28 (c) and (d). The different AVO trends suggest that anisotropy can be observed in conventional compressional wave data.

Figure 4.29 shows P-wave CDP gathers, recorded at the same midpoint but on the orthogonal trending lines 2 (CDP 2666) and 3 (CDP 2452). Both are moved out with the same stacking velocity, which is chosen to best flatten CDP 2666, but it leaves CDP 2452 overcorrected. This indicates a faster P-wave stacking velocity along line 3 than along line 2 at their point of intersection. The fractures are more nearly parallel with line 3 than line 2, consistent with this azimuthal variation in P-wave velocities.

For a rough quantitative estimation of the amount of anisotropy, let us say that the NMO over-correction is about 20 milliseconds for an incident angle of 25 degrees, and the velocity anisotropy occurs within a period of 700-millisecond P-wave traveltime. Using the results in chapter 3, we conclude that the equivalent shear anisotropy is about 8 percent.

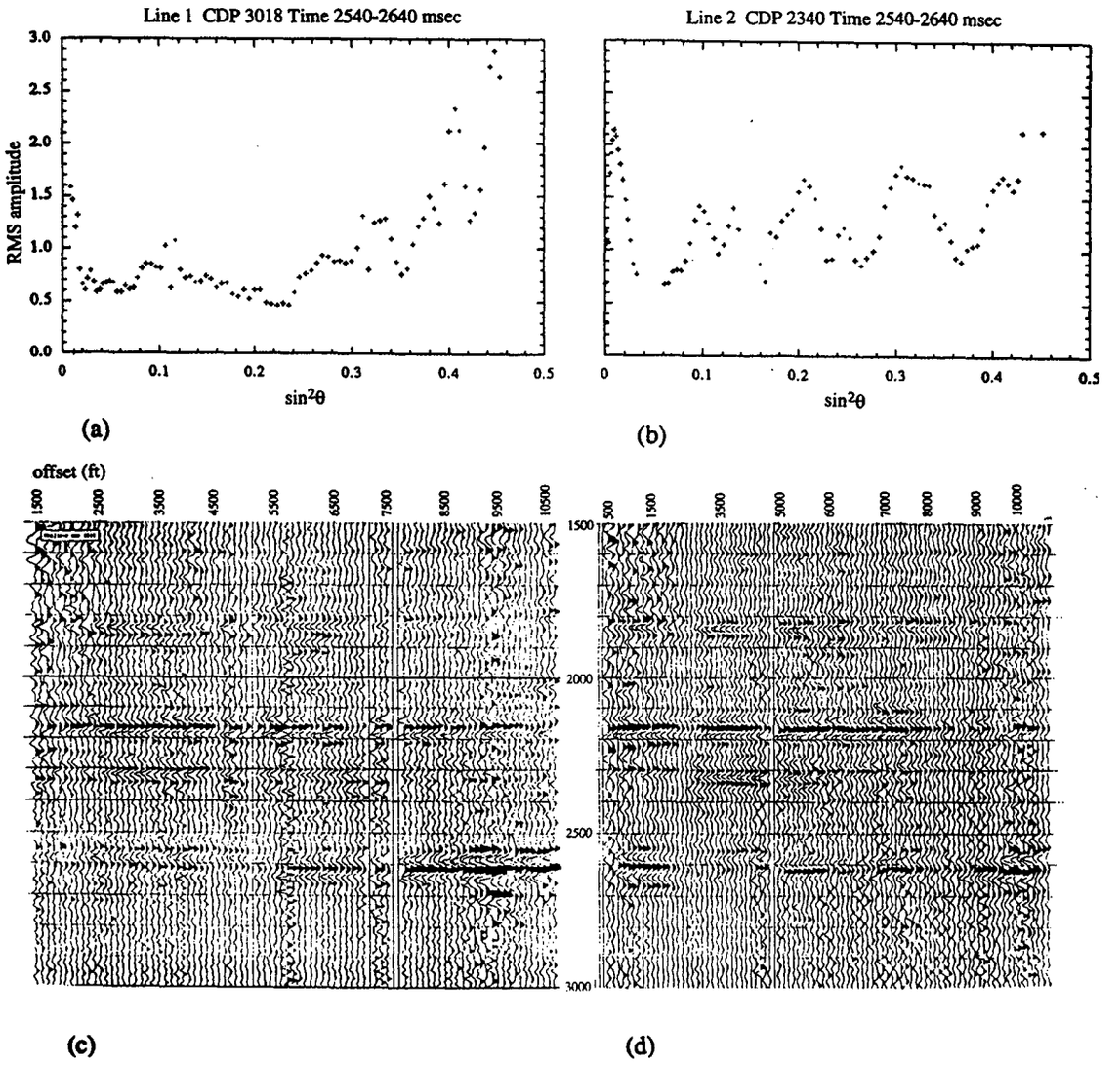

Figure 4.28: AVO trends obtained at the same midpoint on orthogonally trending lines 1 (CDP 3018) and 2 (CDP 2340). (a) AVO trend in the direction of line 1 (θ is angle of incidence), (b) AVO trend in the direction of line 2, (c) NMO corrected CDP gather on line 1, (d) NMO corrected CDP gather on line 2.

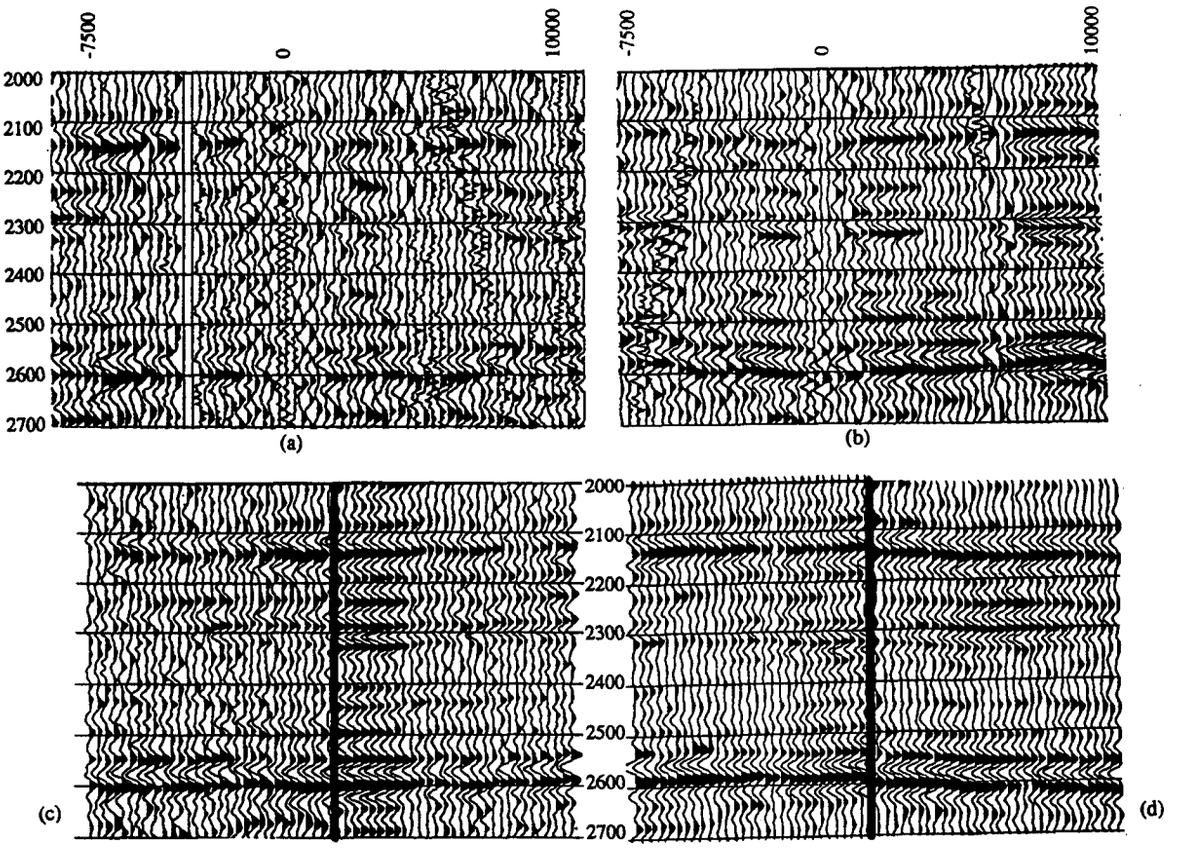

Figure 4.29: CDP gathers at the same midpoint but on orthogonally trending lines 2 (CDP 2666) and 3 (CDP 2452). Both are moved out with the same stacking velocity. (a) CDP gather on line 2, (b) CDP gather on line 3, (c) tie of events on near offset stacks, (d) tie of events on far offset stacks.

4.6 Conclusions

With the generous help and expertise of our partners at Amoco and Arco/Vastar Resources, we successfully acquired and processed nearly 50 km of 2-D, 9-component reflection data over a fractured site in the Powder River basin of Wyoming. The S-wave data were of moderately good quality, allowing us to develop a fracture model for the site by combining shear wave splitting rotation analysis with well control. The P-wave data were of very good quality, allowing us to see lateral variations in reflectivity, AVO response, and frequency content (attenuation) as well as some evidence for azimuthally dependent AVO and P-wave stacking velocities.

Throughout the site, the fracture directions, inferred from the shear-wave rotation analysis on all four lines, trend consistently SW-NE — all generally within about 20° of each other. These trends were taken to be equal to the polarization direction of the fast shear wave after rotation. The fracture intensity was taken to be proportional to relative time difference between the fast and slow shear waves at each location. This travel time difference (inferred fracture intensity) is highly variable throughout the site – the corresponding shear-wave anisotropy in the Frontier-Niobrara zones ranges from near zero to as much as 7 percent. The regions of largest anisotropy along the four lines can be interpreted with two localized zones of relatively intense fracturing (shown in gray in Figure 4.19).

Before beginning the survey, it was suggested that the fractures at depth would trend more along a NW-SE direction, parallel to the strike of the Casper Arch and the associated flexure along the SW edge of the survey (Figure B.1, Appendix B). These were also interpreted from the second derivative of the known structure at depth. This trend is also seen in surface fractures south of the survey area (Mueller, pers. comm.). The Amoco-Arco Morton Ranch well was drilled near the midpoint of survey line 1 and completed right before our seismic survey. Based on this pre-survey interpretation, the well went horizontal in the Niobrara-Frontier interval and trended northeast (almost parallel to line 1), aiming to intersect a maximum number of fractures perpendicular to their trends. In fact, it was observed down-hole that it trended within about 20° of the fracture trend, consistent with the interpretation in Figure 4.19. The initial test production at Morton Ranch was quite promising with 165 BOPD, 380 MCFGPD. However, the productivity decreased quickly to about 16 BOPD and 70 MCFGPD (Figure 4.22). The result of this well suggest that, first of all that the horizontal well didn't intersect that many of them, and secondly, the fractures may be closed because of

the loss of pore pressure due to production – consistent with poor fracture connectivity and low fracture density.

The Red Mountain 1-H well was drilled near the intersection of line 2 and line 4 after the seismic study, using the derived fracture model. The well was reported hitting numerous fractures, consistent with the fracture model, and the test production on July 18, 1994 showed 1068 MCFGPD, 32BOPD and only 3 barrels of water per day. The initial result demonstrated once again the effectiveness of the four-component shear-wave method developed by Alford. Since the well is fairly new, much information is still not available and this result is only preliminary. A number of older vertical wells confirm the fracture model. For example the Chinook Lois, Apache Githens, and Energetics Simms wells (Table B.2, Appendix B) all lie within the fracture zones (gray in Figure 4.19) and all have shown reasonable production. A few others outside of the interpreted fracture zones performed much worse.

Several attributes of the P-wave data were found to be consistent with, and possibly indicators of fractures: Strong lateral variations in P-wave reflectivity, AVO response, and frequency content were observed along line 2. Although we did not attempt to model quantitatively their response, they could be indicators of gas and fractures. However, such scalar attributes along a single 2-D line — no matter how striking — cannot give information about the direction of fractures that is so critical for designing wells. It is possible that with more work, we could learn to combine these scalar attributes with independent fracture direction information (for example from regional trends, or measured stress directions) to quantitatively characterize fractures. We recommend further work in learning to quantify the various P-wave scalar attributes associated with fractures.

Perhaps most intriguing are the several indications of P-wave anisotropy that we observed. Azimuthal variations of AVO response and P-wave stacking velocity were observed at the intersections of lines 1-2 and 2-3. The azimuthal velocity variation is consistent with the directions of the fracture model.

An important conclusion is that 2-D single component surveys are likely to be inadequate for fracture mapping. In our survey, only two line intersections allowed us to even look for azimuthal P-wave variations. We recommend looking for these variations in 3-D single component data. 3-D data will allow, in general, a more complete sampling of azimuths at many CDPs. Partly as a result of this work, Arco is now beginning a 3-D study to look for fracture-related azimuthal variations of P-wave stacking velocity and we at Stanford are beginning a similar 3-D study to look for fracture-related azimuthal variations in AVO.

References

Alford, R. M., 1986, Shear data in the presence of azimuthal anisotropy: Dilley, Texas, paper presented at the 56th Annual Meeting, Soc. of Explor. Geophys., Houston.

Anstey, N. A., Whatever happened to ground roll?: The leading edge, **5**, 40-45.

Banik, N. C., 1984, Velocity anisotropy of shales and depth estimation in the North Sea basin: Geophy., **49**, 1411-1419.

Beydoun, W. B., Cheng, C. H., and Toksoz, M. N., 1985, Detection of open fracture with vertical seismic profiling, J. Geophys. Res., **90**, 4557-4566.

Blangy, J. P., 1992, Integrated seismic lithologic interpretation: the petrophysical basis: Ph.D. dissertation, Stanford University.

Blangy, J. P., 1994, AVO in transversely isotropic media — an overview: Geophys., **59**, 775-781.

Crampin, S., 1978, Seismic wave propagation through a cracked solid: polarization as a possible dilatancy diagnostic, Geophys. J. R. Astron. Soc., **53**, 467-496.

Crampin, S., McGonigle, R. and Bamford, D., 1980, Estimating crack parameters from observations of P-wave anisotropy, Geophys., **40**, 345-360.

Crampin, S., 1984, Effective anisotropic elastic constants for wave propagation through cracked solids, Geophys. J. Roy. Astr. Soc., **76**, 135-145.

Crampin, S., Evans, R., and Ucer, S. B., 1985, Analysis of records of local earthquakes: the Turkish dilatancy projects (TDP1 and TDP2), Geophys. J. R. Astron. Soc., **83**, 1-16.

Crampin, S., Bush, I., Naville, C., and Tylor, D. B., 1986, Estimating the internal structure of reservoirs with shear-wave VSPs: The Leading Edge, **5**, 35-39.

Crampin, S., 1988, Extensive-dilatancy anisotropy, new earthquake prediction tool (meeting report), Eos Trans. AGU, **69**, 729.

Hildebrandt, G. F., Morse, P. F., 1986, Suppression of coherent noise by the stack array: Geophysics, **51**, 873.

Hudson, J. A. , 1981, Wave speeds and attenuation of elastic waves in material containing cracks, Geophys. J. Roy. Astr. Soc., **64**, 133-150.

Hudson, J. A., 1991, Crack distributions which account for a given seismic anisotropy, Geophys. J. Int., **104**, 517-521.

Johnston, D. H., 1986, VSP detection of fractured-induced velocityanisotropy, 56th Ann. Int. SEG Meeting, 1986, Houston, Expanded Abstracts, 464-466.

Lewis, C., 1989, Three-dimensional Multicomponent Imaging of Reservoir Heterogeneity, Silo Field, Wyoming, Ph.D. Dissertation, Colorado School of Mines.

Lorenz, J. C., Branagan, P., Warpinski, N. R., and Sattler, A. R., 1986, Fracture characteristics and reservoir behavior of stress sensitive fracture systemsin flat-lying lenticular formations: Paper presented at Proceedings of Unconventional Gas Technical Symposium, Soc. of Pet. Eng., Louisville, Ky.

Mallick, S. and Frazer, L. N., Reflection/transmission coefficients and azimuthal anisotropy in marine seismic studies: Geophys. J. Int., **105**, 241-252.

Mavko, G. and Nur, A., 1979, Wave attenuation in partially saturated rocks: Geophysics, **44**, 161-178.

Mueller, M., 1992, Using shear waves to predict lateral variability in vertical fracture intensitiy: The leading Edge, **11**, 29-35.

Mukerji, T. and Mavko, G., 1994, Pore fluid effects on seismic velocity in anisotropic rocks, in press, Geophysics..

Ostrander, W. J., 1983, Plane-wave reflection coefficients for gas sands at non-normal angles of incidence: 52nd ann. int. SEG mtg., Dallas, Texas, 443

Ostrander, W. J., 1984, Plane-wave reflection coefficients for gas sands at nonnormal angles of incidence: Geophysics, **49**, 1637-1648.

Pelissier, M. A., Thomas-Betts, A. and Vestergaard, P. D., Azimuthal variations in scattering amplitudes induced by transverse isotropy: Geophysics, **56**, 1584-1595.

Sengupta, M., 1987, Sensitivity analysis of amplitude versus offset (AVO) method: 57th ann. int. SEG mtg., New Orlean, LA, 621-623.

Szpakiewicz, M. J., McGee, K., and Sharma, B., 1986, Geologic problems related to characterization of clastic reservoirs for enhanced oil recovery: Proceedings of the SPE/DOE Fifth Symposium on Enhanced Oil Recovery, **2**, 97-106, Soc. of Pet. Eng., Tulsa, Okla.

Taner, M. T. and Koehler, F., 1981, Surface consistent corrections: Geophysics, **46**, 17-22.

Thomsen, L., 1986, Elastic anisotropy due to aligned cracks: Theoretical models, Trans. Am. Geoph. Union, **67** , 1207.

Vernik, L. and Nur, A., 1992, Ultrosonic velocity and anisotropy of hydrocarbon source-rocks: Geophysics, **57**, 727-735.

Willis, H. A., Rethford, G. L. and Bielavski, E., 1986, Azimuthal anisotropy: occurrence and effect of shear wave data quality, paper presented at 56th Annual Meeting, Soc. of Explor. Geophys., Houston.

Wright, J., The effects of transverse isotropy on reflection amplitude versus offset: Geophysics, **52**, 564-567.

Wyoming Geological Association, 1976, Guidebook, 28th Annual Field Conference, Geology and energy resources of the Powder River: Casper, Wyoming, 328 p.

Yin, H., 1992, Acoustic Velocity and Attenuation of rocks: Isotropy Intrinsic Anisotropy, and Stress Induced Anisotropy, Ph.D. dissertation, Stanford University, Stanford, California.

Appendix A

Stiffness matrices

The stiffness matrices of the anisotropic systems are

Triclinic system:
$$\begin{bmatrix} c_{11} & c_{12} & c_{13} & c_{14} & c_{15} & c_{16} \\ c_{12} & c_{22} & c_{23} & c_{24} & c_{25} & c_{26} \\ c_{13} & c_{23} & c_{33} & c_{34} & c_{35} & c_{36} \\ c_{14} & c_{24} & c_{34} & c_{44} & c_{45} & c_{46} \\ c_{15} & c_{25} & c_{35} & c_{45} & c_{55} & c_{56} \\ c_{16} & c_{26} & c_{36} & c_{46} & c_{56} & c_{66} \end{bmatrix}, \quad \text{21 constants}$$

Monoclinic system:
$$\begin{bmatrix} c_{11} & c_{12} & c_{13} & 0 & c_{15} & 0 \\ c_{12} & c_{22} & c_{23} & 0 & c_{25} & 0 \\ c_{13} & c_{23} & c_{33} & 0 & c_{35} & 0 \\ 0 & 0 & 0 & c_{44} & 0 & c_{46} \\ c_{15} & c_{25} & c_{35} & 0 & c_{55} & 0 \\ 0 & 0 & 0 & c_{46} & 0 & c_{66} \end{bmatrix}, \quad \text{13 constants}$$

Orthorhombic system:
$$\begin{bmatrix} c_{11} & c_{12} & c_{13} & 0 & 0 & 0 \\ c_{12} & c_{22} & c_{23} & 0 & 0 & 0 \\ c_{13} & c_{23} & c_{33} & 0 & 0 & 0 \\ 0 & 0 & 0 & c_{44} & 0 & 0 \\ 0 & 0 & 0 & 0 & c_{55} & 0 \\ 0 & 0 & 0 & 0 & 0 & c_{66} \end{bmatrix}, \quad \text{9 constants}$$

Tetragonal system:
$$\begin{bmatrix} c_{11} & c_{12} & c_{13} & 0 & 0 & c_{16} \\ c_{12} & c_{11} & c_{13} & 0 & 0 & -c_{16} \\ c_{13} & c_{13} & c_{33} & 0 & 0 & 0 \\ 0 & 0 & 0 & c_{44} & 0 & 0 \\ 0 & 0 & 0 & 0 & c_{44} & 0 \\ c_{16} & -c_{16} & 0 & 0 & 0 & c_{66} \end{bmatrix} \quad \text{7 constants}$$

Tetragonal system with a 2-fold symmetry axis perpendicular to the 4-fold axis:

$$\begin{bmatrix} c_{11} & c_{12} & c_{13} & 0 & 0 & 0 \\ c_{12} & c_{11} & c_{13} & 0 & 0 & 0 \\ c_{13} & c_{13} & c_{33} & 0 & 0 & 0 \\ 0 & 0 & 0 & c_{44} & 0 & 0 \\ 0 & 0 & 0 & 0 & c_{44} & 0 \\ 0 & 0 & 0 & 0 & 0 & c_{66} \end{bmatrix} \quad 6 \text{ constants}$$

Trigonal systems:

$$\begin{bmatrix} c_{11} & c_{12} & c_{13} & c_{14} & -c_{25} & 0 \\ c_{12} & c_{11} & c_{13} & -c_{14} & c_{25} & 0 \\ c_{13} & c_{13} & c_{33} & 0 & 0 & 0 \\ c_{14} & -c_{14} & 0 & c_{44} & 0 & c_{25} \\ -c_{25} & c_{25} & 0 & 0 & c_{44} & c_{14} \\ 0 & 0 & 0 & c_{25} & c_{14} & (c_{11}-c_{12})/2 \end{bmatrix}, \quad 7 \text{ constants}$$

Trigonal system with a 2-fold symmetry axis perpendicular to the 3-fold axis:

$$\begin{bmatrix} c_{11} & c_{12} & c_{13} & c_{14} & 0 & 0 \\ c_{12} & c_{11} & c_{13} & -c_{14} & 0 & 0 \\ c_{13} & c_{13} & c_{33} & 0 & 0 & 0 \\ c_{14} & -c_{14} & 0 & c_{44} & 0 & 0 \\ 0 & 0 & 0 & 0 & c_{44} & c_{14} \\ 0 & 0 & 0 & 0 & c_{14} & (c_{11}-c_{12})/2 \end{bmatrix}, \quad 6 \text{ constants}$$

Hexagonal system:

$$\begin{bmatrix} c_{11} & c_{12} & c_{13} & 0 & 0 & 0 \\ c_{12} & c_{11} & c_{13} & 0 & 0 & 0 \\ c_{13} & c_{13} & c_{33} & 0 & 0 & 0 \\ 0 & 0 & 0 & c_{44} & 0 & 0 \\ 0 & 0 & 0 & 0 & c_{44} & 0 \\ 0 & 0 & 0 & 0 & 0 & (c_{11}-c_{12})/2 \end{bmatrix}, \quad 5 \text{ constants}$$

Cubic system:

$$\begin{bmatrix} c_{11} & c_{12} & c_{12} & 0 & 0 & 0 \\ c_{12} & c_{11} & c_{12} & 0 & 0 & 0 \\ c_{12} & c_{12} & c_{11} & 0 & 0 & 0 \\ 0 & 0 & 0 & c_{44} & 0 & 0 \\ 0 & 0 & 0 & 0 & c_{44} & 0 \\ 0 & 0 & 0 & 0 & 0 & c_{44} \end{bmatrix}, \quad 3 \text{ constants}$$

Appendix B

Regional geologic framework and site description

Rob Walters, Wei Chen, and Gary Mavko

B.1 Structural features

The "Fort Fetterman" site is located at the southwestern margin of the Powder River basin, north of the town of Douglas, in Converse County, east-central Wyoming. The Powder River basin is one of many structural features formed during the Laramide Orogeny that occurred during latest Cretaceous to early Tertiary time in the western Cordillera (Dickinson et al., 1988). In the Rocky Mountain region, the typical structural style consists of a series of "basement-cored uplifts and intervening sediment-filled basins" (Dickinson et al., 1988) over a wide area. The study site is bounded to the south and west by the Casper Arch to the southeast by the Hartville Uplift (Figure B.1). As discussed below, these structural features may have had a considerable influence on the formation of preferred fracture orientations.

Mitchell and Rogers (1993) note that the southern end of the Powder River basin has been significantly influenced by an extensional system of nearly vertical normal faults that affects Lower Cretaceous, Upper Cretaceous and Tertiary units. They proposed that these faults, which have throws of 30 feet or less, are basement derived, and controlled deposition of the Upper Cretaceous Frontier and Niobrara Formations. The fault systems appear to trend northwest-southeast in the south-central part of the basin, and northeast-southwest at the southern margin, parallel to the Hartville Uplift (Figure B.2, Mitchell and Rogers, 1993). Slack (1981) also proposed a series of northeast-trending structural lineaments northeast of the study area, which extend northeastward to the Black Hills monocline. Mitchell and Rogers (1993) noted that a number of important producing fields in the southern Powder River basin have fracturing as an important reservoir component (Figure B.3), and proposed that fracture potential is key to production from "conventional" sandstone reservoirs as well as shale reservoirs.

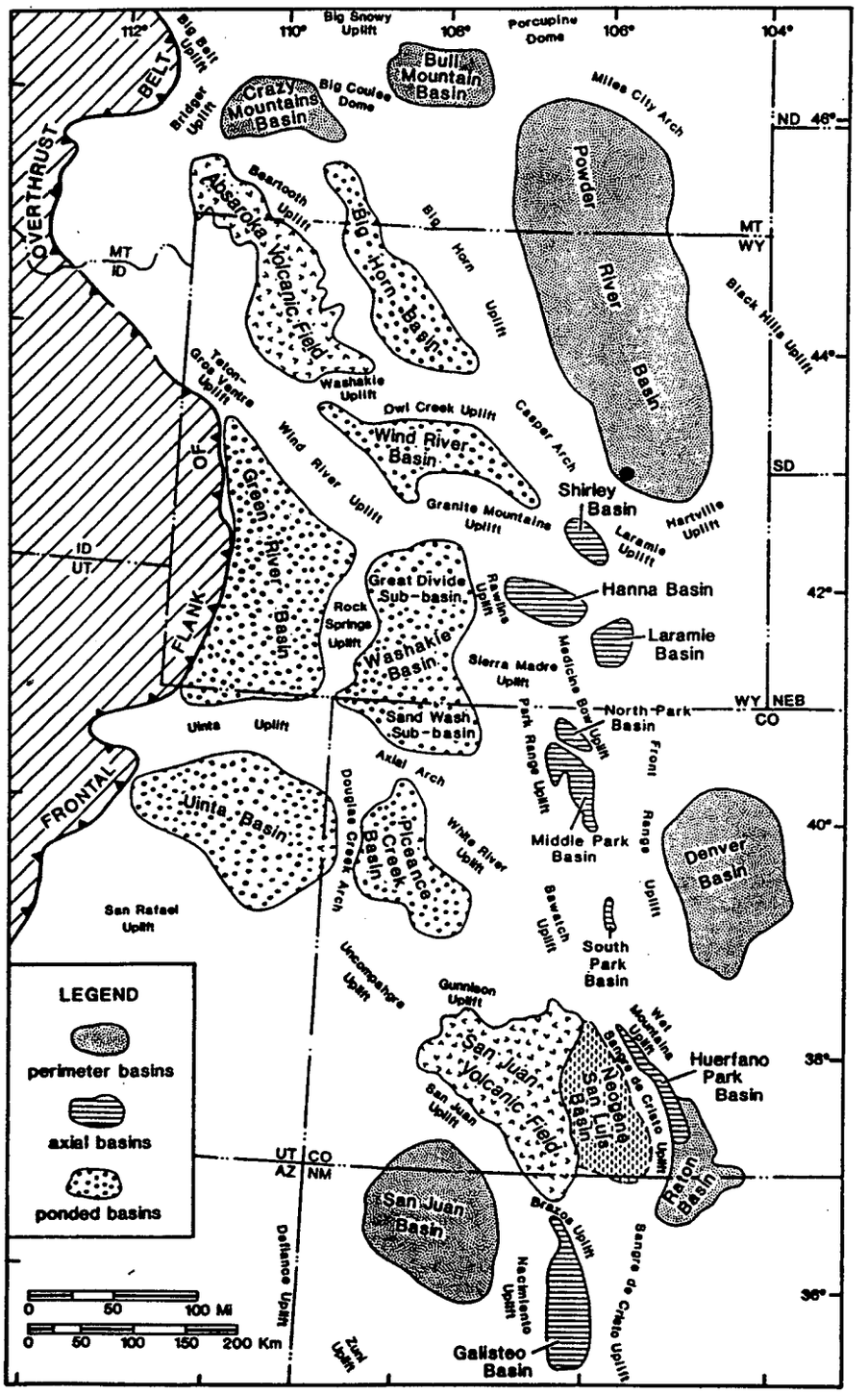

Figure B.1: Laramide structural features in the central Rocky Mountain region, from Dickinson et al. (1988). Large dot at southwestern edge of Powder River basin in east-central Wyoming denotes approximate location of the study site.

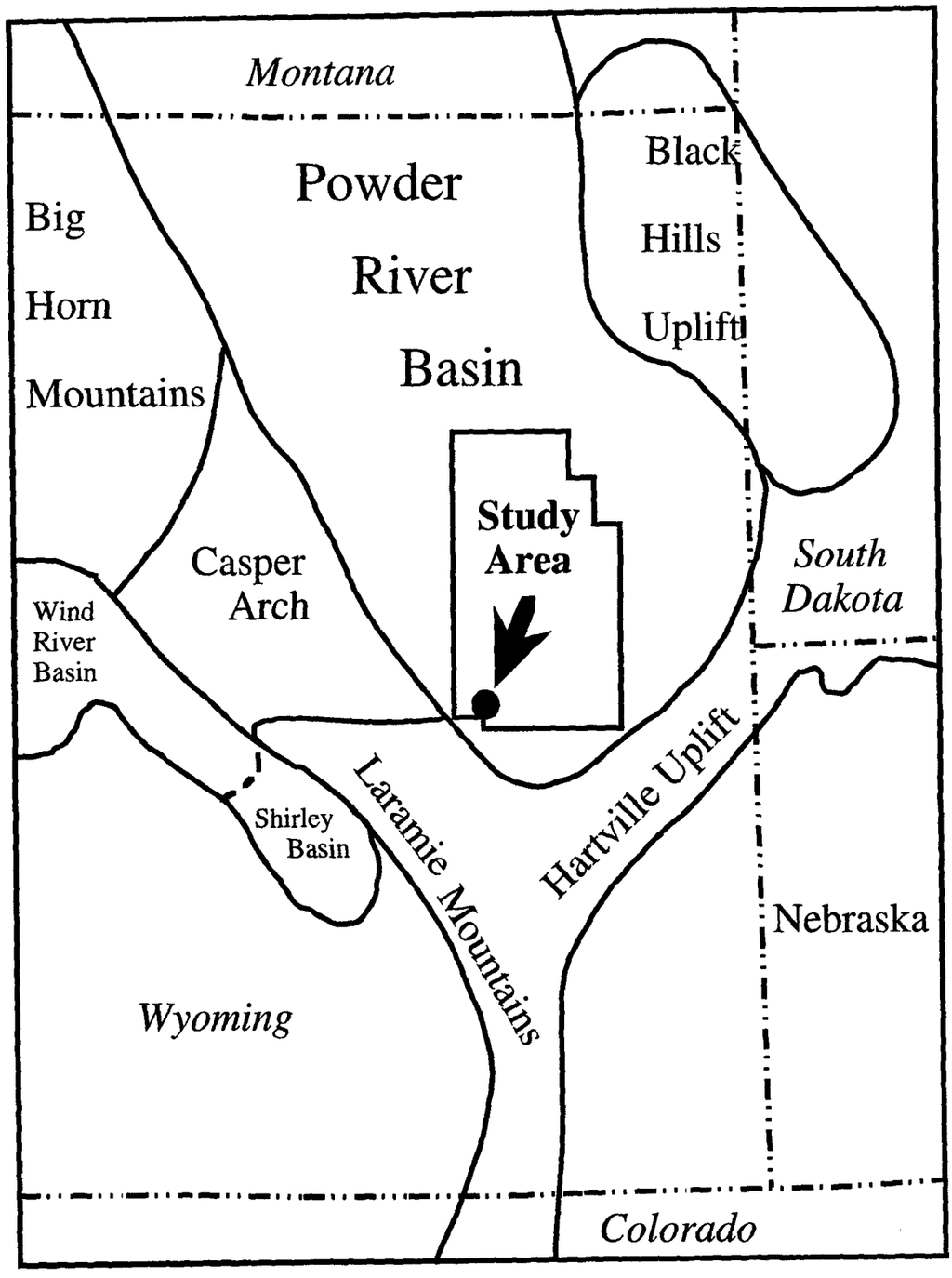

Figure B.2: Structural features in eastern Wyoming, from Mitchell and Rogers (1993), showing Powder River basin (shaded area), and adjacent Hartville Uplift to the southeast. The study site is marked by dot.

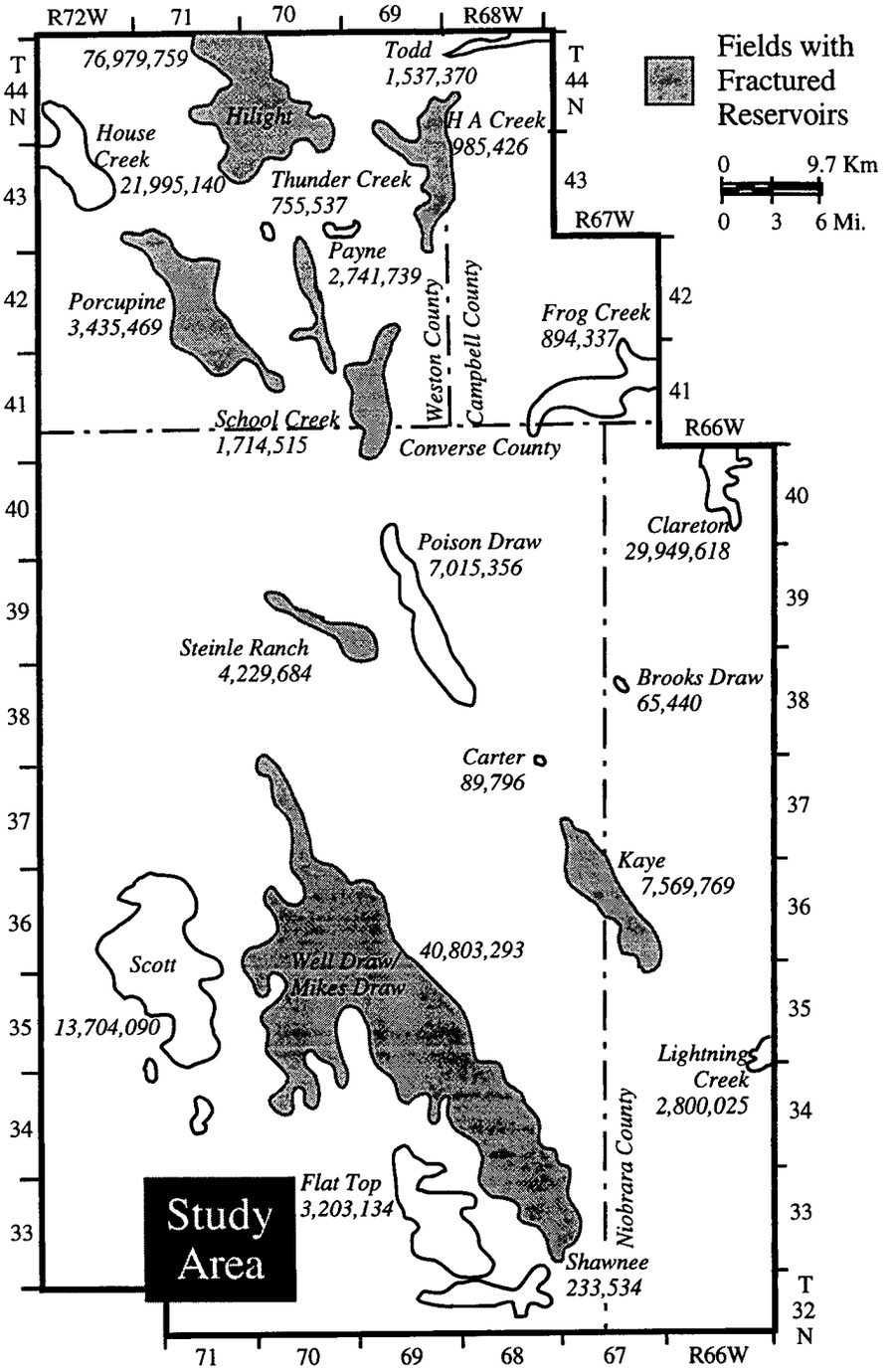

Figure B.3: Producing fields in Converse County and vicinity, Wyoming, from Mitchell and Rogers (1993); shaded areas are known to produce from fractured reservoirs. The study site is outlined at lower left.

B.2 Overpressure

Overpressuring is another potentially important parameter in defining the characteristics of reservoirs in the southern Powder River basin. The major source rocks in the southern Powder River basin are Lower Cretaceous shales (Skull Creek and Mowry) and the Upper Cretaceous Niobrara Formation, which is also a reservoir. Overpressuring is responsible for preservation of primary porosity at depth and maintenance of open fractures (Mitchell and Rogers, 1993). This fracture porosity is important at Silo Field, located more than 100 miles south of the study area, since the Niobrara in this field is a chalk rather than a shale. Mitchell and Rogers (1993) explain the abundance of hydrocarbon shows from "unconventional" reservoirs in the Upper Cretaceous Frontier equivalents (and the Niobrara) as being due to preserved primary porosity and the presence of open fractures.

In the southern Powder River Basin, overpressuring occurs from the Lower Cretaceous Fall River Formation to the top of the Niobrara, and is caused by generation and expulsion of hydrocarbons from Lower Cretaceous Mowry and Upper Cretaceous Niobrara source rocks (Mitchell and Rogers, 1993). Within our study area pressure gradients from drillstem tests range from 0.47 psi/ft in the southeast corner of T33N R71W to 0.51 psi/ft to the northwest (Mitchell and Rogers, 1993), with an overall increase in pressure gradient from south to north.

B.3 Regional stratigraphy and depositional environments

Figure B.4 shows the stratigraphic nomenclature developed for various basins in Wyoming from the Precambrian to the Tertiary. This study is primarily concerned with upper Cretaceous sediments in the southwestern portion of the Powder River basin. Information for the formations listed below was taken from articles by Barlow and Haun (1966), Hando (1976), Merewether et al. (1976), Prescott (1975), and the Wyoming Geological Association Guidebook (1976).

The following is a summary of Upper Cretaceous stratigraphy in the study area:

- *Parkman Sandstone*: offshore marine bar (shelf) sand, deposited in 100-200 feet water depths; composed of discrete sand lenses encased in siltstone and shale. Hydrocarbon productive in other areas of the Powder River basin.
- *Steele Shale*: marine shale.
- *Sussex Sandstone*: shelf sand, deposited in 100-200 feet water depths, influenced by longshore currents; composed of discrete, lenticular sand bodies encased in

interbedded siltstone and shale. Hydrocarbon productive in other areas of the Powder River basin.

- *Niobrara Formation*: unconformably overlies the Frontier; a series of fractured, marine chalks and limestones interbedded with calcareous shales and bentonites. Oil and gas reservoir that is its own source rock. Open fractures necessary for production due to low porosity and permeability.
- *First Frontier Sand*: uppermost of three sands within the Frontier Formation; fractured, offshore marine bar sand containing interbedded shales in 3-4 transgressive-regressive cycles; grades upward regionally from marine shale to sandstone at the top. Reservoirs are thin, low permeability; pay section is coarse grained, reworked. Lower limit of 8% porosity is necessary for effective pay thickness.
- *Mowry Shale*: dark grey to black, hard, siliceous shales interbedded with thin siltstone and sands, plus regionally extensive bentonite beds. Deposited in very stable depositional environment, greater than 500 feet water depths.

B.4 Frontier Formation

The Frontier and equivalent formations comprise the interval between the Mowry Shale and the Niobrara Formations in the lowermost part of the Upper Cretaceous in the Rocky Mountain region. The section includes sand bodies interbedded with marine shale, ranging up to 1,000 feet thick in central, west-central and northeast Wyoming (Barlow and Haun, 1966). The sands are interpreted as having been deposited by fluvio-deltaic processes along the margins of the Western Interior Seaway during early Late Cretaceous time. Rivers flowing eastward across the Cordillera during this time from a source area located west-northwest of the Yellowstone Park area created these areally extensive deltas (Barlow and Haun, 1966; Prescott, 1975).

The informal terms "first Frontier sandstone" and "second Frontier sandstone" denote the important producing sands, with the second Frontier accounting for most of the oil production from the giant Salt Creek field in Natrona County, Wyoming (Barlow and Haun, 1966). Salt Creek field is located approximately 60 miles northwest of the study area. These sands were generally deposited in the subaqeous portion of the delta, and reflect a marine influence, rather than merely fluvial influx. Thus, they are part of the shore-zone system (Galloway and Hobday, 1983), whose components include beaches, barriers, lagoons and tidal flats.

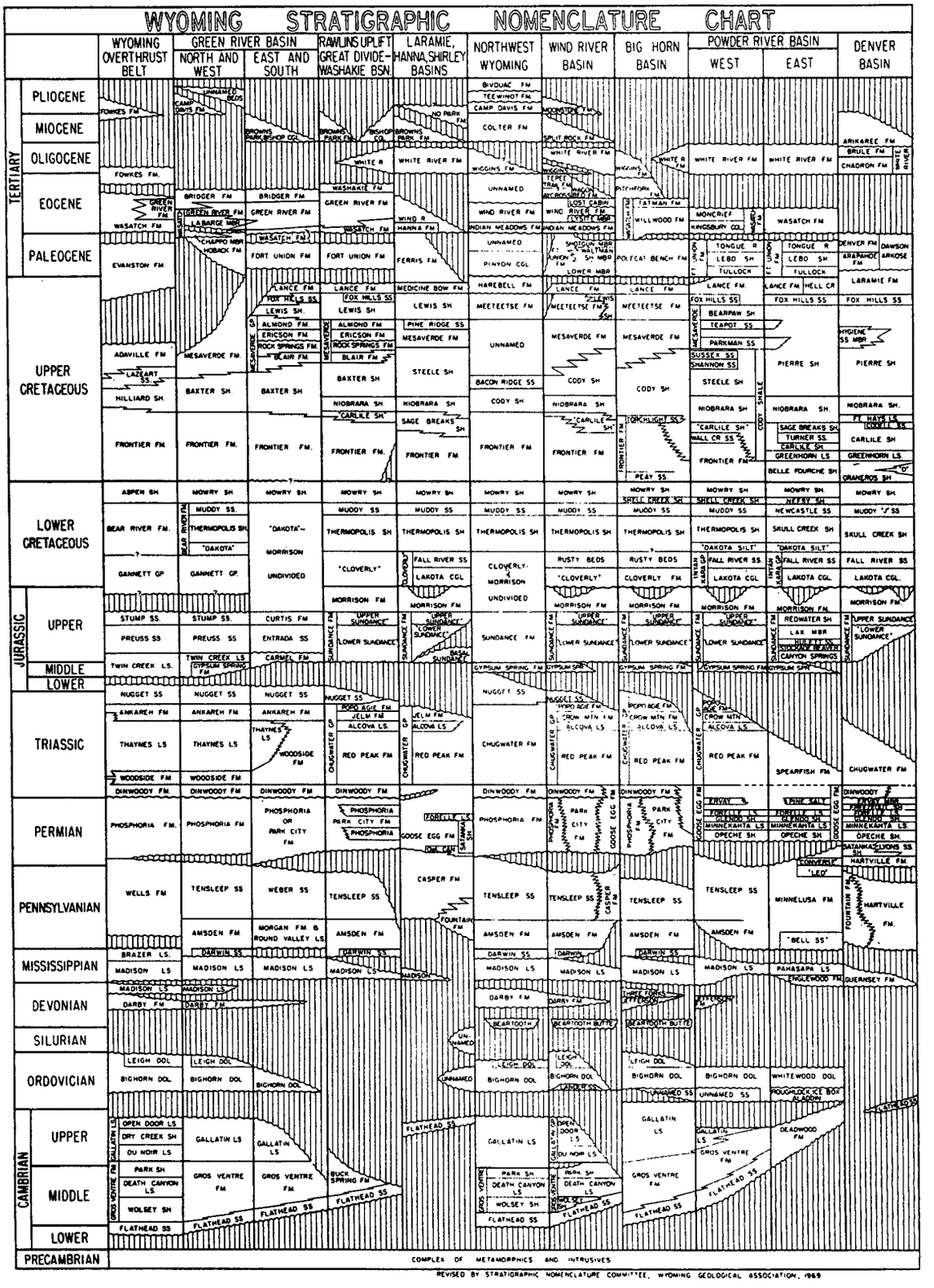

Figure B.4: Stratigraphic nomenclature (Wyoming Geol. Assoc. Guidebook, 1976).

At Spearhead Ranch field, located approximately 40 miles north-northwest of the study area in Converse County, the producing first Frontier reservoir is referred to as an "offshore marine bar" (Prescott, 1975). Detailed analysis of well logs from this field (Prescott, 1975) suggests three or four regressive-transgressive cycles within the first Frontier sandstone interval. In both the Spearhead Ranch and Salt Creek fields, the trapping mechanism is stratigraphic, and at Spearhead Ranch field, the interval dips uniformly to the southwest with no closure (Prescott, 1975).

In the southern Powder River basin, another stratigraphic classification divides the time-equivalent of the Frontier Formation into (oldest to youngest) the Belle Fourche Shale, Greenhorn Limestone, and the Carlile Formation (Mitchell and Rogers, 1993). The Carlile is then subdivided into the Turner Sandstone Member, consisting of well-sorted marine sands and silts, and the Sage Breaks Member, a marine, calcareous shale. This area includes the DOE site in southern Converse County, as well as parts of Campbell, Weston and Niobrara Counties. Mitchell and Rogers (1993) note that the Turner is a good potential target for horizontal drilling, since it is a fractured reservoir.

In the Kaycee-Tisdale Mountain area, the Frontier incorporates interstratified shale, siltstone, sandstone and bentonite, with the Wall Creek Sandstone Member at the top (Merewether et al., 1976). This area is located on the western flank of the Powder River Basin in Johnson County, northwest of Spearhead Ranch field. Merewether et al. (1976) suggest that most of the Frontier sands in this area were deposited in wave-dominated deltaic environments.

In southwest Wyoming, the Frontier in the Green River basin consists of both marine and nonmarine sandstones and shales, with increasing dominance of marine deposits to the east, toward the Western Interior Seaway (Dutton et al., 1992). Along the Moxa Arch, a north-trending uplift close to the eastern boundary of the Thrust Belt, the Frontier is composed of shoreline sands and fluvial channel-fill sands, and is encased by thick shales. The subdivisions into First Frontier sandstone, Second Frontier sandstone, etc. are applicable, and the Second Frontier (a fluvial-deltaic system) contains low permeability gas reservoirs from which the majority of the production in the western Green River Basin is derived (Dutton et al., 1992).

The Powell-Ross field is located in Converse County just northwest of the study site in T40N, R74W; average porosity for this field is given as 15%. Typical porosities for Frontier reservoir sands in the Powell-Ross field range from a cutoff limit of 8% for effective pay thickness to a high of 22% (Hando, 1976). Completions from the Frontier produce both oil and gas, with the Powell II Unit No. 1 well completed for 624 BOPD and 2.2 MCFGPD (Hando, 1976). For the larger Spearhead Ranch field nearby, in T37-40N,

R74-75W, Prescott (1975) noted when porosities are less than 8%, the reservoir becomes uneconomic, due to insufficient permeability. Most development wells in this field average about 1,000 BOPD and 2-2.5 MMCFGPD (Prescott, 1975). The trapping mechanism at Spearhead Ranch is purely stratigraphic, and the first Frontier is an offshore marine bar. Hydrocarbon production from fractured reservoirs is not mentioned for these fields.

B.5 Frontier Formation and fracture patterns in field studies

Comparatively few published studies have attempted to relate fracture patterns in the field to those observed in cores. Dutton et al. (1992) conducted a detailed study of natural fractures in the Frontier Formation in the Moxa Arch and western Green River basin of southwestern Wyoming as part of the Gas Research Institute's Tight Gas Sands project. They examined data from both cores and outcrops; core data showed that, although extension fractures were closely spaced, they were often confined to individual sand members and formed vertically discontinuous strands striking predominantly north and east. In outcrop, dominant strike directions near Kemmerer, Wyoming were bimodal, with a closely spaced (from 4" to 3') north-striking set and a younger, cross-cutting, more widely spaced set that strikes east-west.

Dutton et al. (1992) found no consistent relationship between the presence of a given fracture set and current structural position, and attributed subtle differences in original composition or diagenesis as important factors affecting the tendency of the rock to fracture. They found a compartmentalization of fracture arrays and drastically varying connectivity even within the same fracture set. In their study area, fracture origin is likely related to isostatic adjustment to loads imposed by proximity to thrust sheets. Dutton et al. (1992) concluded that the vertically confined, isolated fracture swarms in this area would present a more challenging exploration target than those in areas of uniformly spaced, orthogonal fracture sets.

B.6 Frontier Formation at the DOE site

Within the study area, the First Frontier sand lies approximately 100 feet below the top of the Frontier Formation. The First Frontier sand contains fracture sets, as identified from fracture identification (dipmeter) logs. Figure B.5 shows the gamma ray, sonic and density logs for the Apache #36-1 State well (see Figure B.6 for location). At the well, located on the southeastern end of Line 2, this sand produces from a perforated interval from 11,695 to 11,785 feet. Initial production from a test on 3/17/81 was 70 BOPD

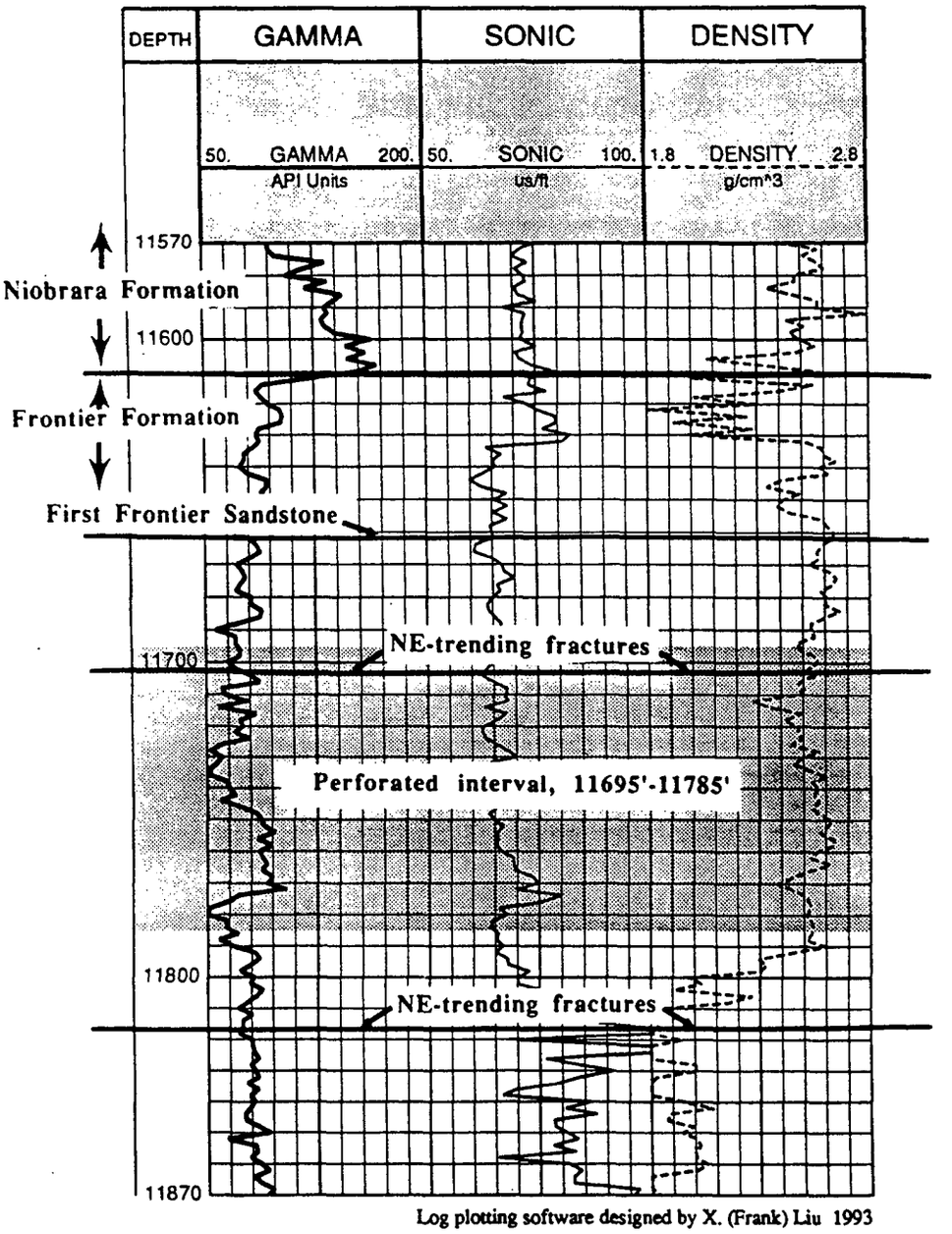

Figure B.5: Plot of gamma ray, sonic and density logs from Apache #36-1 State well (see Figure 23 for location), with formation tops and fracture zones labeled. Producing interval within First Frontier sand is shaded.

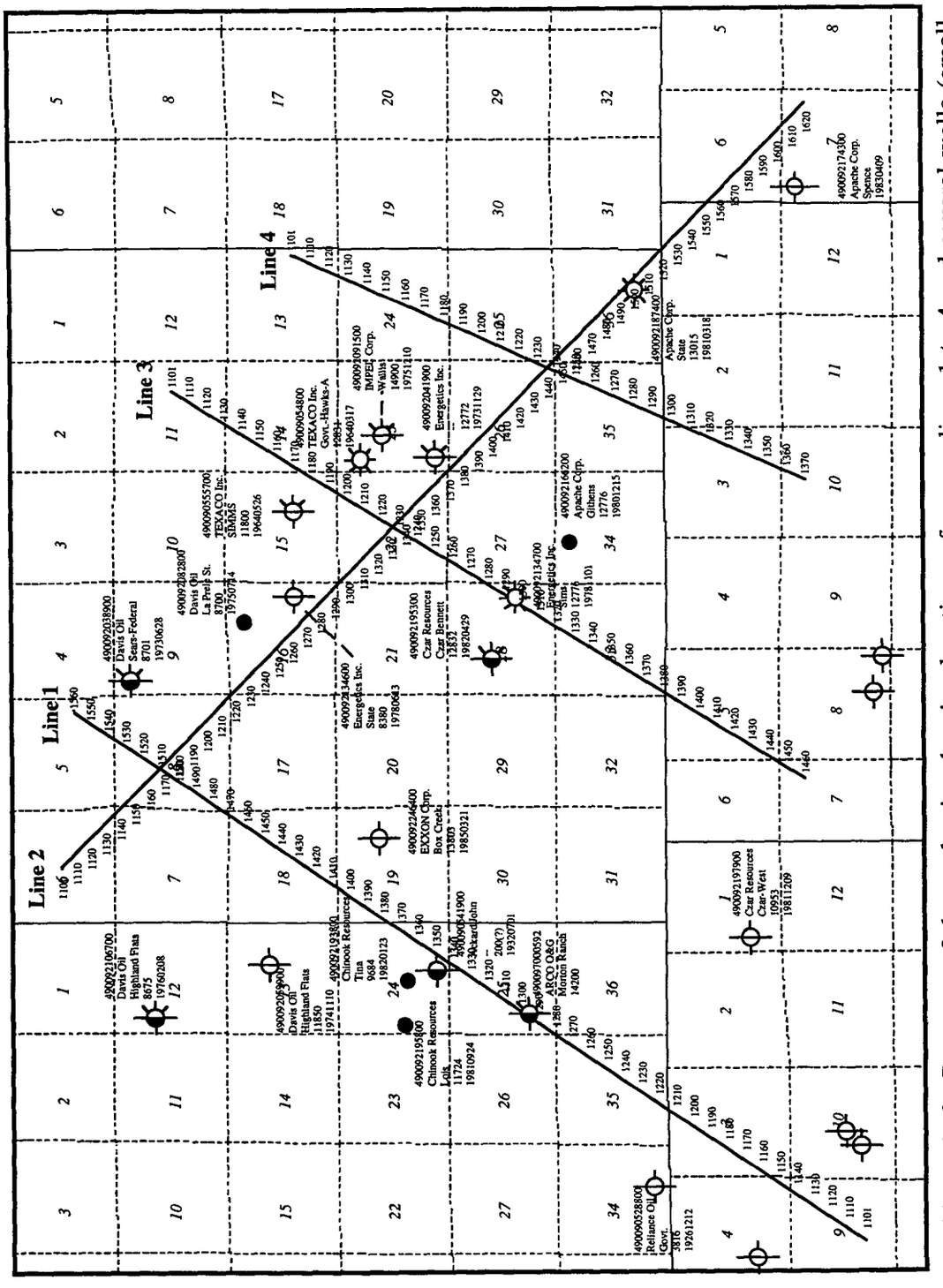

Figure B.6: Basemap of the study site showing locations of survey lines 1 to 4 and several wells (small circles). Also shown are fracture orientation determinations from log results for the Apache #36-1 State well.

and 1,700 MCFGPD. Velocities in this interval, from the sonic log, are rather high, at 65 μs/ft, or 15,400 ft/sec; formation density is 2.5 g/cm^3 (Figure B.5). The velocity decreases to 80 μs/ft, or 12,500 ft/sec below this producing sand.

Another sonic log from the Davis Oil #1 well to the west of line 1 shows approximately the same high velocity character in the first Frontier sand. A core description from the Texaco #1 Sims well in section 15, T33N R71W, indicates that the first Frontier is a fine grained, "tight" sandstone, with a trace of oil.

B.7 Niobrara formation — regional stratigraphy and fracture patterns

The Upper Cretaceous Niobrara Formation directly overlies the Frontier interval. At Silo Field, located northeast of Cheyenne in far southeastern Wyoming, the Niobrara is a naturally fractured, oil-productive chalk (Lewis et al., 1991). Dips are gentle to the southwest, and the chalk is faulted where it drapes over a deeper Permian salt withdrawal, or salt dissolution structure. Fracture orientations parallel this paleostructure, and the average fracture strike is N50°W to N55°W (Lewis et al., 1991). This orientation was also confirmed by dipmeter logs and by 3-D rotation analysis of shear-wave seismic data. Anisotropy, as identified in the azimuthal rotation analysis, was determined to result from vertical fractures alone, rather than from the combined effects of vertical fractures and horizontal layering.

Sonnenberg and Weimer (1993) reported on oil production from the Niobrara in Silo field, and noted that the open fractures which provide the means of producing from this low permeability reservoir were created by a combination of folding, basement faulting, solution of older Permian evaporites, high fluid pressure, and the effects of the regional stress field. Porosities in the Niobrara chalk were found to be approximately 8%, and are proportional to maximum burial depth. Cumulative production from the fractured Niobrara (7,600 feet to 8,500 feet depths) is already greater than 1.3 million BO from 40 vertical wells, and adding in production from horizontal completions brought the total to over 2 million BO through June, 1992.

B.8 Niobrara formation at the DOE site

The Niobrara Formation within the study area is a shale, with high gamma ray counts and a flat SP on the logs. Formation velocity, measured from the sonic log at the Apache #36-1 State well and the Davis Oil #1 well, is approximately 75 μs/ft, or 13,300 ft/sec. Typical formation density is around 2.3 - 2.5 g/cm^3 (see well logs for Apache #1 State, Figure B.5).

B.9 Well completion information and well log data

In the past several decades, tens of wells have been drilled in the Fort Fetterman area. Log data, mainly in paper copy form, are available from approximately sixteen wells in the vicinity of the survey site (refer to Figure B.6 for well locations). Digital log data are available from the Apache #1 State, Chinook Lois and Energetics Simms wells. Table B.1 lists the well names, operators, locations and available logs from each well. For five of the wells, the only available information was the formation tops. All well data information is in the public domain, even though some was obtained from an industry source. Figure B.5 shows gamma ray, sonic and density logs of the Apache state well, and Figure B.7 shows the sonic log of several other wells for comparison.

Table B.1: List of available well logs.

operator	Well Name	Location	Logs
Apache Corp.	#36-1 State	T33N R71W s36	SP, GR, BHC, DI-SFL, CNP-D, FID
Apache Corp.	Githens	T33N R71W s34	SP, GR, BHC, DI-SFL, CN-FD
Chinook Res.	Lois	T33N R72W s24	SP, GR, DI-SFL, BD
Czar Res.	Czar Bennett	T33N R71W s28	SP, GR, BHC, DI-FL, CN, CD, Spectralog
Czar Res.	Czar West	T32N R72W s1	SP, GR, BHC, DI-L, FID
Davis Oil	Fort Fetterman	T33N R72W s20	SP, GR, BHC, DI-SFL
Energetics	#43-28 Simms	T33N R71W s28	SP, GR, BHC, DI-SFL, CNP-D, BD
Exxon Corp.	#1 Box Creek	T33N R71W s19	SP, GR, BHC, DI-FL, CN, CD, AF, Spetralog
Impel Corp.	#1 Wallis	T33N R71W s23	SP, GR, BHC, DI-L, CN-FD
Texaco Inc.	Simms	T33N R71W s15	SP, GR, IEL, Sonic
Texaco Inc.	Govt.-Hawks-A	T33N R71W s23	SP, GR, IEL, Sonic
Arco Oil & Gas	Morton Ranch	T33N R72W s25	formation tops only
Vastar Res. Inc.	Red Mountain 1-H	T33N R71W s35	formation tops only
Apache Corp.	Spence	T32N R70W s7	formation tops only
Davis Oil	Highland Flats	T33N R72W s13	formation tops only
Energetics	Wallis	T33N R71W s23	formation tops only

Key: SP = spontaneous potential, GR = gamma ray, BHC = borehole compensated sonic, DI-SFL = dual induction, spherically focused log, DI-L = dual induction, laterolog, IEL = induction electric log, CNP-D = compensated neutron porosity-density, CN-FD = compensated neutron-fromation density, CN = compensated neutron, CD = compensated density, BD = bulk density, AF = acoustic fraclog, FID = fracture identification log.

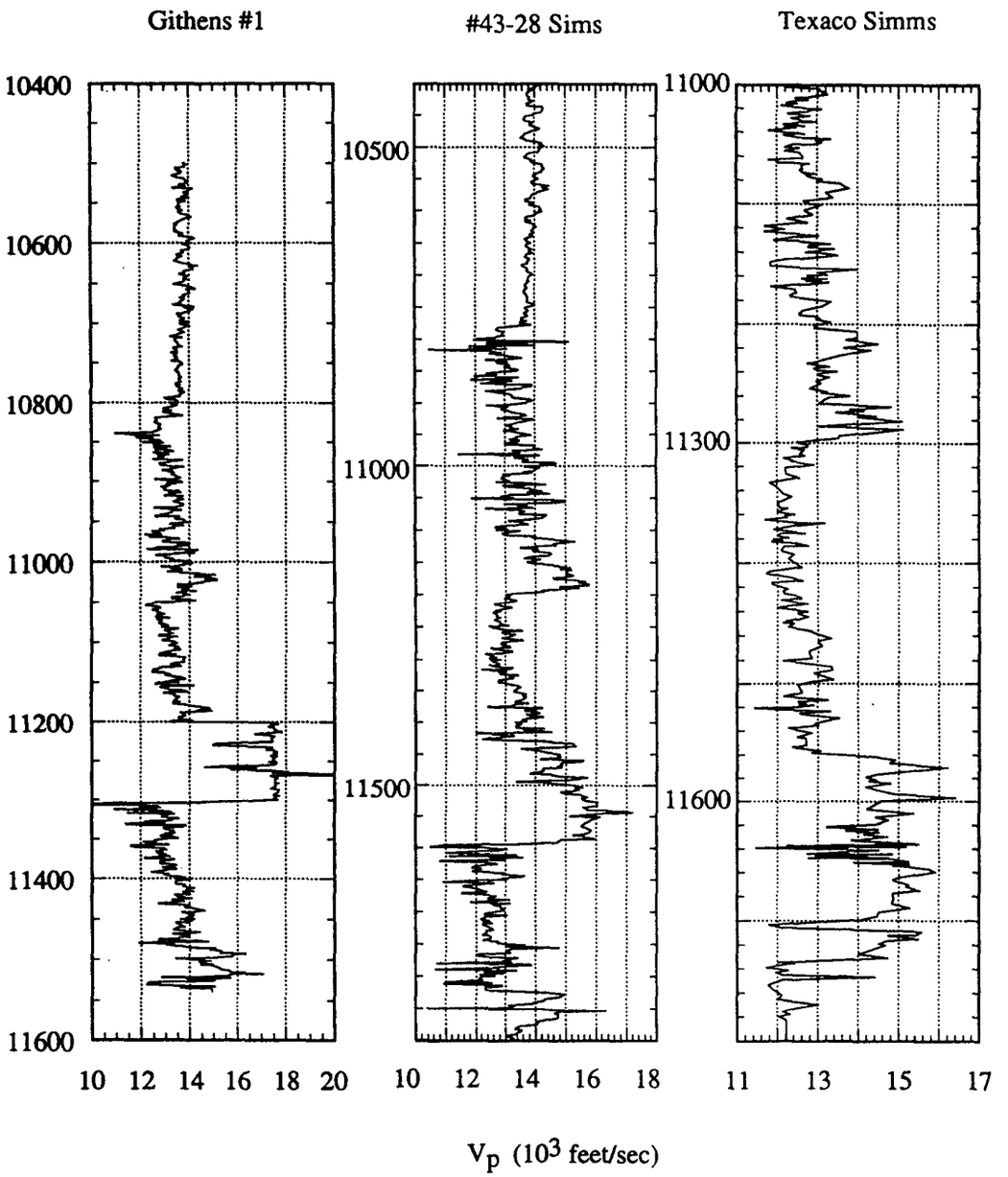

Figure B.7: Sonic logs of Githens #1, #43-28 Sims and Texaco Simms wells.

Table B.2 lists some useful information compiled from the well completion reports and log data. It includes formations tops, production information, P-wave velocities and densities for the Niobrara formation and the Frontier formation. As we can see, this site shows very complex characteristics in terms of well productivity: some wells were completely dry, some were gas wells and some produced oil as well as gas. There seems no apparent correlation between well productivity and log data.

Table B.2: Formation tops and production information of wells at Fort Fettertmen site.

	Parkman Sand	Steele Shale	Sussex Sand	Niobrara Shale	1st Frontier	Mowry Shale	Production (per day)
#36-1 State	8387	8956	-	11050	11662	12488	gas 1700mcf oil 70b
Githens	8200	8790	9456	10782	11522	12330	oil 10b
Lois	8120	-	9472	10691	11577	-	oil 135b
Czar Bennett	-	-	9445	10732	-	-	dry
Czar West	5737	-	7150	8685	9458	-	dry
Fort Fetterman	7178	7880	8603	10250	10810	11710	dry
#43-28 Sims	8119	8723	10223	10800	11463	12311	gas 227mcf oil 50b
#1 Box Creek	8097	-	9412	10730	11390	12290	dry
Energetics Wallis #1	-	8890	9663	-	11605	12475	dry
Texaco Simms	8248	8826	-	11030	11454	-	dry
Govt. Hawks A	8278	8848	-	11045	11448	12416	gas 71mcf
Morton Ranch	7578	8338	9084	10285	11503	-	gas 380mcf oil 165b
Red Mountain	8218	-	9580	10750	11550	-	gas 1068mcf oil 32b
Spence	8670	-	10010	11210	11810	-	dry

Two wells are particularly worth noticing. The Amoco-Arco Morton Ranch well was drilled near the midpoint of survey line 1 and completed right before our seismic survey. Before the drilling, geologists at Amoco and Arco hypothesized that the fractures should be trending northwest, based on the outcrop observations and the structural information (the fractures are usually parallel to the flexure at the basin boundary, refer to Figure B.1). Consequently the well went horizontal in the Niobrara-Frontier interval and trended northeast, aiming to intersect a maximum number of fractures. The initial test production was quite promising with 165 BOPD, 380 MCFGPD. However, the productivity decreased quickly to about 16 BOPD and 70 MCFGPD (Figure B.8). The result of this well suggest that, first of all the fractures may have different orientation, thus the horizontal well didn't intersect that many of them, and secondly, the fractures may be closed because of the loss of pore pressure due to production.

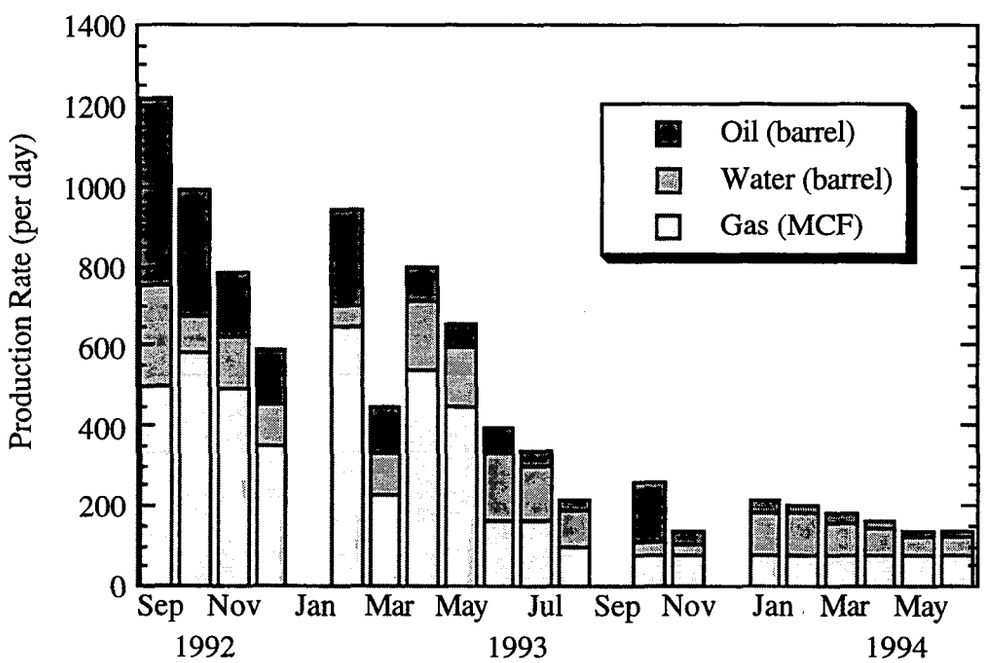

Figure B.8: Production history of the Amoco-Arco Morton Ranch well.

Arco (Vastar Res.) and Amoco Red Mountain 1-H well was drilled near the intersection of line 2 and line 3 after the seismic study. Scientists at Amoco and Arco estimated the fracture orientation and density from the analysis of four-component shear-wave data and the well was designed based on their interpretation. The total depth was reached on

December 30, 1993. Inside the Frontier formation at about 11511 feet TVD (true vertical depth) the well went horizontal for about 1100 feet trending southeast. The well was reported hitting numerous fractures, and the test production on July 18, 1994 showed 1068 MCFGPD, 32BOPD and only 3 barrels of water per day. The initial result demonstrated once again the effectiveness of the four-component shear-wave method developed by Alford (1986). Since the well is fairly new, much information is still not available and this result is only preliminary.

B.10 Structural features in the study area

At the Niobrara level, the axis of an anticline trends southwest-northeast through the central portion of the Fort Fetterman site, as shown in the structure contour map (Figure B.9). There appears to be a change in dip, or a flattening of the structure, just south of line 2, before the beds ramp up sharply in the flexure to the southwest. This change in dip also corresponds approximately with an area of anomalous rotation results in the fracture orientation. The First Frontier structure map (Figure B.10) also shows an anticlinal feature in a similar orientation; again there is an abrupt change in dip associated with the steep flexure.

The structural trend is subparallel with the fracture orientation of N55^{o}E - N60^{o}E determined for the Frontier formation in the Apache #36-1 State well. Two of these fractured intervals are shown on the logs (Figure B.5). The other fracture orientation, for a group of fractures within the Niobrara at this well location, was perpendicular to this trend, approximately N30^{o}W - N40^{o}W. In the eastern part of the study area (line 4), there is a possible change in orientation of the regional flexure trend from northwest to northeast (Amoco Corp., personal comm.). This change may be associated with the transition to the bordering Hartville Uplift (see structural features, Figure B.1). Mitchell and Rogers (1993), in a study of the region just north and east of the Fort Fetterman site, found that trends in isopach and resistivity maps correlate with predominant fracture orientations and regional tectonic trends.

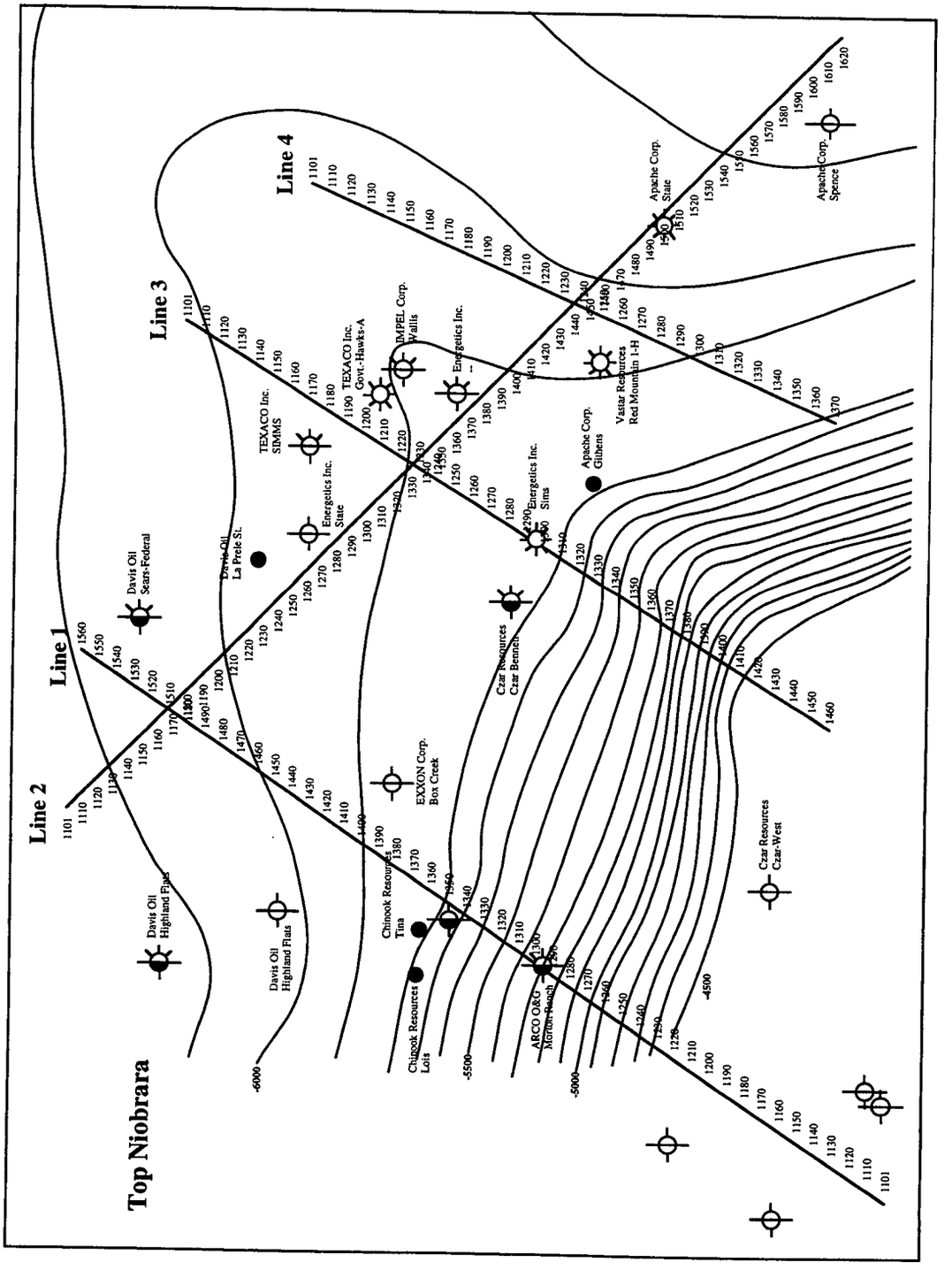

Figure B.9: Structure contour map on top of Niobrara Formation in the study area, based primarily on well log tops, with some seismic control (especially in steeply dipping areas). Contour interval is 100 feet .

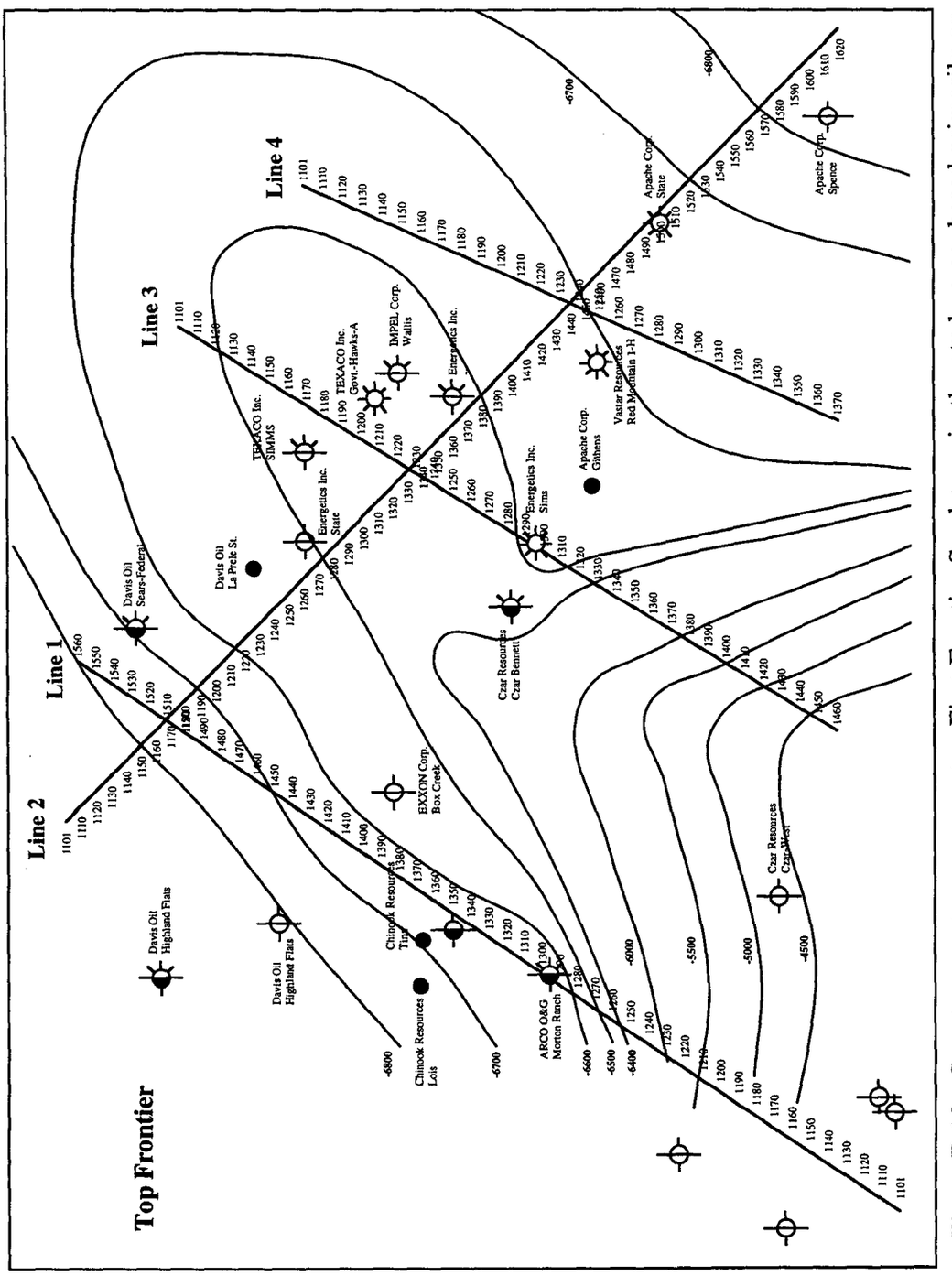

Figure B.10: Structure contour map on top First Frontier Sandstone in the study area, based primarily on well log tops, with some seismic control (especially in steeply dipping areas). Contour interval is 100 feet in less steep areas, 500 feet near flexure.

References

Alford, R. M., 1986, Shear data in the presence of azimuthal anisotropy: Dilley, Texas, paper presented at the 56th Annual Meeting, Soc. of Explor. Geophys., Houston.

Barlow, J. A., and Haun, J. D., 1966, Regional stratigraphy of Frontier Formation and relation to Salt Creek field, Wyoming: AAPG Bulletin, **50**, 2185-2196.

Dickinson, W. R., Klute, M. A., Hayes, M. J., Janecke, S. U., Lundin, E. R., McKittrick, M. A., and Olivares, M. D., 1988, Paleogeographic and paleotectonic setting of Laramide sedimentary basins in the central Rocky Mountain region: GSA Bulletin, **100**, 1023-1039.

Dutton, S.P., Hamlin, H. S., and Laubach, S. E., 1992, Geologic controls on reservoir properties of low-permeability sandstone, Frontier Formation, Moxa Arch, southwest Wyoming: The University of Texas at Austin, Bureau of Economic Geology, topical report no. GRI-92/0127, prepared for the Gas Research Institute, 199 p.

Galloway, W. E., and Hobday, D. K., 1983, Terrigenous clastic depositional systems: New York, Springer-Verlag, 423 p.

Hando, R. E., 1976, Powell-Ross field, Converse County, Wyoming: Wyoming Geological Association Guidebook, 28th Annual Field Conference, 139-145.

Lewis, C., Davis, T. L., and Vuillermoz, C., 1991, Three-dimensional multicomponent imaging of reservoir heterogeneity, Silo field, Wyoming: Geophys., **56**, 2048-2056.

Merewether, E. A., Cobban, W. A., and Spencer, C. W., 1976, The Upper Cretaceous Frontier Formation in the Kaycee-Tisdale Mountain area, Johnson County, Wyoming, Wyoming Geological Association Guidebook, 28th Annual Field Conference, 33-44.

Mitchell, G. C., and Rogers, M. H., 1993, Extensional tectonic influence on Lower and Upper Cretaceous stratigraphy and reservoirs, southern Powder River basin, Wyoming: The Mountain Geologist, **30**, no. 2, 54-68.

Prescott, M. W., 1975, Spearhead Ranch field, Converse County, Wyoming: Rocky Mountain Association of Geologists, A symposium on deep drilling frontiers in the central Rocky Mountains, 239-244.

Slack, P. B., 1981, Paleotectonics and hydrocarbon accumulation, Powder River basin, Wyoming: AAPG Bulletin, **65**, 730-743.

Sonnenberg, S. A., and R. J. Weimer, 1993, Oil production from Niobrara Formation, Silo field, Wyoming: Fracturing associated with a possible wrench fault system: The Mountain Geologist, **30**, no. 2, 39-53.

Wyoming Geological Association, 1976, Guidebook, 28th Annual Field Conference, Geology and energy resources of the Powder River: Casper, Wyoming, 328 p.